THE UNIVERSITY OF QUEENSLAND

AUSTRALIA

Vanadium-oxide-based electrode materials for Li-ion batteries

Peng Liu

Master of Science

A thesis submitted for the degree of Doctor of Philosophy at

The University of Queensland in 2016

School of Chemical Engineering

Abstract

Vanadium pentoxide (V_2O_5) with a layered crystalline structure is a promising cathode material for lithium-ion batteries (LIBs). V_2O_5 possesses theoretical capacities of 442 mAh g^{-1} for three Li^+ intercalations, or 294 mAh g^{-1} for two Li^+ intercalations per formula. These values are much higher than those of traditional cathode materials, such as $LiFePO_4$. However, several problems largely restrict the battery performance of V_2O_5, such as small Li^+ diffusion coefficient, low electrical conductivity, irreversible phase transitions, and dissolution of vanadium into the electrolyte. Therefore, V_2O_5 exhibits poor rate capability and cycling stability. This thesis aims to improve the performance of V_2O_5 in regard to its electrical conductivity, lithium diffusion coefficient, and structural stability of V_2O_5 by using strategies, such as nanostructuring, element doping, adding carbon additives, and conductive polymer coating.

The effects of electrode compositions and voltage windows on the electrochemical properties of V_2O_5 were investigated. The electrode compositions were varied by changing the ratio among V_2O_5, carbon black (CB), and poly(vinylidene fluoride) (PVDF). Two electrodes were prepared with the different V_2O_5:CB:PVDF ratios of 7:2:1 and 8:1:1. The V_2O_5 electrode with the 7:2:1 composition exhibited better cycling and rate performance in the voltage range of 1.5–4.0 V, due to higher electric conductivities. The electrochemical properties of this electrode were further improved by changing the voltage windows of charge/discharge. The narrow voltage window of 2–4 V only allows V_2O_5 to have a maximum of two lithium intercalations, which excludes the formation of irreversible ω-$Li_3V_2O_5$ phase. In the voltage range of 2–4 V, the electrochemical reversibility of the 7:2:1 V_2O_5 electrode was greatly improved, leading to better cycling performance.

Poly(3,4-ethylenedioxythiophene) (PEDOT) and multi-walled carbon nanotubes (MWCNTs) were employed to modify commercial V_2O_5 to prepare composite electrode materials for LIBs. It was found that MWCNTs improved the electric conductivity of the MWCNT-modified V_2O_5. In comparison, PEDOT not only performed better in enhancing the electric conductivity of the PEDOT-modified V_2O_5 but also enhanced its stability against electrolyte. The V_2O_5 modified with 20% PEDOT exhibited the current density of 574 mA g^{-1} for charging at 2.6 V, which is much larger than the 293 mA g^{-1} of the sample with 20% MWCNT. When applied as a cathode for lithium ion batteries, the sample

modified with PEDOT performed the best, followed by the sample modified with both MWCNTs and PEDOT, and the sample modified with MWCNTs only.

Cu-doped V_2O_5 nanobelts were synthesized by a facile hydrothermal treatment method as cathode materials for LIBs. The single phase Cu-doped V_2O_5 nanobelts were obtained with up to 4 mol% of copper. Both the V_2O_5 and $Cu_{0.04}V_2O_5$ nanobelts were highly interconnected to form web networks. The width of the $Cu_{0.04}V_2O_5$ nanobelts was smaller than that of the V_2O_5 nanobelts. The electric conductivity of the $Cu_{0.04}V_2O_5$ was enhanced, due to the mixed valences of Cu and V ions. When applied as the cathode material for LIBs, the $Cu_{0.04}V_2O_5$ nanobelts showed better cycling and rate performance than that of V_2O_5 nanobelts.

Declaration by author

This thesis is composed of my original work, and contains no material previously published or written by another person except where due reference has been made in the text. I have clearly stated the contribution by others to jointly-authored works that I have included in my thesis.

I have clearly stated the contribution of others to my thesis as a whole, including statistical assistance, survey design, data analysis, significant technical procedures, professional editorial advice, and any other original research work used or reported in my thesis. The content of my thesis is the result of work I have carried out since the commencement of my research higher degree candidature and does not include a substantial part of work that has been submitted to qualify for the award of any other degree or diploma in any university or other tertiary institution. I have clearly stated which parts of my thesis, if any, have been submitted to qualify for another award.

I acknowledge that an electronic copy of my thesis must be lodged with the University Library and, subject to the policy and procedures of The University of Queensland, the thesis be made available for research and study in accordance with the Copyright Act 1968 unless a period of embargo has been approved by the Dean of the Graduate School.

I acknowledge that copyright of all material contained in my thesis resides with the copyright holder(s) of that material. Where appropriate I have obtained copyright permission from the copyright holder to reproduce material in this thesis.

Publications during candidature

P. Liu, B. Wang, X.M. Sun, I. Gentle, and X.S. Zhao, A comparative study of V_2O_5 modified with multi-walled carbon nanotubes and poly(3,4-ethylenedioxythiophene) for lithium-ion batteries, *Electrochim. Acta* 213, 557 (2016).

W. Cao, A.P. Hu, X.H. Chen, X.H. Liu, **P. Liu**, Q.L. Tang, and X.S. Zhao, NiO hollow microspheres interconnected by carbon nanotubes as an anode for lithium ion batteries, *Electrochim. Acta* 213, 75 (2016).

X.M. Sun, **P. Liu**, Y. Gu, T.E. Rufford, and X.S. Zhao, Control over the morphology and phase of MnO_x formed in the modified Hummers' method and impact on the electrocapacitive properties of MnOx-graphite oxide composite electrodes, *RSC Advances* 6, 44717 (2016).

B. Wang, B.H. Xu, T.F. Liu, **P. Liu**, C.F. Guo, S. Wang, Q.M. Wang, Z.G. Xiong, D.L. Wang, and X.S. Zhao, Mesoporous carbon-coated $LiFePO_4$ nanocrystals co-modified with graphene and Mg^{2+} doping as superior cathode materials for lithium ion batteries, *Nanoscale* 6, 986 (2014).

B. Wang, S. Wang, **P. Liu**, J. Deng, B.H. Xu, T.F. Liu, D.L. Wang, and X.S. Zhao, Growth of $LiFePO_4$ nanoplatelets with orientated (010) facets on graphene for fast lithium storage, *Mater. Lett*. 118, 137 (2014).

Publications included in this thesis

P. Liu, B. Wang, X.M. Sun, I. Gentle, and X.S. Zhao, A comparative study of V_2O_5 modified with multi-walled carbon nanotubes and poly(3,4-ethylenedioxythiophene) for lithium-ion batteries, *Electrochim. Acta* 213, 557 (2016).

Incorporated as Chapter 5

Contributor	Statement of contribution
Author Peng Liu (Candidate)	Designed experiments (100%) Wrote and edited paper (75%) Material characterization (95%)
Author Dr. Bo Wang	Wrote and edited paper (5%)
Author Xiaoming Sun	Material characterization (5%)
Author Prof. Ian Gentle	Wrote and edited paper (5%)
Author Prof. X.S. Zhao	Wrote and edited paper (15%)

Contributions by others to the thesis

None

Statement of parts of the thesis submitted to qualify for the award of another degree

None

Acknowledgements

I would like to express my sincere gratitude to my principle advisor Prof. George Zhao for giving me a precious chance to start my Ph.D. research in the field of lithium-ion batteries. His guidance, patient education, and continuing supports have been the most important guarantees for me to progress step by step. I am also grateful to my co-advisor Prof. Ian Gentle for his great supports, valuable suggestions, and discussions.

I would like to thank my colleagues for their kind help, including Mr. Bo Wang, Mr. Binghui Xu, Ms. Xiaoming Sun, Ms. Luhong Zhang, Dr. Zhigang Xiong, Dr. Ashok Nanjundan, Ms. Dongfang Yang, Mr. Rohit Gaddam, and Ms. Aiping Hu. I wish to say a big thank you to the lab mates for their contributions to the fantastic research environment.

I would like to thank my wife (Min Hao) and my parents (Quanjun Liu & Meiyun Zhou) for their deep love, support, and encouragement. I would never have gone so far without their selfless dedication and unwavering belief.

I would like to thank the Australian Commonwealth Government and The University of Queensland for the Australian Postgraduate Award (APA) and the International Postgraduate Research Scholarship (IPRS). The strong financial supports have been important guarantee for my full-time PHD research.

I would like to thank the technical staffs at the Centre for Microscopy and Microanalysis for the assistance with microscopy facilities: Ms Ying Yu, Mr Ron Rasch, Dr Graeme Auchterlonie, Dr Barry Wood, and Dr Kim Sewell. Their training and suggestions helped me to deep understand working principles and to operate the instruments efficiently.

Keywords

Lithium ion batteries, cathode, V_2O_5, nanostructure, polymer coating, doping, carbon, electrochemical properties, lithium storage mechanism

Australian and New Zealand Standard Research Classifications (ANZSRC)

ANZSRC code: 090403, Chemical Engineering Design, 60%
ANZSRC code: 090406, Powder and Particle Technology, 20%
ANZSRC code: 091205, Functional Materials, 20%

Fields of Research (FoR) Classification

FoR code: 0904, Chemical Engineering, 50%
FoR code: 0912, Materials Engineering, 30%
FoR code: 0204, Condensed Matter Physics, 20%

Table of Contents

Abstract ..... **I**
Declaration by author ..... **III**
Publications during candidature ..... **IV**
Acknowledgements ..... **VII**
Table of Contents ..... **IX**
List of Figures ..... **XII**
List of tables ..... **XVII**
List of equations ..... **XVII**
List of Abbreviations ..... **XVIII**
1 Introduction **1**
1.1 Background 1
1.2 Lithium-ion batteries 2
1.2.1 Development history 3
1.2.2 Working principles 5
1.2.3 Solid electrolyte interphase 6
1.2.4 Basic concepts 7
1.2.5 Challenges 9
1.3 Significance and research objectives 10
1.4 Thesis outline 11
2 Literature review **14**
2.1 Common cathode materials 14
2.1.1 Layered lithium metal oxides 14
2.1.2 Spinel LiM_2O_4 compound 16
2.1.3 Olivine lithium iron phosphate 17
2.2 Vanadium pentoxide cathode materials 19
2.2.1 Crystalline and hydrated V_2O_5 19
2.2.2 Nanostructured V_2O_5 26
2.2.3 Carbon modified V_2O_5 35
2.2.4 Cation-doped V_2O_5 44
2.2.5 Polymer-coated V_2O_5 47
2.3 Summary 51
3 Experiment methods **53**
3.1 Chemical reagents and materials 53

3.2 Occupational Health, Safety and Welfare 54
3.3 Material synthesis 54
3.3.1 Hydrothermal method 54
3.3.2 Reflux 55
3.3.3 Chemical oxidative polymerization 56
3.4 Material Characterization 56
3.4.1 X-ray diffraction 56
3.4.2 Scanning electron microscopy 57
3.4.3 Transmission electron microscopy 57
3.4.4 Energy dispersive X-Ray spectroscopy 58
3.4.5 Thermal gravimetric analysis 58
3.4.6 Brunauer-Emmette-Teller surface area analysis 58
3.4.7 Fourier transform infrared spectroscopy 59
3.4.8 X-ray photoelectron spectroscopy 59
3.5 Electrode preparation and cell assembly 59
3.6 Electrochemical measurements 61
3.6.1 Galvano-static charge/discharge 61
3.6.2 Cyclic voltammetry 61
3.6.3 Electrochemical impedance spectroscopy 61
4 The effects of electrode composition and voltage window on the electrochemical properties of V_2O_5 62
4.1 Introduction 62
4.2 Experimental 63
4.3 Results and discussions 64
4.3.1 Material properties 64
4.3.2 Effects of electrode composition 66
4.3.3 Effects of voltage window 71
4.3.4 Conclusions 74
5 A comparative study of V_2O_5 modified with multi-walled carbon nanotubes and poly(3,4-ethylenedioxythiophene) for lithium-ion batteries 76
5.1 Introduction 76
5.2 Experimental 77
5.2.1 Modification of V_2O_5 with MWCNTs 77
5.2.2 Modification of V_2O_5 with PEDOT 78
5.2.3 Modification of V_2O_5 with both MWCNTs and PEDOT 78

5.2.4 Characterization 78
5.2.5 Electrochemical measurements 79
5.3 Results and discussion 79
5.3.1 Physical characterization 79
5.3.2 Electrochemical characterization 84
5.4 Conclusions 89
6 Single-crystalline orthorhombic copper vanadate nanobelts as cathode material for lithium-ion batteries 90
6.1 Introduction 90
6.2 Experimental 91
6.3 Results and discussion 92
6.4 Conclusions 105
7 Conclusions and Recommendations 106
8 List of References 109

List of Figures

Figure 1.1 Comparison of various rechargeable batteries according to volumetric and gravimetric energy density.[1] 2
Figure 1.2 SEM image of dendritic lithium formed on the surface of lithium metal in rechargeable lithium batteries.[15].....4
Figure 1.3 Schematic diagram of a typical lithium-ion battery in a charging process.[29].....6
Figure 1.4 Schematic illustration of the SEI on a graphite anode. An inorganic layer appears next to the graphite surface, where the LiF crystals are observed. A porous organic layer is formed close to the electrolyte.[31] 7
Figure 2.1 Crystal structure of layered lithium transition-metal oxides ($LiMO_2$); Green color represents the MO_2 slabs, and red balls are Li ions.[29].....15
Figure 2.2 (a) Crystal structure of $LiFePO_4$ showing 1D Li+ diffusion tunnels along the *b*-axis; Lithium, oxygen, phosphor, and iron atoms are represented by green, red, purple, and brown balls, respectively. (b) Schematic illustration of immobile defects in 1D tunnels, which can obstruct Li+ diffusion; the red sections between two adjacent defects are completely inaccessible to lithium ions.[87] 18
Figure 2.3 The crystal structure of pristine V_2O_5 built by square pyramids sharing edges and corners. Red and white balls are oxygen and vanadium atoms.[108].....20
Figure 2.4 Schematic diagram of (a) possible Li^+ diffusion paths in the crystal lattice of the orthorhombic V_2O_5 viewed along the [010] direction; (b) path A, path B, and path C viewed along the [001] direction. Path A and path B propagate along the *b*-axis and the *c*-axis, respectively. Path C goes approximately along the diagonal of the *a*- and *b*-axis.[109] 21
Figure 2.5 Electrochemical cycling of V_2O_5 at different current rates.[100].....22
Figure 2.6 The crystal structures of σ–phase and γ–phase $Li_xV_2O_5$. Circles between layers are lithium atoms.[112] 23
Figure 2.7 The crystal structure of $V_2O_5 \cdot nH_2O$ xerogel in the *ac* plane. Red polyhedrons are VO_6 octahedrons. Green balls are water molecules.[114] 24
Figure 2.8 (a) XRD pattern and (b) TGA curve of the $V_2O_5 \cdot nH_2O$ xerogel; (c) effect of interlayer spacing on the n value of $V_2O_5 \cdot nH_2O$; (d) Discharge measurements of $V_2O_5 \cdot nH_2O$ xerogels annealed at different temperature with a current density of 100 μA/cm^2.[114,116].....25

Figure 2.9 TEM images of V_2O_5 hollow nanospheres at different magnifications. A high-resolution TEM image was shown in the inset.[123] 27
Figure 2.10 (a) HRTEM image of 100 nm thick and 400 nm wide V_2O_5 nanowires treated with BuLi for 10 s. The inset is the SAED pattern along the 〈001〉 axis. The (020) and (200) spots were attributed to the pristine orthorhombic V_2O_5, suggesting no lithium intercalation. (b) HRTEM image of 20 nm thick and 740 nm wide V_2O_5 nanowires treated with BuLi for 10 s. The ω-$Li_3V_2O_5$ is the primary phase, revealed by the (200) spot shown in the SAED pattern (inset). (c) TEM image of $Li_xV_2O_5$ nanowires treated with Br_2 to remove lithium ions. The SAED pattern (inset) was indexed to the pristine V_2O_5, indicating a full delithiation of $Li_xV_2O_5$ nanowires.[124] 27
Figure 2.11 (a) SEM image and a photograph (inset) of the centimeter-long V_2O_5 nanowires;[120] (b) Schematic diagram of the scalable synthesis of V_2O_5 nanobelts at room temperature as cathode materials for LIBs.[127] 29
Figure 2.12 Schematic illustration (A) of the synthesis of V_2O_5 nanosheets by a dissolution–splitting method. SEM image (B) and TEM image (C) of $(NH_4)_2V_6O_{16}$ nanosheets.[121].....30
Figure 2.13 AFM image (a) and height profile (b) of the V_2O_5 nanosheets with multi-layer stacking structure. The height profile in figure b corresponds to the white line in the figure a. The parallel stacked layers nanosheets have about 3–5 nm in thickness.[133].....32
Figure 2.14 (a) FESEM image of the hierarchical 3D V_2O_5 sponge superstructure built by highly interconnected V_2O_5 nanosheets. (b) The dependences of power densities on energy densities of 3D V_2O_5, stacked V_2O_5 film, and bulk V_2O_5 electrodes. The stacked V_2O_5 film was prepared by drying in a conventional vacuum oven.[142] 32
Figure 2.15 FESEM images of 3D porous V_2O_5 microspheres before (a-b) and after (c-d) annealing. The microspheres were comprised of highly oriented nanofibers.[143] 33
Figure 2.16 (a) FESEM and (b) TEM images of the precursor of hierarchical V_2O_5 hollow microspheres prepared by a solvothermal method at 200 °C for 12 h. The composition of the raw solution included VOC_2O_4 (2 mL, 0.0825 M) and ethylene glycol (20 mL).[140].....34

Figure 2.17 Schematic illustration for the synthesis carbon-coated V_2O_5 nanocrystals with mesoporous carbon as a hard template by a capillary-induced filling approach.[36] 35
Figure 2.18 Schematic diagram of synthesizing the nanocomposites of interconnected carbon nanotubes and V_2O_5 nanowires.[147] 37
Figure 2.19 (a) Schematic illustration of the synthesis of V_2O_5-coated MWCNT sponge. The thickness of the sponge is reduced from 2 mm to 170 μm after compression in coin cell. SEM images of MWCNT sponge before (b) and after (c) 1000 cycles of atomic layer depositions of V_2O_5. Rate performance (d) of the MWCNT/V_2O_5 sponge in the voltage range of 4.0–2.1 V at different current densities.[159] 38
Figure 2.20 (a) Schematic illustration of the novel efficient dual-conducting network in the V_2O_5/carbon tube-in-tube composite. (b) TEM image of the V_2O_5/carbon tube-in-tube composite, where the most V_2O_5 nanoparticles were encapsulated within carbon tube-in-tube. The red and black arrows represent V_2O_5 nanoparticles and the walls of carbon tube-in-tube.[149] 39
Figure 2.21 (a) Schematic illustration of a carbon nanotube encapsulating V_2O_5 nanosheets (V_2O_5@G). (b) Schematic illustration of the flexible V_2O_5@G membrane interwoven by nanocables. (c) SEM image and (d) photograph of the V_2O_5@G membrane. (e) TEM image of a V_2O_5@G nanocable.[160] 40
Figure 2.22 (a) SEM image of the cross-section of the V_2O_5 nanowire–GO composite paper. The inset is a schematic illustration for the uniform distribution of graphene nanosheets (black) and V_2O_5 nanowires (green) within the composite paper. (b) HRTEM image of the V_2O_5 nanowire–GO composite paper. A V_2O_5 nanowire (dashed lines) was laid on a GO nanosheet. (c) Cycling performance of the V_2O_5 nanowire–graphene (15 wt%) composite paper measured with a current density of 10000 mA g^{-1} between 1.7 V and 3.8 V for 100000 cycles.[161] 41
Figure 2.23 (a) The schematic illustration of the preparation of the rGO-supported porous V_2O_5 spheres (V_2O_5/rGO). First, graphite oxide was well exfoliated to form graphene oxide by a modified Hummers method and adequate ultrasonication. Vanadium isopropoxide ($VO(OiPr)_3$ was then easily attached on the GO surfaces, and nucleated into $V_2O_5 \cdot nH_2O$ with ammonia. A solvothermal treatment was used to produce the composites of rGO and reduced vanadium

oxide particles, which were oxidized into the V_2O_5/rGO composite by annealing. (b) SEM image of the composite of V_2O_5 with 46 wt% rGO.[166] 43
Figure 2.24 SEM images of the V_2O_5 nanosheets/RGO hierarchical composite. The inset is a schematic diagram of the hierarchical structure, where self-assembled V_2O_5 nanosheets were uniformly attached on the rGO sheets.[110] 44
Figure 2.25 FESEM image (a) of the cross-section of the free-standing V_2O_5–polypyrrole thin film with a thickness of 10 μm; Photographs of the pure V_2O_5 film (b) and the V_2O_5–polypyrrole film (c) with good flexibility under bending conditions.[189] 49
Figure 3.1 Schematic illustration of coin cell assembly. 60
Figure 4.1 XRD pattern of commercial V_2O_5 powder. 64
Figure 4.2 SEM images of commercial V_2O_5 powders at different magnifications. 65
Figure 4.3 Nitrogen adsorption-desorption isotherms of commercial V_2O_5 powder. 65
Figure 4.4 Cyclic voltammograms (first three cycles) of the V_2O_5 electrodes with different compositions a) 7V:2C:1P and b) 8V:1C:1P in the voltage range of 1.5-4.0 V. 66
Figure 4.5 Galvanostatic charge–discharge curves of the V_2O_5 electrodes with different compositions a) 7V:2C:1P and b) 8V:1C:1P in the voltage range of 1.5-4.0 V. 68
Figure 4.6 Cycling performance of the V_2O_5 electrodes with different compositions at a current density of 0.1 C in the voltage range of 1.5-4.0 V. 69
Figure 4.7 Rate performance of the V_2O_5 electrodes with different compositions in the voltage range of 1.5-4.0 V.....70
Figure 4.8 Electrochemical impedance spectra of the V_2O_5 electrodes with different compositions measured from 100 kHz to 1 mHz with a voltage amplitude of 5 mV. 71
Figure 4.9 Cyclic voltammograms (first three cycles) of the 7V:2C:1P V_2O_5 electrode in the voltage range of 2.0-4.0 V.....72
Figure 4.10 Galvanostatic charge–discharge curves of the 7V:2C:1P V_2O_5 electrode at a current density of 0.1 C in the voltage ranges of 2.0-4.0 V. 73
Figure 4.11 Cycling a) and rate b) performance of the 7V:2C:1P V_2O_5 electrode in the voltage range of 2-4 V.....74
Figure 5.1 XRD patterns of different samples. 80
Figure 5.2 TGA curves of VC5, VP10, and VC5P10. 81
Figure 5.3 SEM images of a) V_2O_5, b) VC5, c) VP10, and d) VC5P10. 82

Figure 5.4 EDS mapping of a) V, b) O, c) S, and d) dark field TEM image of sample VP10. 83
Figure 5.5 V 2p and S 2p XPS spectra of sample VP10. 83
Figure 5.6 ATR-FTIR spectra of V_2O_5, PEDOT, MWCNT, VP10, and VC5P10. 84
Figure 5.7 CV curves of V_2O_5, VP10, VP20, VC10, VC20, and VC10P10 for the 3rd cycle. 85
Figure 5.8 Cycling performance of a) VC and b) VP samples at 0.2C between 2.0 and 4.0 V. Comparison of rate capabilities of c) VC samples with V_2O_5 and d) VP samples with V_2O_5 at various current rates. 86
Figure 5.9 a) Cycling and b) rate performances of V_2O_5, VC5, VP10, and VC5P10 between 2.0 and 4.0 V. 88
Figure 5.10 Discharge-charge voltage profiles of VP10 at 0.2C between 2.0 and 4.0 V. ..89
Figure 6.1 XRD patterns of V_2O_5 and $Cu_{0.04}V_2O_5$ nano-belts annealed at 400 ℃ for 1 h. .93
Figure 6.2 SEM images of (a-b) V_2O_5 and (c-d) the $Cu_{0.04}V_2O_5$ nanobelts. 93
Figure 6.3 Nitrogen adsorption-desorption isotherms of the V_2O_5 and $Cu_{0.04}V_2O_5$. 94
Figure 6.4 TEM (a) and HRTEM (b) images of the V_2O_5 nanobelts. TEM (c) and HRTEM (d) images of the $Cu_{0.04}V_2O_5$ nanobelts. 95
Figure 6.5 EDX mapping of the $Cu_{0.04}V_2O_5$ nanobelts. 96
Figure 6.6 High-resolution XPS spectra of V 2p and Cu 2p for the $Cu_{0.04}V_2O_5$ nanobelts. 97
Figure 6.7 The SEM images of the products obtained with different hydrothermal reaction durations. (a-b) 10h, (c-d) 15 h. 98
Figure 6.8 The SEM images of the products obtained at 190 ℃ for different hydrothermal reaction durations. (a-b) 20h, (c-d) 25 h, (e-f) 30 h. 99
Figure 6.9 Cyclic voltammograms of the V_2O_5 nanobelts in the voltage range of 2.0-4.0 V. 100
Figure 6.10 Cyclic voltammograms of the $Cu_{0.04}V_2O_5$ nanobelts in the voltage range of 2.0-4.0 V. 100
Figure 6.11 Galvanostatic charge–discharge curves of a) V_2O_5 nanobelts and b) $Cu_{0.04}V_2O_5$ nanobelts in the voltage range of 2.0-4.0 V. 101
Figure 6.12 Electrochemical impedance spectra of the V_2O_5 and $Cu_{0.04}V_2O_5$ nanobelts measured from 100 kHz to 1 mHz with a voltage amplitude of 5 mV. 102
Figure 6.13 Cycling performance of the V_2O_5 and $Cu_{0.04}V_2O_5$ nanobelts at a current density of 0.1C in the voltage range of 2.0-4.0 V. 103
Figure 6.14 Rate performance of the V_2O_5 and $Cu_{0.04}V_2O_5$ nanobelts in the voltage range of 2.0-4.0 V. 104

List of tables

Table 2.1 The electrochemical performance of the V_2O_5-based hybrid materials for LIBs. 50
Table 3.1 The information of the chemical reagents used in this thesis. 53

List of equations

Equation 1.1 General redox reactions of LIBs for charging……6
Equation 1.2 Open circuit voltage ……..……..8
Equation 1.3 Operating voltage ……..8
Equation 1.4 Theoretical specific capacity……..8
Equation 1.5 Specific capacity ...……..8
Equation 2.1 Redox reaction of V_2O_5 for LIBs……..19
Equation 3.1 Hydrothermal reactions of V_2O_5 and H_2O_2……....55
Equation 3.2 Brunauer-Emmette-Teller theory……58
Equation 3.3 Specific BET surface area……....58
Equation 5.1 Phase transitions of V_2O_5 for discharging……84

List of Abbreviations

3D	Three dimensional
AFM	Atomic force microscope
ALD	Atomic layer deposition
APS	Ammonium persulfate
BET	Brunauer-Emmette-Teller
BJH	Barrett-Joyner-Halenda
CDI	Combination displacement/intercalation
CNT	Carbon nanotube
CTIT	Carbon tube-in-tube
CV	Cyclic voltammetry
CVD	Chemical vapor deposition
DMC	Dimethyl carbonate
EC	Ethylene carbonate
EDX	Energy-dispersive X-ray
EIS	Electrochemical impedance spectra
FTIR	Fourier transform infrared spectroscopy
GO	Graphene oxide
HEV	Hybrid electric vehicle
LIB	Lithium-ion battery
$LiMO_2$	Lithium metal oxides
$LiMPO_4$	Lithium metal phosphate
MWCNT	Multiwall carbon nanotube
NMP	N-methyl-2-pyrrolidone

PANI	Polyaniline
PHEV	Plug-in hybrid electric vehicle
PPy	Polypyrrole
R_{ct}	Charge transfer resistance
rGO	Reduced graphene oxide
SAED	Selected area electron diffraction
SEI	Solid electrolyte interphase
SEM	Scanning electron microscopy
TEM	Transmission electron microscopy
TGA	Thermal gravimetric analysis
V_2O_5	Vanadium pentoxide
V_2O_5@G	Carbon nanotube encapsulating V_2O_5 nanoparticles
$V_2O_5 \cdot nH_2O$	Hydrated vanadium pentoxide
VOC	Open circuit voltage
XPS	X-ray photoelectron spectra
XRD	X-ray diffraction

1 Introduction

1.1 Background

Environmental problems are causing more and more threat for the society, including air pollution, climate changes, global warming. These concerns are highly associated with the combustion of fossil fuels. Exploring sustainable and environmentally friendly energy resources are a significant task for present energy crisis. Solar energy, hydropower, and wind energy are the leading technologies of clean energy. In common, they have unstable and intermittent nature, which increases the cost and the difficulty for energy storage. Rechargeable batteries are playing an important role in the storage and output of clean energy. The produced energy can be efficiently stored in rechargeable batteries and be transmitted as needed later on. In addition, rechargeable batteries also dominate in powering electronic devices and plug-in hybrid electric vehicles (PHEVs). Particularly, PHEVs require high-performance rechargeable batteries with high energy and power densities.

Rechargeable batteries are electrochemical energy storage devices that conduct reversible conversion between electric energy and chemical energy. The widely used rechargeable batteries include lithium-ion batteries (LIB), nickel-cadmium (Ni-Cd) batteries, nickel-metal hydride (Ni-MH) batteries, and lead-acid batteries. LIBs occupied the largest portion (63%) of global battery sales, compared to the 23% for Ni–Cd and the 14% for Ni–MeH.[1] The lead-acid batteries are limited to supply power for starting, lighting, and ignition in automobiles. Ni–Cd batteries with excellent high-power performance are mainly used in power tools.

Among rechargeable batteries, LIBs exhibited the highest gravimetric and volumetric energy density with proper safety (Figure 1.1).[1,2] The LIBs can reach 180 W h kg^{-1} for the gravimetric energy density and 400 Wh L^{-1} for the volumetric energy density. The high energy density of LIBs is related to the high operating voltage of ~3.6 V, which is two times that (1.2 – 2.0 V) of the aqueous counterparts.[3] The other advantages of LIBs include

long lifespan, low self-discharge rate, flexible design, and no memory effect.[4] LIBs have been most widely used in portable electronic devices for decades. The large-scale LIBs are also needed in smart grids, storing off-peak electricity and releasing electricity during peak time. Powering plug-in hybrid electric vehicles (PHEVs) is another promising application of LIB, due to the outstanding energy density. PHEVs can be used s supplementary energy storage for smart grids.

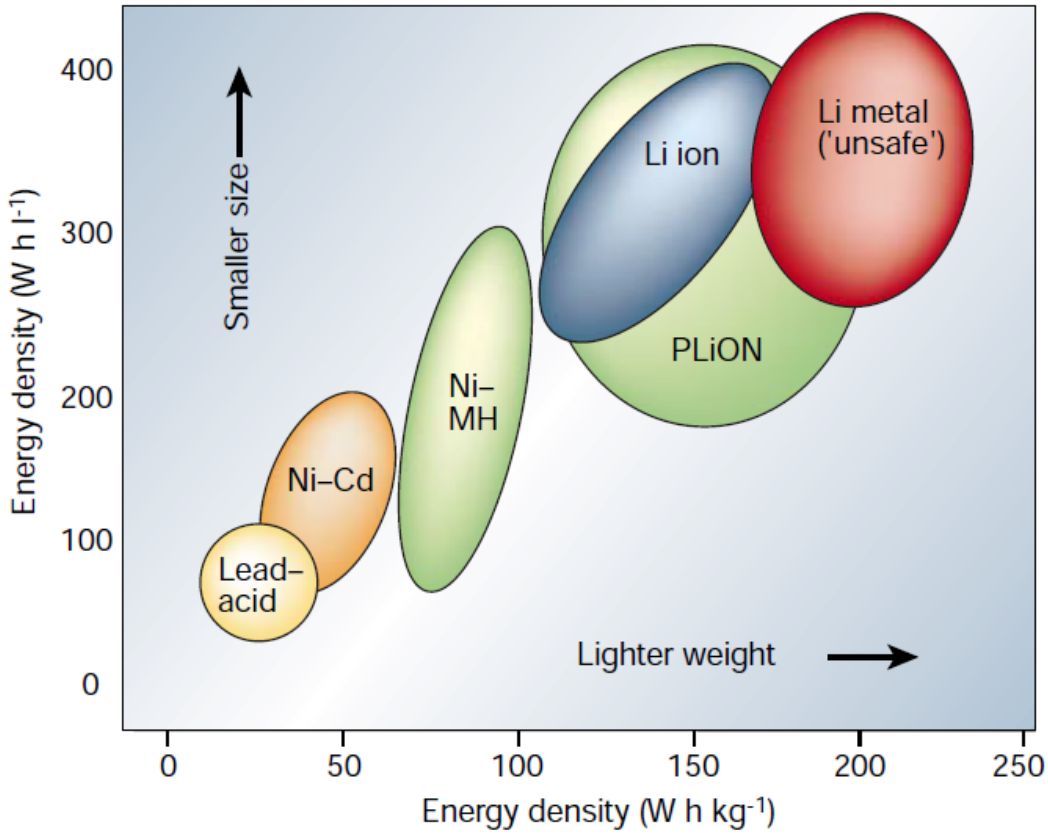

Figure 1.1 Comparison of various rechargeable batteries according to volumetric and gravimetric energy density.[1]

1.2 Lithium-ion batteries

Lithium-ion batteries are the most successful representative of commercial rechargeable batteries. The popularization of plug-in hybrid electric vehicles and large-scale LIBs highly rely on the high performance of next-generation LIBs. The development history and current status of LIBs are important to determine the proper routes for next-generation LIBs. The basic knowledge of LIBs is also reviewed, including working principles, key electrochemical parameters, and challenges.

1.2.1 **Development history**

The unique nature of Li metal motivated its application as the anode in rechargeable batteries. Among metallic elements, lithium has the best electro-positivity (-3.04 V versus standard hydrogen electrode) and the lightest atomic mass (6.94 g mol^{-1}), which is favorable for designing batteries with high energy density.[1] In 1958, Li metal was confirmed to be stable in some non-aqueous electrolytes, owing to the formation of a passivation layer on lithium surface.[5] This study stimulated the research of using lithium metal for batteries. In 1975, a primary (non-rechargeable) lithium battery was assembled successfully for the first time.[1] Due to the high specific capacity, primary lithium batteries were soon equipped in portable electronic devices.

Some inorganic compounds were identified as intercalation materials that enable reversible reactions with alkali metals.[1] This was a great breakthrough to make rechargeable lithium batteries possible. In 1976, Whittingham from Exxon introduced the first rechargeable lithium battery, which employed TiS_2 as the cathode, Li metal as the anode, and lithium perchlorate in dioxolane as the electrolyte.[6] The TiS_2 with a layered crystal structure is a typical intercalation compound with a low operating voltage of 2.2 V. The performance of rechargeable lithium batteries was largely restricted by lack of proper Li-metal/liquid electrolyte combination. Li dendrites are unevenly formed on the anode-electrolyte interface during cycling, which can pierce the separator and cause cell explosion (Figure 1.2).[7] The Li/Al alloys were effective alternatives to lithium metal, which can effectively eliminate the growth of dendritic lithium by reducing the intrinsic reactivity of lithium.[8] Unfortunately, the anodes of Li/Al alloys are easily damaged due to large volume changes during cycling. Exploring new intercalation materials is significant for the advances in rechargeable lithium batteries. Transition metal oxides were found to be good intercalation compounds with high capacities and high voltages, such as MnO_2, TiO_2, MoO_2, and V_6O_{13}.[9,10]

In order to enhance the battery safety, another intercalation compound can be used as the anode to replace lithium metal. In 1980, Lazzari *et al.* introduced an innovative rechargeable lithium battery by using Li_xWO_2 as the anode and Li_yTiS_2 as the cathode, which exhibited stable cycling without large capacity loss.[11] The concept of lithium-ion batteries had been proposed since then. In lithium ion batteries, lithium is in the ionic state rather than the metallic state. As a result, lithium ion batteries eliminate the safety problem

of dendritic lithium. A high-potential cathode material is required in a lithium ion battery to compensate the increase in the potential of the anode. The research emphasis changed from transition-metal disulfide to layered transition-metal oxides with higher voltages. In 1980, $LiCoO_2$ was first proposed as the cathode for LIB with high energy density by J.B. Goodenough.[12] But $LiCoO_2$ didn't attract too much attention due to lack of stable electrolytes in the operating voltage (above 4 V vs. Li/Li^+) of $LiCoO_2$. The following ten years were taken to implement the concept of lithium ion battery, by exploring proper anode materials, stable electrolytes, and lower cost. In 1989, a lithium ion battery showing good reversibility and a low operating voltage was achieved by combining a carbonaceous anode material with a metal-oxide cathode and a proper electrolyte.[13] This was a breakthrough in exploring appropriate components for lithium ion batteries. In 1991, Sony Corporation commercialized lithium ion batteries with $LiCoO_2$ as the cathode and graphite as the anode.[14] Portable electronic devices have been overwhelmingly powered by lithium ion batteries since then.

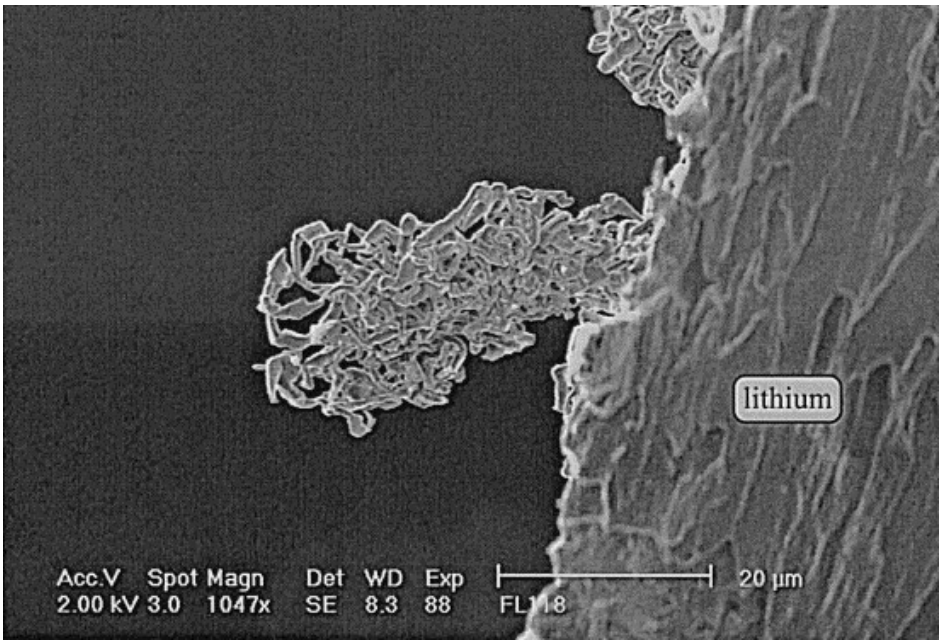

Figure 1.2 SEM image of dendritic lithium formed on the surface of lithium metal in rechargeable lithium batteries.[15]

It has been a continuous task for electrochemists to optimize lithium-ion batteries, from the aspects of energy density, power density, cycling stability, cell potential, and safety. Searching new electrode materials is of great importance in this course. There are several striking cathode materials, such as spinel $LiMn_2O_4$ in 1983 [16] and olivine $LiFePO_4$ in 1997

[17]. Transition metals like silicon and tin were found as the anode materials with highest specific capacities, which can form alloys with lithium.[18,19] In 1997, Fuji Photo Film initiated the commercial use of lithium-tin alloy as the anode for high-capacity lithium ion batteries.[20] Interest in carbonaceous anode materials was refreshed by one-dimensional carbon nanotube[21] and atomically thin graphene[22]. In addition, modifications of existing electrode materials with nanostructures, element doping, and conductive surface coating have been effective strategies to enhance their electrochemical properties. The layered $LiCo_{1/3}Ni_{1/3}Mn_{1/3}O_2$ compound introduced by Ohzuku in 2001 is a promising cathode candidate for commercial lithium ion batteries.[23] The cycling performance of lithium ion batteries is highly affected by the stability of electrode–electrolyte interface. Selecting optimum combinations of the electrode–electrolyte–electrode system has been considered as a great research approach to achieve stable electrode–electrolyte interface.

1.2.2 **Working principles**

A typical lithium ion battery consists of an anode, a cathode, an electrolyte, and a separator (Figure 1.3). Graphite and $LiCoO_2$ are commonly used as the anode and the cathode, respectively. Both of them are intercalation compounds with layered structures, which offer interlayer spacing to accommodate lithium ions. A microporous membrane is placed as the separator in between the anode and the cathode. The conventional electrolyte is a non-aqueous solution where lithium salt $LiFP_6$ is dissolved in a mixed organic solvent of ethylene carbonate (EC) and dimethyl carbonate (DMC).[24] Both the electrolyte and the separator are electric insulators but ionic conductors. The electrical contact between the anode and the cathode is made by lithium ions in the electrolyte through the separator. Electrons can only transport through the external circuit, avoiding internal shorting of the battery.[25]

Lithium ion batteries are also known as “Rocking-chair” batteries. Lithium ions are reversibly inserted/extracted into/from a layered electrode material during cycling, and a flow of electrons simultaneously runs through the external circuit.[26] In a charging process, lithium ions are deintercalated from the layered cathode into the electrolyte, and the electrolyte releases the same amount of lithium ions that intercalate into the carbonaceous anode. Electrons move in the opposite direction through the external circuit, resulting in the oxidation of the anode and the reduction of the cathode. During charging, the external

electric energy is converted into the chemical energy of the battery. As for discharging, the lithium ions are extracted from the anode back to the cathode, while electrons flow from the anode to the cathode via the external circuit.[27] Discharging generates electricity by the conversion of chemical energy to power electronic devices. The general redox reactions for charging can be expressed as Equation 1.1:[28]

Cathode $LiCoO_2 \rightarrow Li_{1-x}CoO_2 + xLi^+ + xe^-$

Anode $xLi^+ + xe^- + C_6 \rightarrow Li_xC_6$

Overall $LiCoO_2 + C_6 \rightarrow Li_{1-x}CoO_2 + Li_xC_6$

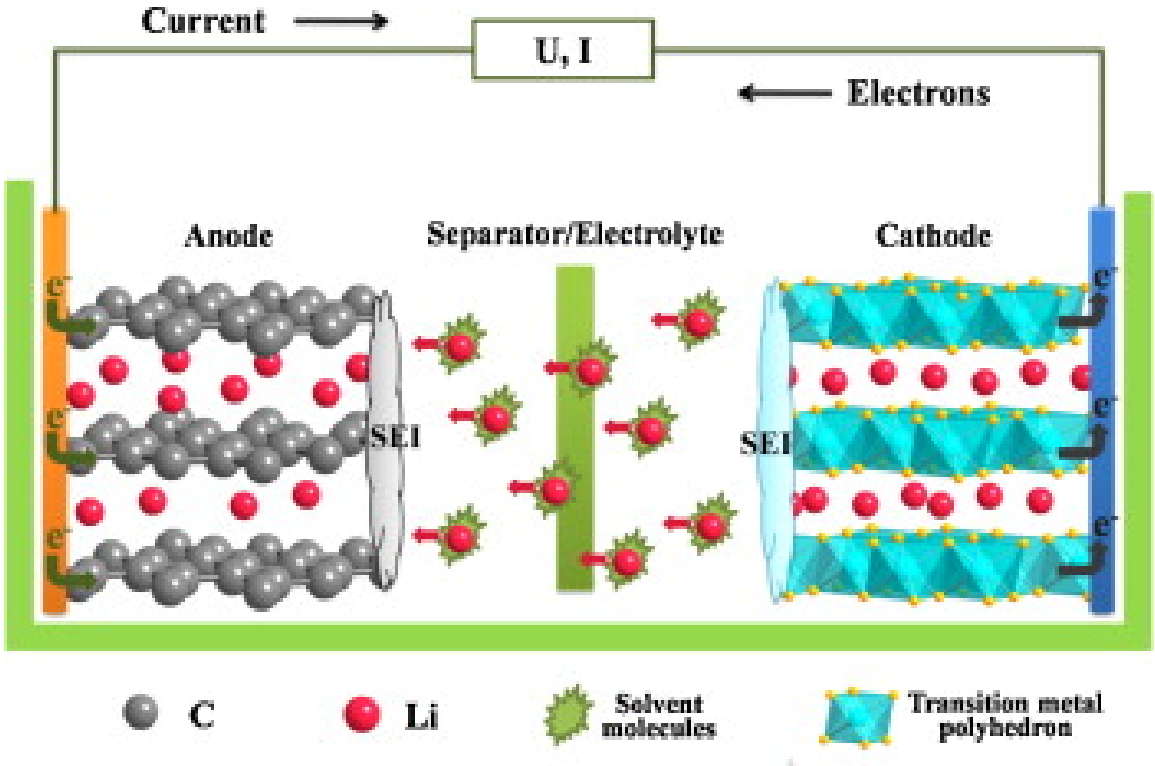

Figure 1.3 Schematic diagram of a typical lithium-ion battery in a charging process.[29]

1.2.3 **Solid electrolyte interphase**

As lithium ions intercalate into the anode during the first charge, a passivation layer appears on the surface of the anode due to the reduction of the electrolyte below 0.8 V.[3] This passive layer is called solid electrolyte interphase (SEI), which is ionically conducting but electrically insulating.[30] The thickness of SEI ranges from 20 to hundreds Å.[31] A typical SEI possesses the complex composition of inorganic and organic decomposition products. The composition of the SEI on a graphite anode is shown in Figure 1.4. The

degradation of lithium salts generates a dense layer of inorganic products next to the graphite surface. A porous organic layer is formed close to the electrolyte by reducing the solvent of the electrolyte.[3]

The formation of SEI consumes lithium ions, resulting in an irreversible capacity loss in the first cycle.[32] It might take several cycles for the complete formation of SEI. There are also some advantageous effects of SEI on the battery performance of LIBs. On the one hand, SEI protects the electrolyte from further decomposition in the following cycles. On the other hand, SEI prevents the co-intercalation of solvent molecules with Li-ions into the anode material. As a result, the formation of SEI leads to good cycling stability of LIBs.[3] Stable SEI is favorable to the long cycle life of a LIB, particularly at high current rates and at deep discharge.

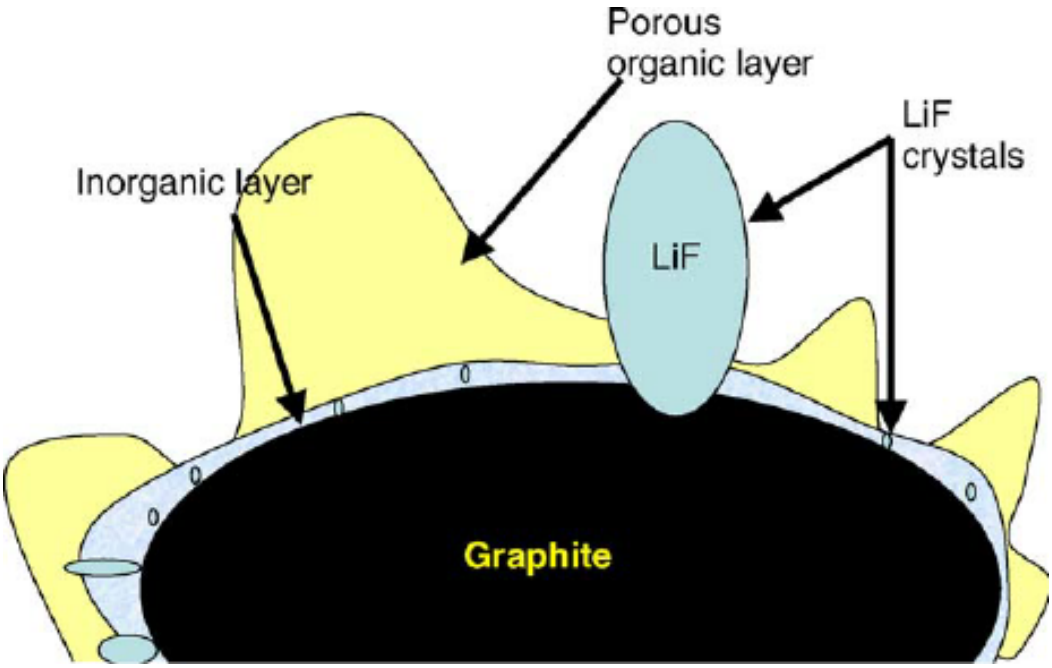

Figure 1.4 Schematic illustration of the SEI on a graphite anode. An inorganic layer appears next to the graphite surface, where the LiF crystals are observed. A porous organic layer is formed close to the electrolyte.[31]

1.2.4 **Basic concepts**

Several basic concepts are important to evaluate the battery performance of lithium ion batteries. The definitions and theories of these basic concepts are introduced as follows:

Open circuit voltage (V_{OC}) is the voltage of a LIB without any external current flow in the condition of open circuit. It is dependent on the difference in the electrochemical potentials of the anode and the cathode, according to Equation 1.2.

$$V_{OC} = (\mu_A - \mu_C)/(-nF)$$

Where μ_A is the electrochemical potential of the anode, μ_B is the electrochemical potential of the cathode, n is the quantity of electrons in the redox reaction, F is the Faraday constant with a value of 96485 C mol^{-1}.

Operating voltage is the voltage of a LIB measured in a closed circuit, according to Equation 1.3 of $V = V_{OC} - IR$, where I is the working current of the closed circuit and R is the internal resistance of the LIB.

Theoretical specific capacity C_o of a coin cell depends on the mass of the active material, according to Equation 1.4.[27]

$$C_o = \frac{26.8n}{M} m_o = m_o/q$$

Where m_o is the mass of the active material with g as the unit, M is the molar weight (g mol^{-1}) of the active material, n is the quantity of electrons in the redox reaction, and q is the electrochemical equivalence. The unit of theoretical capacity is Ah.

Specific capacity (Q_s) of an active material is the total amount of charges per unit mass transferred during charge or discharge, according to Equation 1.5.

$$Q_s = \frac{1}{m_o} \int_{t1}^{t2} I(t)dt$$

Where I is the charge/discharge current; t is the time; m_o is the mass of the active material. The unit of specific capacity is mAh g^{-1}. Energy density (W h Kg^{-1}) is the product of the specific capacity and the operating voltage, which presents the electric energy store in the unit mass of an active material. Power density (W Kg^{-1}) is the energy density in a unit time, which is associated with the rate capability of a coin cell.

Charge/discharge rate (denoted as "*nC*") reflects how fast lithium ions are transferred during cycling. *nC* means that the charge takes 1/*n* hours to reach the theoretical or nominal specific capacity. For examples, 0.1C corresponds to a full charge in 10 hours.

1.2.5 **Challenges**

Lithium-ion battery is considered as the best candidate for the energy storage devices in the plug-in hybrid electric vehicles (PHEV). However, the electrochemical performance of present LIBs still falls behind the strict requirements of PHEVs. Lithium-ion batteries have pressing need in performance enhancement, considering the current limitations, such as high cost, low energy and power densities, short cycle life, safety and environmental concerns.[26]

Most electrode materials exhibit specific capacities far below the theoretical values, which is limited by the intrinsic properties of active materials.[4] The poor electric conductivity and low lithium diffusion are common drawbacks of electrode materials. When LIBs are cycled at high current densities, the lithium diffusion in the active materials becomes more difficult due to large polarizations. The battery resistance increases with larger polarization, which gives rise to low power density and poor rate capability. Several problems of electrode materials during lithium insertion/extraction largely reduce the cycle-lives of LIBs, such as large volume changes, irreversible phase transition, unstable electrode-electrolyte interfaces.[1] Fire and explosion are the primary hazards of LIBs, which are associated with large charge/discharge currents, flammability of electrolytes, and pack engineering.[33]

Cathodes are components that most restrict the performance of LIBs. The cell voltages and capacities of LIBs mainly depend on the cathode. When the specific capacity of a node reaches 1200 mAh g^{-1}, further increase in the capacity of the anode almost has no contribution the total cell capacity.[34] Silicon anode material has the highest theoretical specific capacity of 4200 $mAhg^{-1}$ among all the electrodes for LIBs.[35] In comparison, typical cathode materials only exhibit small specific capacities between 160 and 200 mAh g^{-1}, such as $LiNi_{1/3}Co_{1/3}Mn_{1/3}O_2$ and $LiFePO_4$. Therefore, the specific capacities of cathode materials fall far behind those of anode materials, which become a bottleneck for developing LIBs with high energy density. To largely enhance the electrochemical performance of LIBs, it is essential to explore cathode materials with higher capacities.
Ideal cathode materials need to be developed from several aspects as follows:

(1) High energy density

As energy density is determined by both the working voltage and the specific capacity, excellent cathode materials should exhibit high specific capacity and high cell voltage. As

for intercalation compounds, multiple lithium intercalations per formula are favorable for high specific capacities.

(2) Good structural stability

The structural stability of a cathode material directly affects its cycling performance. During lithium insertion/extraction, ideal cathode materials can keep zero volume expansion, and fully reversible phase transitions, small voltage changes within 0.4 V. Good cycling stability also requires cathode materials to remain stable in contact with the electrolyte.

(3) High electric and ionic conductivities.

High power density is an important feature for cathode materials that possess excellent rate performance. Rate capability mainly relies on the kinetics of lithium ion diffusion and electron transport.[36] Nanostructured compounds with high electric and ionic conductivities are top candidates for cathode materials with high rate performance. Nanoscale cathode materials highly reduce the distances that lithium ions and electrons transport during cycling.

(4) Low cost and non-toxicity

Commercial $LiCoO_2$ cathode materials are expensive and toxic, largely restricting the development of large-scale LIBs. Therefore, new cathode materials are expected to be abundant and environmentally benign.

1.3 Significance and research objectives

Cathode materials are the components that most restrict the battery performance of lithium ion batteries. The cell voltage and total capacity of a LIB depend on the of the cathode. The theoretical capacity of silicon anode is the highest (4200 $mAhg^{-1}$), which is over 30 times the specific capacity (137 mAh g^{-1}) of the commercial $LiCoO_2$ cathode.[35,37] To meet the requirements of plug-in hybrid electric vehicles, this project is of great significance to develop novel cathode materials with high energy and power densities. Vanadium pentoxide (V_2O_5) is a cathode material with a layered crystalline structure. This typical intercalation compound has large theoretical capacities of 294 mAh g^{-1} for two Li^+ or 437 mAh g^{-1} for three Li^+ intercalation/deintercalation,[38] which are much larger than those of traditional cathode materials, such as $LiCoO_2$ (140 mAh g^{-1}),[39] $LiMn_2O_4$ (148 mAh g^{-1}),[40] and $LiFePO_4$ (170 mAh g^{-1}).[41] Therefore, V_2O_5 is an excellent candidate for next-

generation high performance cathode materials. Synthesizing advanced V_2O_5 materials with outstanding electrochemical performance is the focus of this project. However, V_2O_5 has drawbacks such as low Li^+ diffusion coefficient (10^{-12} to 10^{-13} $cm^2\ s^{-1}$), poor electric conductivity (10^{-2} to 10^{-3} S cm^{-1}), irreversible phase transitions, and dissolution of vanadium into the electrolyte.[42,43] The layered V_2O_5 exhibits fast capacity fading and poor rate capability, which reduces its potential to be used as a commercial cathode material.

The nanostructured V_2O_5 materials can effectively enhance the battery performance of the V_2O_5 cathode material. Nanostructures can shorten the diffusion length of lithium ions by reducing particle sizes, facilitate electrolyte penetration by generating porous structures, and buffer volume changes during lithium insertion/extraction by free voids. A novel strategy is to integrate cation doping with the V_2O_5 nanostructures. This design not only has the advantages of the V_2O_5 nanomaterials, but also increases the intrinsic electric conductivity of V_2O_5. In addition, It is significant to modify the nanostructured V_2O_5 with conductive additives, such as carbon materials and conductive polymers. Both conducting carbon and polymers can enhance the electric conductivity on the V_2O_5 surface, and prevent particle aggregation. The polymer coating also works as a protective surface layer preventing direct contact of V_2O_5 with the electrolyte.

The research objectives of this project are to design and synthesize the V_2O_5-based composite cathodes materials for high-performance lithium-ion batteries from the following aspects:

(1) To develop a facile, low-cost, green synthesis method to prepare V_2O_5 nanomaterials.
(2) To optimize the nanoscale architecture of V_2O_5 with a robust structure, high porosity, and small particle size.
(3) To enhance the electric conductivity of nanostructured V_2O_5 by cation doping or adding conductive additives.
(4) To prevent the loss of the active material due to particle aggregation and by coating conductive polymers on the V_2O_5 surface.
(5) To optimize electrode composition for maximizing the battery performance.

1.4 Thesis outline

This thesis includes seven chapters, which are briefly introduced as follows:

Chapter 1 Introduction – This chapter starts with presenting background, development history, working principles, and challenges of lithium-ion batteries. The significance of this project and research objectives are then summarized.

Chapter 2 Literature review – This chapter first introduces the structural and electrochemical properties of conventional cathode materials for LIBs. The focus of this chapter then switches to the detailed information of vanadium pentoxide cathode materials, including nanostructured V_2O_5, carbon modified V_2O_5, cation-doped V_2O_5, and polymer-coated V_2O_5.

Chapter 3 Experiment methods –This Chapter presents that chemicals and methods that have been used to synthesize the materials. The instrumental analysis techniques that have been used for physical and electrochemical characterizations are also briefly introduced.

Chapter 4 The effects of electrode composition and voltage window on the electrochemical properties of V_2O_5 – This chapter investigates the effects of electrode composition and voltage window on battery performances of V_2O_5. The electrode composition is optimized by manipulating the weight ratios among active materials, carbon blacks, and PVDF binder. Two electrodes with different compositions (7:2:1 and 8:1:1) were prepared for electrochemical measurements. Moreover, the formation of ω-$Li_3V_2O_5$ can be eliminated by changing the voltage windows from 1.5-4 V to 2-4 V.

Chapter 5 A comparative study of V_2O_5 modified with multi-walled carbon nanotubes and poly(3,4-ethylenedioxythiophene) for lithium-ion batteries – The V_2O_5 composites with MWCNTs and PEDOT are prepared and evaluated for lithium ion batteries. PEDOT and MWCNTs are both favorable for improving the battery performance of V_2O_5. It is of interest to study the effect of both conductive additives on material properties and electrochemical properties of V_2O_5. The amount of PEDOT and MWCNTs are manipulated to optimize electrodes for LIBs.

Chapter 6 Single-crystalline orthorhombic copper vanadate nanobelts as cathode material for lithium-ion batteries – The Cu-doped V_2O_5 nanobelts are synthesized by hydrothermal treatment method. The copper element can effectively increase the conductivity of V_2O_5. This chapter systematically demonstrates the material properties,

battery performance, and electrochemical mechanism of single phase Cu-doped V_2O_5 nanobelts.

Chapter 7 Conclusions and recommendations – This chapter summarizes the highlights of this thesis and gives recommendations for future research.

2 Literature review

2.1 Common cathode materials

In lithium ion batteries, the total specific capacity and cell voltages are dominated by cathode materials. The advances in cathode materials are crucial for high-energy and high-power LIBs. In terms of crystal structure, cathode materials can be divided into different groups, including layered lithium metal oxides ($LiMO_2$), spinel LiM_2O_4 compound, lithium metal phosphate $LiMPO_4$, and vanadium oxides. These cathode materials are lithium intercalation compounds, which allow lithium insertion/extraction for electrochemical redox reactions. Some common problems of cathode materials are associated with the lithium insertion/extraction, such as structural instability, slow lithium diffusion, volume changes, and phase transitions. Various strategies have been developed for improving the battery performance of conventional cathode materials.

2.1.1 **Layered lithium metal oxides**

$LiCoO_2$ is the most widely used cathode material for commercial lithium ion batteries, owing to high specific energy density, low self-discharge rate, and long cycle life.[44-46] It is crystallized in the layered rhombohedral phase (R3m), similar to the α-$NaFeO_2$ structure (Figure 2.1).[47] CoO_6 octahedra are connected by sharing edges, forming layers of CoO_2. Lithium ions reside between the layers of CoO_2 and are octahedrally coordinated with surrounding oxygen atoms. The positively charged lithium layers play an important role in stabilizing the crystal lattice by screening the negatively charged layers of CoO_2.[37] The lithium diffusion of $LiCoO_2$ is two-dimensional between the CoO_2 layers. As lithium ions are extracted, Co^{3+} is oxidized to unstable Co^{4+}. The repulsions of adjacent CoO_2 layers increase with the gradual removal of lithium ions, leading to lattice expansion along the *c* axis. The structural stability is reduced with lithium extraction.

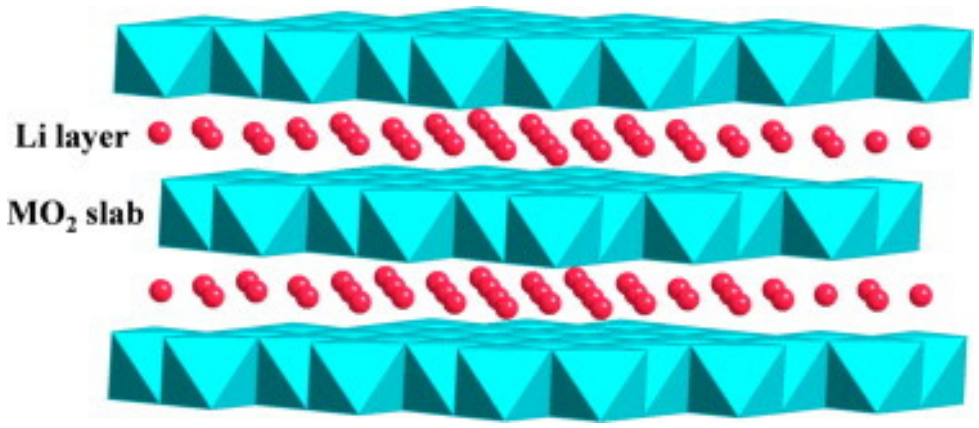

Figure 2.1 Crystal structure of layered lithium transition-metal oxides ($LiMO_2$); Green color represents the MO_2 slabs, and red balls are Li ions.[29]

The theoretical discharge capacity of $LiCoO_2$ is 273.8 mAh g^{-1}, corresponding to the extraction of one lithium per formula.[48] In practice, the reversible extraction/insertion of lithium ions within $LiCoO_2$ are restricted to less than 0.5 lithium, giving rise to a capacity of 137 mAh g^{-1} that is half of the theoretical value. Extraction of more than 0.5 lithium induces abrupt expansion of the c axis, leading to electrode degradation and fast capacity fading. [37] The dissolution of Co^{4+} ions into the electrolyte is another reason for the poor capacity retention. To maintain $LiCoO_2$ in good structural stability, the cut-off voltage of charging is limited to 4.2 V. Several strategies have been investigated to further enhance the specific capacity and cycling stability of $LiCoO_2$, including surface coating [46,49-51] and element doping [48,52,53].

Due to the expensive and toxic nature, $LiCoO_2$ is not suitable for large-scale lithium ion batteries. Alternatives to $LiCoO_2$ need to be abundant and environmentally friendly. $LiNiO_2$ also exhibits the α-$NaFeO_2$ structure, the energy density of which is 15% higher by volume and 20% higher by mass than that of $LiCoO_2$.[54] Ni^{2+} ions in $LiNiO_2$ are inclined to occupy lithium sites, leading to poor lithium diffusion and large capacity loss as main challenges of $LiNiO_2$.[55] Layered $LiMnO_2$ is a metastable phase with a monoclinic (*C*2/*m*) crystal structure, which converts into the stable $LiMn_2O_4$ spinel structure during charging.[56,57] This phase transition results in very poor electrochemical properties of $LiMnO_2$. Generally, the intrinsic drawbacks of $LiNiO_2$ and $LiMnO_2$ prevent them to be satisfactory cathode materials for LIBs. A new strategy has been proposed to mix Co, Ni, and Mn ions to form new layered compounds $LiCo_xNi_yMn_{1-x-y}O_2$ with various compositions.[58,59] Among them, the $LiCo_{1/3}Ni_{1/3}Mn_{1/3}O_2$ compound attracted extensive attention as the best candidate for

the cathode materials of hybrid electric vehicle (HEV).[23,60-62] The $LiCo_{1/3}Ni_{1/3}Mn_{1/3}O_2$ exhibits good structural and thermal stability, high capacity, and excellent capacity retention. The specific capacity of $LiCo_{1/3}Ni_{1/3}Mn_{1/3}O_2$ is 200 mAh g^{-1} in a voltage range of 2.5–4.6 V.[60] The $LiCo_{1/3}Ni_{1/3}Mn_{1/3}O_2$ is isostructural with $LiCoO_2$, and exhibits nearly zero phase change during cycling.[63] However, the low electric conductivity of $LiCo_{1/3}Ni_{1/3}Mn_{1/3}O_2$ still restricts the rate capability at high current densities.[64] $LiCo_{1/3}Ni_{1/3}Mn_{1/3}O_2$ also shows a rapid capacity fading above 4.5 V.[65] A variety of surface modifications and elemental substitutions have been used to improve the battery performance of $LiCo_{1/3}Ni_{1/3}Mn_{1/3}O_2$.[66-68]

2.1.2 **Spinel LiM_2O_4 compound**

The spinel $LiMn_2O_4$ is another promising cathode material with a cubic structure (Fd3m), where manganese atoms reside on the octahedral sites and lithium atoms are located on the tetrahedral sites.[69] The presence of manganese enables $LiMn_2O_4$ to have the advantage of low cost, environmentally benign, and good safety. Different from the two-dimensional lithium diffusion in the α-$NaFeO_2$ structure, the spinel $LiMn_2O_4$ offers three-dimensional pathways for lithium diffusion, favorable for high rate performance.[54] The $LiMn_2O_4$ allows a maximum of one lithium intercalation, and transforms into the tetragonal $Li_2Mn_2O_4$ phase (space group F41/*ddm*) at around 3 V (vs. Li/Li^+).[70] This phase transition comes with a Jahn–Teller distortion to induce a large increase in the c/a ratio of the unit cell by 16%, which causes the electrode to lose the structural integrity.[71] Practically, $Li_2Mn_2O_4$ needs to be charged and discharged within a voltage range of 3.5–4.3 V to maintain the cubic structure within the composition of $Li_xMn_2O_4$ ($0 < x < 1$).[72] The theoretical capacity of $Li_xMn_2O_4$ ($0 < x < 1$) is 148 mAh g^{-1}, corresponding to lithium insertion/extraction at around 4 V (vs. Li/Li^+).[73] However, the $LiMn_2O_4$ cathode material is still challenged by severe capacity fading in the 4 V region during cycling. Two reasons are responsible for the capacity fading. First, dissolution of Mn into the electrolyte leads to the poor electrode stability.[74,75] Second, the structural integrity of the active material decreases with lithium insertion/extraction during cycling.[76]

Partial substitution of manganese with other transition metals is an effective method to improve the battery performance of the $LiMn_2O_4$ cathode material, such as iron,[77] cobalt,[78] nickel[79]. The dopant can greatly enhance the structural stability, leading to a

much lower capacity fading. $LiNi_{0.5}Mn_{1.5}O_4$ performs the best among the doped $LiMn_2O_4$ compounds, which exhibits good cycling stability and high energy density. In stoichiometric $LiNi_{0.5}Mn_{1.5}O_4$, the valence of Ni is +2, while the valence of Mn is completely raised to +4. The redox couple of Ni^{2+}/Ni^{4+} in $LiNi_{0.5}Mn_{1.5}O_4$ generates a high operating voltage of 4.7 V, leading to a high energy density.[29] In addition, non-stoichiometric $LiNi_{0.5}Mn_{1.5}O_{4-x}$ shows better rate performance than that of stoichiometric $LiNi_{0.5}Mn_{1.5}O_4$. It is attributed to the enhanced electric conductivity of the non-stoichiometric $LiNi_{0.5}Mn_{1.5}O_{4-x}$ by generating a small amount of Mn^{3+} ions.[80]

2.1.3 **Olivine lithium iron phosphate**

Lithium iron phosphate $LiFePO_4$ with the olivine structure is first reported as a cathode material for LIBs by Padhi *et al.* in 1997.[81] With insertion/extraction of lithium ions at the operating voltage of 3.4 V vs. Li^+/Li, $LiFePO_4$ has a theoretical capacity of 170 mAh g^{-1}.[82] $LiFePO_4$ has attracted ever-growing research interest, due to excellent cycling stability, low cost, non-toxicity, and high thermal stability.[83] The main problems of $LiFePO_4$ are low electronic conductivity ($\sim 10^{-9}$ to 10^{-10} S cm^{-1}) and low Li^+ diffusion coefficient ($\sim 10^{-14}$ cm^2 s^{-1}).[82] The sluggish transports of Li^+ ions and electrons in $LiFePO_4$ give rise to poor rate capability at high current densities, which largely restricts the commercialization of $LiFePO_4$.

Lithium intercalation/de-intercalation is accompanied by the reversible phase transitions between $FePO_4$ and $LiFePO_4$.[84] These two phases have the same crystal structure. $LiFePO_4$ initially possesses one Li ion per formula unit, which can be removed during charging to form $FePO_4$. Inversely, $FePO_4$ is recovered to $LiFePO_4$ by intake of one lithium ion. Olivine $LiFePO_4$ is crystallized in an orthorhombic crystal structure with the space group Pmnb (Figure 2.2a).[84,85] Iron atoms are located in the centers of FeO_6 octahedra, while phosphorous atoms are bonded with four oxygen atoms to form PO_4 tetrahedra. The FeO_6 octahedra are connected by sharing corners in the *bc*-plane. The PO_4 tetrahedra are linked with the FeO_6 octahedron by sharing one common edge. Lithium atoms are located in the tunnels built by edge-sharing LiO_6 octahedra along the *b*-axis. Therefore, the lithium diffusion is one-dimensional in $LiFePO_4$, where lithium ions only migrate through the tunnels along the *b*-axis.[86] As these tunnels are not connected, lithium ions can't jump from one tunnel to another. Any immobile defect in a tunnel can terminate the one-

dimensional lithium diffusion by blocking the motion of lithium ions (Figure 2.2b).[87] Within a tunnel, the sections between two adjacent defects become completely inaccessible to lithium ions. In comparison, immobile defects are not able to obstruct two-dimensional diffusion, as a result that lithium ions easily detour around the defects. Therefore, the epitaxial growth of $LiFePO_4$ crystals along the (010) plane is favorable for fast lithium storage.

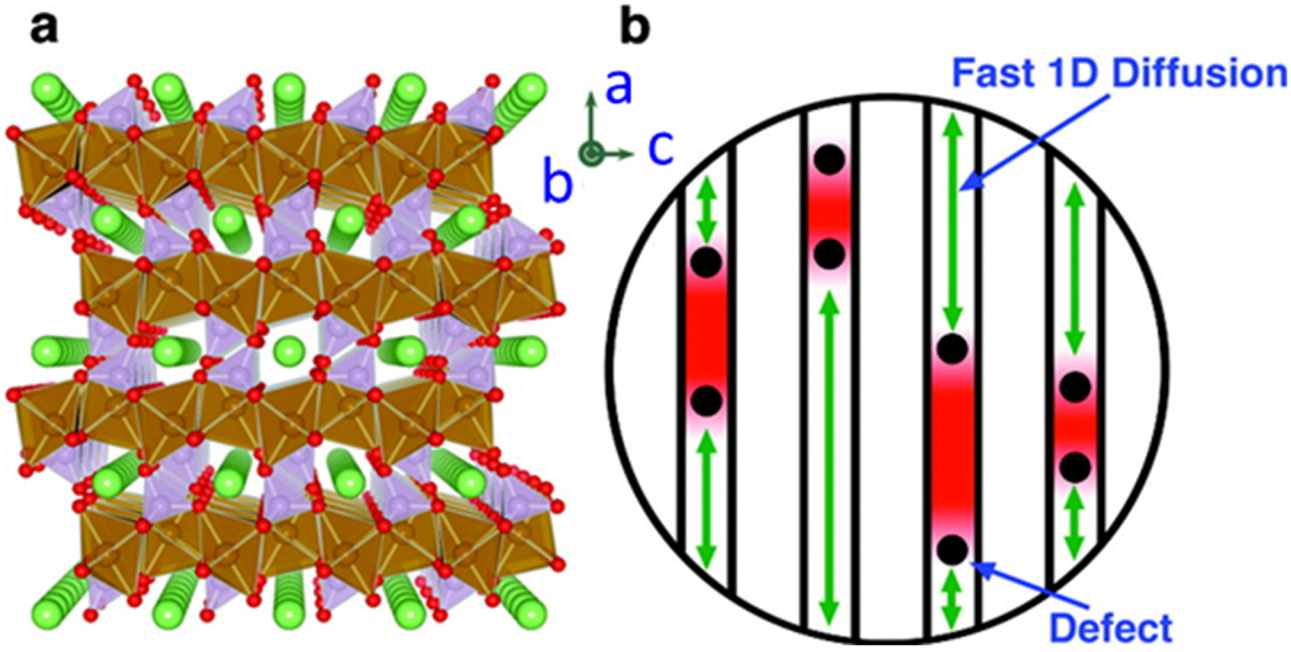

Figure 2.2 (a) Crystal structure of $LiFePO_4$ showing 1D Li+ diffusion tunnels along the *b*-axis; Lithium, oxygen, phosphor, and iron atoms are represented by green, red, purple, and brown balls, respectively. (b) Schematic illustration of immobile defects in 1D tunnels, which can obstruct Li+ diffusion; the red sections between two adjacent defects are completely inaccessible to lithium ions.[87]

Various approaches have been introduced to overcome the drawbacks of $LiFePO_4$, including element doping,[82,88] reducing particle size,[89-92] and surface modification with conductive materials.[93-95] Regarding a successful element doping, the doped cations should reside on the iron sites.[86] If the alien ions are located in the lithium sites, the one-dimensional lithium diffusion can be easily interrupted by these alien ions. The $LiFePO_4$ materials with oriented growth along the (010) facet have been particularly interesting nanostructures, which can effectively shorten Li^+ diffusion length and increase the number of active sites accessible to lithium ions.[93,96]

2.2 Vanadium pentoxide cathode materials

Vanadium is one of the most abundant transition metals in the earth's crust. It has multiple valences from V^{2+} to V^{5+}, forming different simple oxides like VO, V_2O_3, VO_2, and V_2O_5. Many complex oxides can also be built with vanadium atoms of mixed valences. V_3O_7, V_4O_9, and V_6O_{13} are mixed with V^{5+} and V^{4+} ions, while V_6O_{11}, V_7O_{13}, and V_8O_{15} are comprised of V^{3+} and V^{4+} ions.[97]

2.2.1 **Crystalline and hydrated V_2O_5**

Among the family of vanadium oxides, V_2O_5 is the most stable material by having the highest oxidation state of 5+. It crystallizes in a layered orthorhombic structure, which has the space group *Pmnm* (59) with the lattice parameters *a* = 11.510 Å, *b* = 3.563 Å, and *c* = 4.369 Å.[98] The basic polyhedrons in the crystal structure of V_2O_5 are VO_5 pyramids, where the four oxygen atoms in the basal plane are connected with the vanadium atom by weak V-O bonds (2 Å), and the oxygen atom in the apex is coupled with the vanadium atom by a short V=O vanadyl bond (1.54 Å).[99] The VO_5 pyramids are mutually connected, forming a layer in the *ab* plane. These layers are periodically stacked along the *c*-axis, making V_2O_5 a layered material, as shown in (Figure 2.3). The VO_5 pyramids sharing edges are oriented in opposite directions, forming double chains along the *b*-axis. The double chains are linked along the *a*-axis by the corners of two pyramids aligned in the same direction. The VO_5 pyramids thus have their apices arranged in an up-up-down-down order along the *a*-axis.[100]

V_2O_5 is a typical intercalation compound due to the layered structure. The lattice of V_2O_5 reserves structural integrity when being reversibly intercalated by kinetic guest species (atoms, ions, or molecules).[101] The reversible lithium intercalation into V_2O_5 at ambient temperature was first investigated for rechargeable cells by Whittingham in 1976.[102] Since then, V_2O_5 has been studied as a promising cathode material for lithium ion batteries for several decades. The advantages of V_2O_5 include high capacity, high output voltage, low cost, and simple synthesis.[103] The theoretical specific capacities of V_2O_5 can reach 442 mAh g^{-1} for 3 moles of Li^+ insertions, and 294 mAh g^{-1} for 2 moles of Li^+ intercalations per mole of V_2O_5.[104-106] Lithium insertion and extraction in V_2O_5 can be described by Equation 2.1: $V_2O_5 + x\,Li^+ + x\,e^- \leftrightarrow Li_xV_2O_5$ ($0 \leq x \leq 3$). There are three paths for lithium diffusion in

the orthorhombic V_2O_5 (Figure 2.4).[107] Path A and path B propagate along the *b*-axis and the *c*-axis, respectively. Both of them are one-dimensional spatial diffusion tunnels. Path C is a two-dimensional diffusion route, which approximately goes along the diagonal of the *a*- and *b*-axis. Path A is the easiest direction for lithium ions to transport in the lattice of V_2O_5.

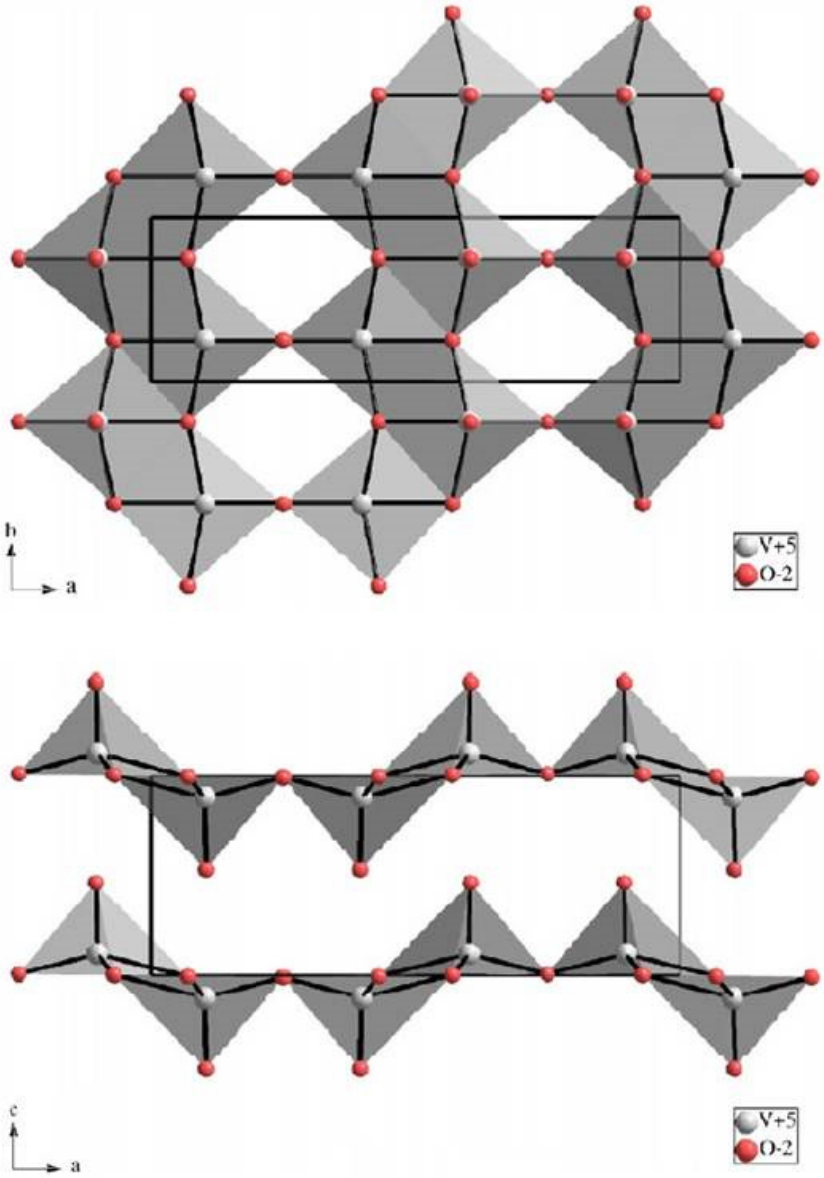

Figure 2.3 The crystal structure of pristine V_2O_5 built by square pyramids sharing edges and corners. Red and white balls are oxygen and vanadium atoms.[108]

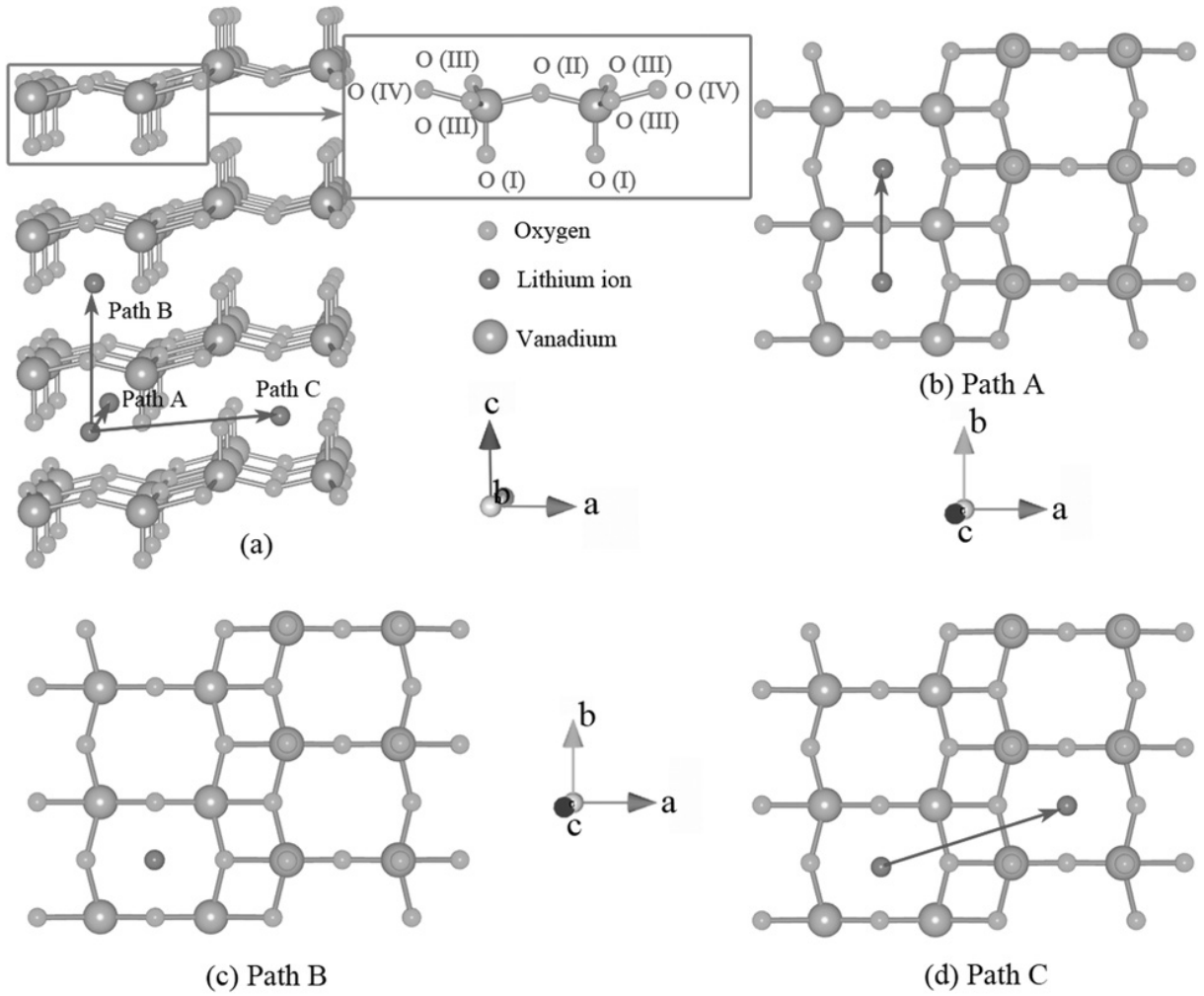

Figure 2.4 Schematic diagram of (a) possible Li^+ diffusion paths in the crystal lattice of the orthorhombic V_2O_5 viewed along the [010] direction; (b) path A, path B, and path C viewed along the [001] direction. Path A and path B propagate along the *b*-axis and the *c*-axis, respectively. Path C goes approximately along the diagonal of the *a*- and *b*-axis.[109]

Regarding practical commercialization for LIBs, several disadvantages of V_2O_5 have largely restricted the progress. V_2O_5 has small Li^+ diffusion coefficient (10^{-12} to 10^{-13} $cm^2 s^{-1}$) and low electrical conductivity (10^{-2} to 10^{-3} S cm^{-1}).[42,43] Irreversible phase transitions of V_2O_5 during deep discharge lead to structural instability.[110] Portions of vanadium could be dissolved into the electrolyte during cycling.[111] These problems lead to the poor rate capability and cycling stability of V_2O_5.

V_2O_5 has several phase transitions when different amounts of lithium are intercalated. With increasing lithium content, V_2O_5 successively transforms into the α ($X<0.1$), the ε ($0.35<x<0.7$), the σ ($0.9<x\leq1$), the γ ($1<x\leq2$), and the ω ($2<x\leq3$) phases.[99] The α-, ε-, and

σ-phases retain the structure of the unintercalated V_2O_5 phase, but with more puckered layers.[112] Particularly, the σ-phase realizes a doubling of the *c* parameter, by having every other layer shifted by half a unit cell along the *b*-axis.[99] The phase transitions for x≤1 are completely reversible. The potential plateaus at 3.4 and 3.2 V (vs Li^+/Li) in the curve of first discharge of V_2O_5 reflect the α/ε and ε /σ phase transitions, as can be seen in Figure 2.5. Further intercalation with more than one lithium results in a permanent phase transition into the γ-phase. The formation of the γ-phase from the σ-phase proceeds gradually during the entire 2.3 V plateau. Different from the pristine V_2O_5, the γ-phase has highly puckered layers, where the apices of VO_5 pyramids alternate up and down individually (Figure 2.6).[112] The γ-phase can be reversibly cycled in the lithium limit of 0≤x≤2. When V_2O_5 is deep discharged below 1.9 V, the irreversible ω-phase appears with more than two lithium intercalations. The ω-phase possesses a tetragonal structure (a=4.1 Å, c=9.2 Å), in which there are 50% V^{+4} and 50% V^{+3}.[113] However, this tetragonal structure disappears after the first cycle. The ω-phase changes into a rock-salt cubic structure with a lattice parameter of 4.1 Å.[99] There is 0.4 lithium trapped in the ω-phase after the first charge. The second discharge also fails to regain the maximum of three lithium intercalation, giving rise to a final composition of ω-$Li_{2.65}V_2O_5$. The ω-phase is only reversible over the restricted range of lithium concentration 0.4≤x≤2.65.[113] In addition, the lithium diffusion coefficient of V_2O_5 decreases with higher lithium content, which leads to inferior battery performance at high current densities.[113]

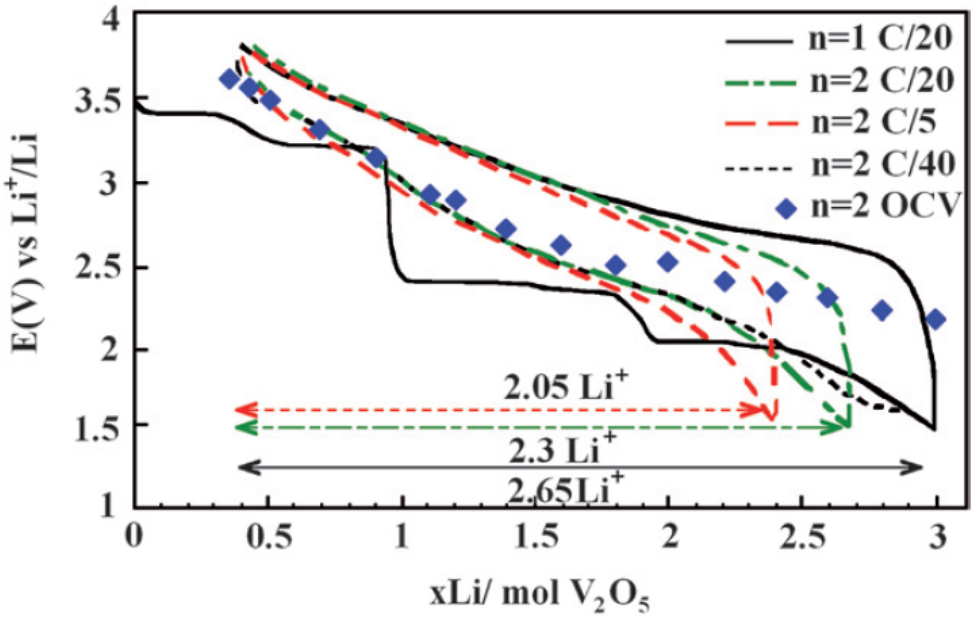

Figure 2.5 Electrochemical cycling of V_2O_5 at different current rates.[100]

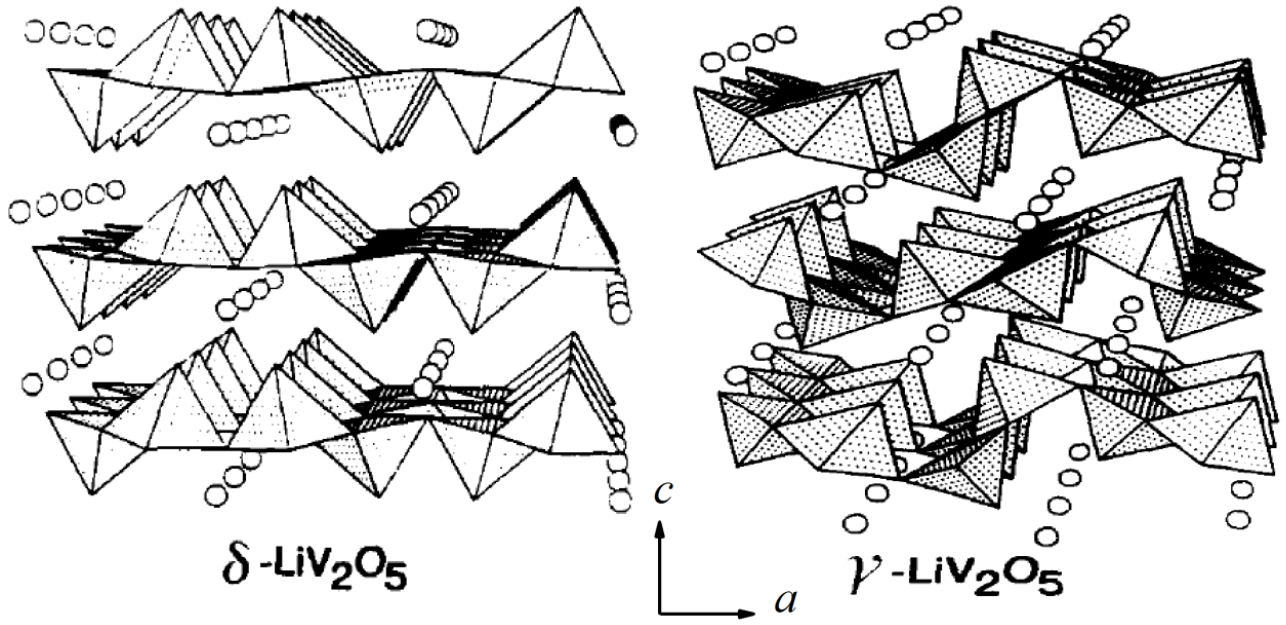

Figure 2.6 The crystal structures of σ–phase and γ–phase $Li_xV_2O_5$. Circles between layers are lithium atoms.[112]

In addition to the orthorhombic V_2O_5, hydrated vanadium pentoxide ($V_2O_5 \cdot nH_2O$) with low crystallinity is also a layered intercalation compound for LIBs. The structure of $V_2O_5 \cdot nH_2O$ features the stacking of bilayers constituted by two single layers of VO_5 pyramids. In comparison, the orthorhombic V_2O_5 only has the monolayers of the VO_5 pyramids periodically arranged along the *c*-axis. Water molecules are situated between the layers of $V_2O_5 \cdot nH_2O$, largely expanding the interlayer spacing. The minimum distance between the bilayers is 11.5 Å, shown in Figure 2.7. The two monolayers within a bilayer are separated by a gap of 2.9 Å.[114] The V-O polyhedrons in every bilayer can be also regarded as octahedrons. The VO_6 octahedrons sharing edges form double chains along the *b*-axis. Parallel double chains are further connected by corners of octahedrons to form a layer. Both V_2O_5 and $V_2O_5 \cdot nH_2O$ prefers crystal growth along one-dimension to generate nanobelts, due to the chain-based layer structure.[114]

$V_2O_5 \cdot nH_2O$ xerogels are common to show cracks and low porosity, caused by volatilization of water.[115] The $V_2O_5 \cdot nH_2O$ xerogel exhibits lamellar ordering along the *c*-axis, reflected by presence of only (00 *l*) diffractions in the XRD pattern of Figure 2.8a.[114,116] Thermal treatment has a great influence on the water content of the $V_2O_5 \cdot nH_2O$ (Figure 2.8b).[115,116] 1.6 mole of water exists in one mole of the $V_2O_5 \cdot nH_2O$ xerogel at room temperature. The

$V_2O_5 \cdot 0.6H_2O$ can be obtained at 110 °C by removing reversibly absorbed water. Thermal treatment at 250 °C clears bond water to produce $V_2O_5 \cdot 0.3H_2O$. Heating at 300 °C leads to the mixture of $V_2O_5 \cdot 0.1H_2O$ and orthorhombic V_2O_5 by removing chemically bound water. The product obtained at 330 °C becomes pure orthorhombic V_2O_5. The content of water in the $V_2O_5 \cdot nH_2O$ xerogel directly determines the distance between two adjacent bilayers, as shown in Figure 2.8c.[116] The xerogel samples with n values from 1.6 to 0.3 show reduced interlayer spacing from 11.74 to 11.15 Å. The interlayer spacing of $V_2O_5 \cdot nH_2O$ is dramatically lowered to 8.43 Å for n = 0.1. Chemically bound water dominates the interlayer spacing of the $V_2O_5 \cdot nH_2O$ xerogel, rather than reversibly absorbed water and bond water. Supercritical extraction of pore liquid from the $V_2O_5 \cdot nH_2O$ xerogel can produce intact and porous $V_2O_5 \cdot nH_2O$ aerogels.[117]

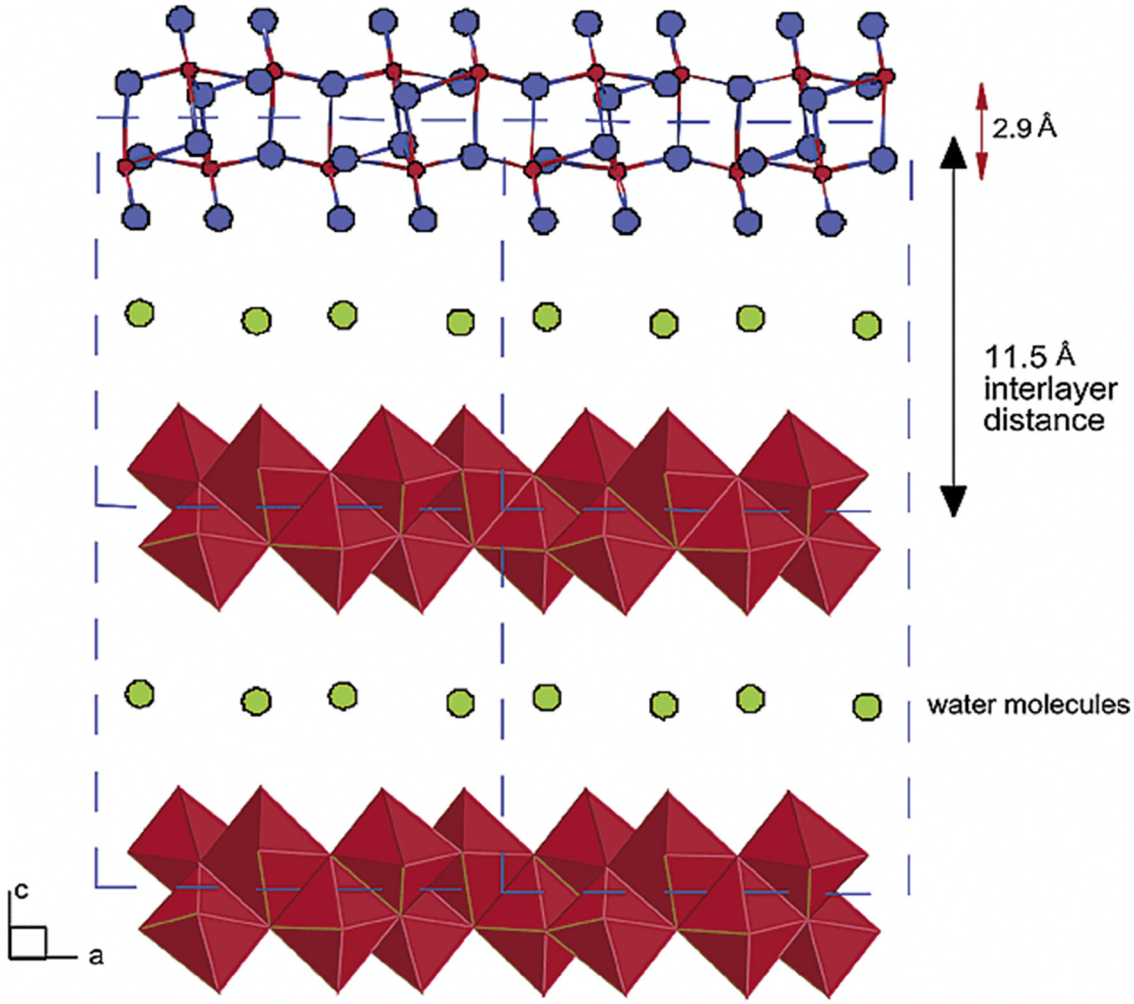

Figure 2.7 The crystal structure of $V_2O_5 \cdot nH_2O$ xerogel in the *ac* plane. Red polyhedrons are VO_6 octahedrons. Green balls are water molecules.[114]

Since the insertions of water molecules can increase the interlayer spacing of $V_2O_5 \cdot nH_2O$, $V_2O_5 \cdot nH_2O$ shows higher specific capacity than that of the orthorhombic V_2O_5. The electrochemical properties of the $V_2O_5 \cdot nH_2O$ are highly associated with the content of residual water. The specific capacities of the $V_2O_5 \cdot nH_2O$ xerogel increase, when the content of residual water decreases from 1.6 to 0.3, shown in Figure 2.8d.[116] Among them, $V_2O_5 \cdot 0.3H_2O$ has the highest capacity, due to the optimal composition that keeps the large interlayer spacing with the least amount of water. However, the $V_2O_5 \cdot nH_2O$ suffers from poor cycling stability, due to the reactions of lithium and residual water to form Li_2O.[118] The porous structure of $V_2O_5 \cdot nH_2O$ easily collapses during battery cycling. In addition, the electrical conductivity of the $V_2O_5 \cdot nH_2O$ xerogel plummets during deep discharge.[115]

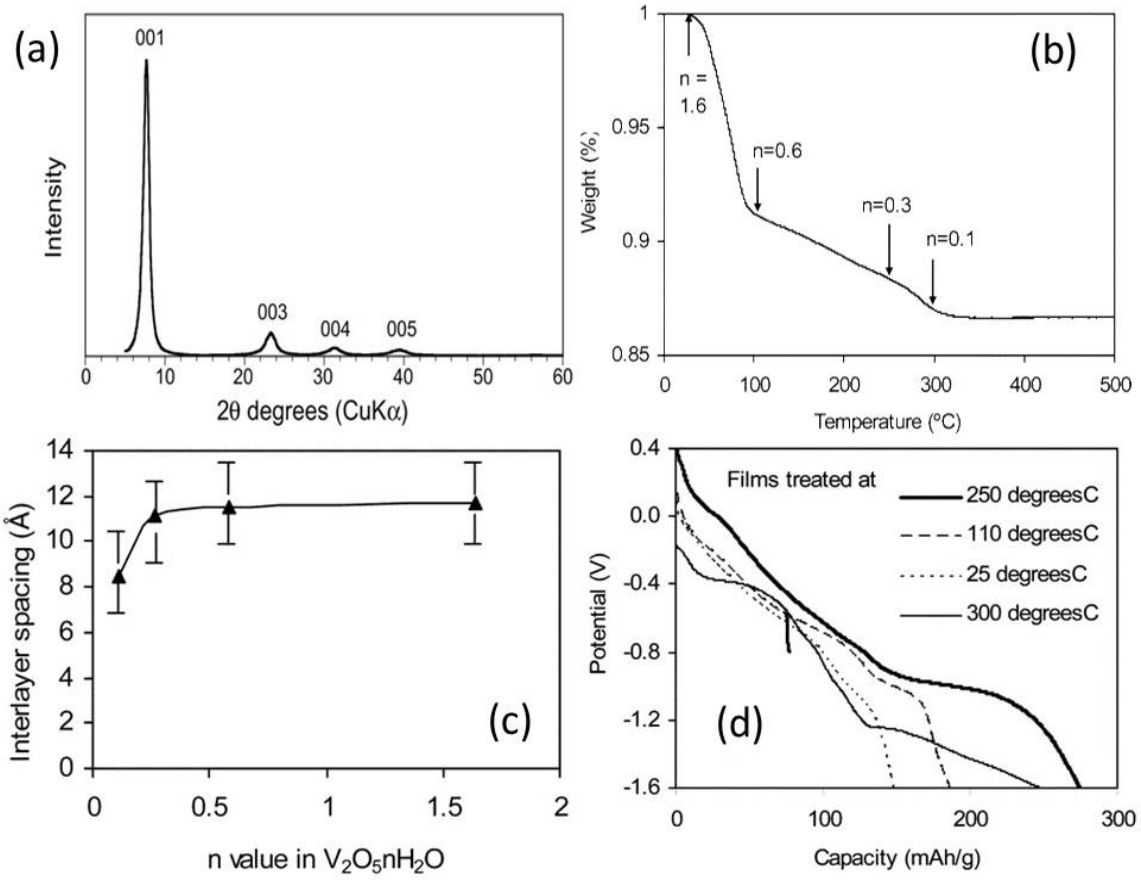

Figure 2.8 (a) XRD pattern and (b) TGA curve of the $V_2O_5 \cdot nH_2O$ xerogel; (c) effect of interlayer spacing on the n value of $V_2O_5 \cdot nH_2O$; (d) Discharge measurements of $V_2O_5 \cdot nH_2O$ xerogels annealed at different temperature with a current density of 100 $\mu A/cm^2$.[114,116]

To achieve a high-performance cathode of vanadium pentoxide for LIBs, a variety of strategies are employed to improve the electrical conductivity, the lithium diffusion coefficient, and the structural stability of V_2O_5. Nanostructure V_2O_5 reduces particle sizes to nanoscale, which shortens the transport path of electrons and lithium ions, and possesses high porosity to buffer volume changes. Due to the highly conductive nature of carbon materials, the carbon-based composites of V_2O_5 can effectively enhance the electric conductivity of the electrode, and hinder the active material from agglomeration in the cycling process. Coating conductive polymers on V_2O_5 is another popular approach that enhances the electrical conductivity of V_2O_5 and protects V_2O_5 from direct contact with the electrolyte.

2.2.2 **Nanostructured V_2O_5**

Nanomaterials have been one of the greatest contributors for the developments of lithium ion batteries, due to the reduced dimensions and the excellent combination of bulk and surface properties.[26,119] A diversity of nanostructured V_2O_5 materials were synthesized to improve the cycling performance and the rate capability. The novel nanostructures of V_2O_5 cover zero-dimensional (0D) nanoparticles,[104] one-dimensional (1D) nanorods[101]/nanoribbons[111]/nanowires[120]/nanotubes[43], two-dimensional (2D) nanosheets,[121] and three-dimensional (3D) hierarchical architectures.[122] The V_2O_5 nanostructures offer many advantages.[26] The short diffusion length facilitates the transport kinetics of electrons and Li^+ ions, leading to high rate capability. The small particle size and the large electrode/electrolyte contact area enhance the utilization of active materials. The high porosity buffers the volume changes caused by Li^+ insertion/extraction.

V_2O_5 nanoparticles (30–60 nm) were prepared by a one-step flame spray pyrolysis process.[104] The optimal sample was obtained by maximizing precursor concentration and injection rate, which showed the highest phase purity of 98 wt% and a specific surface area of ~32 $m^2\ g^{-1}$. When measured as a cathode material for LIBs between 2.5 and 4.0 V, this sample showed excellent cycling performance by keeping a specific capacity of 110 mAh g^{-1} after 100 cycles at a current rate of 10C, and a superior high-rate capacity of 100 mAh g^{-1} at 20C. Sasidharan *et al.* synthesized V_2O_5 hollow nanospheres by a sol-gel method with polymeric micelles as a soft template.[123] Polymer/vandia core-shell particles

were first prepared as precursors. The orthorhombic V_2O_5 hollow spheres were obtained by burning the polymeric cores off at 500 °C in an air atmosphere. The hollow V_2O_5 nanospheres with a diameter of around 28 nm (Figure 2.9) exhibited capacity retention of 92.6% when cycled for 50 cycles at 0.5C in a voltage window of 2-4 V.

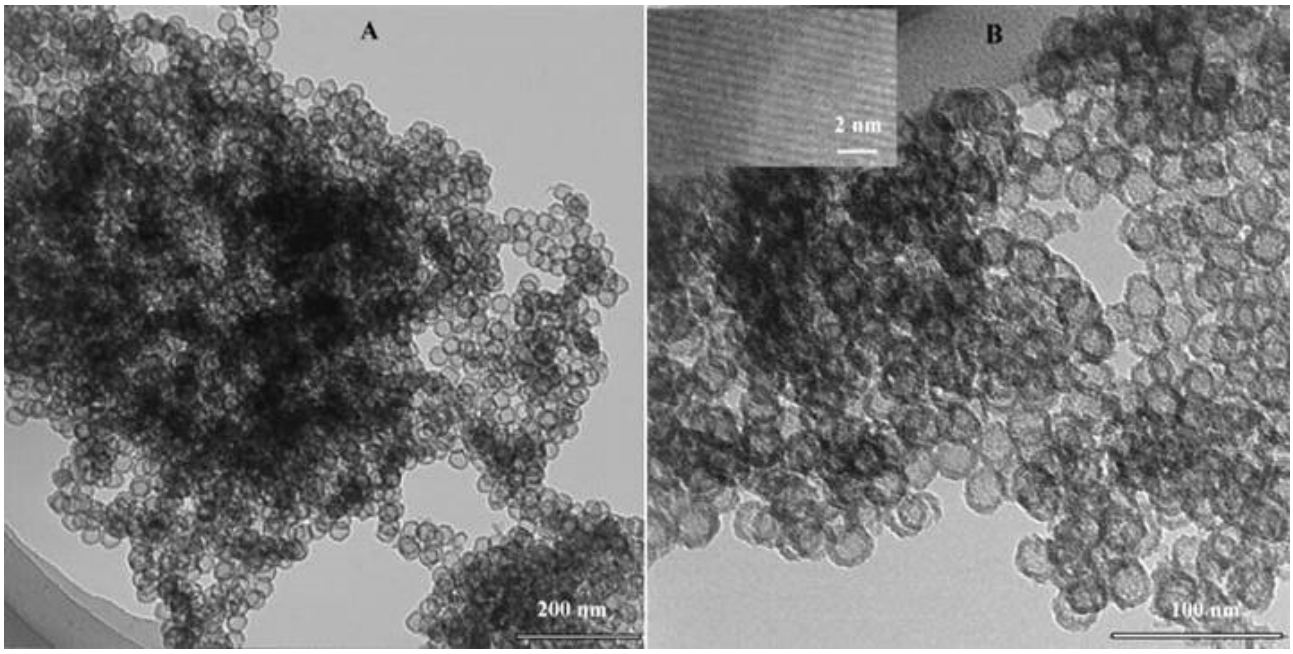

Figure 2.9 TEM images of V_2O_5 hollow nanospheres at different magnifications. A high-resolution TEM image was shown in the inset.[123]

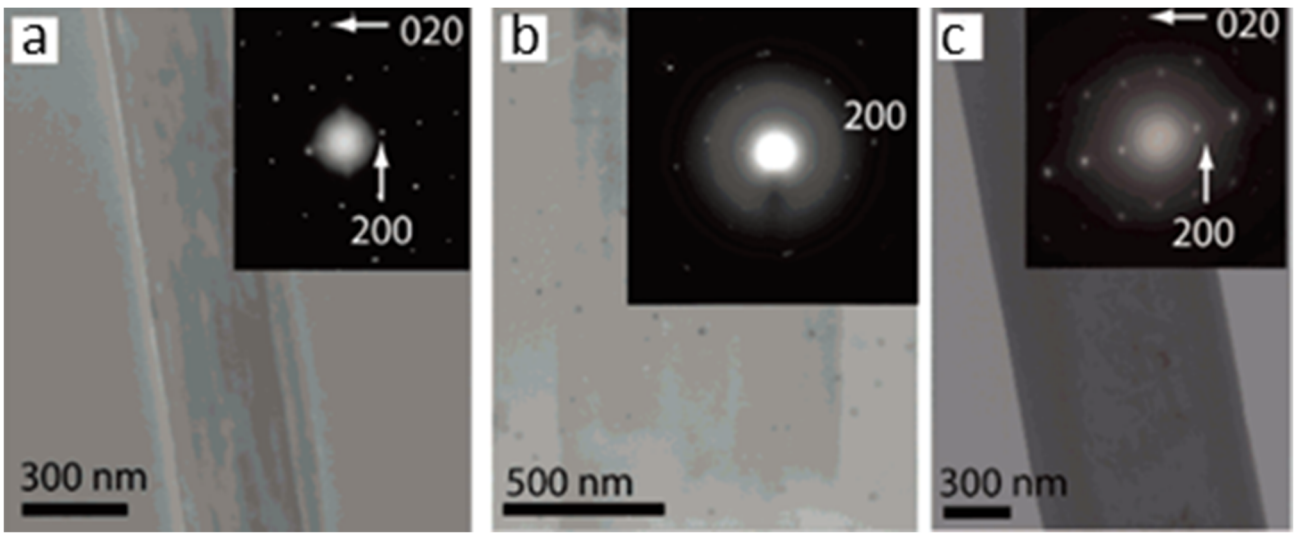

Figure 2.10 (a) HRTEM image of 100 nm thick and 400 nm wide V_2O_5 nanowires treated with BuLi for 10 s. The inset is the SAED pattern along the 〈001〉 axis. The (020) and (200) spots were attributed to the pristine orthorhombic V_2O_5, suggesting no lithium

intercalation. (b) HRTEM image of 20 nm thick and 740 nm wide V_2O_5 nanowires treated with BuLi for 10 s. The ω-$Li_3V_2O_5$ is the primary phase, revealed by the (200) spot shown in the SAED pattern (inset). (c) TEM image of $Li_xV_2O_5$ nanowires treated with Br_2 to remove lithium ions. The SAED pattern (inset) was indexed to the pristine V_2O_5, indicating a full delithiation of $Li_xV_2O_5$ nanowires.[124]

Nanobelts and nanowires are the most studied 1D nanostructure for V_2O_5.[111,120,124-127] Li *et al.* introduced an environmentally friendly technique to synthesize orthorhombic V_2O_5 nanobelts by hydrothermal treatment of the solution of V_2O_5 and H_2O_2.[125] The nanobelts had the fast growth direction of [010] and the lowest growth direction of [001]. The dimensions of the nanobelts were 100−300 nm in width, 30−40 nm in thicknesses, and tens of microns in length. Enhanced specific capacity was observed for this material. Chan *et al.* reported that V_2O_5 nanowires allowed the ω-$Li_3V_2O_5$ phase completely delithiated back to the pristine orthorhombic phase, indicating fully reversibility of lithium insertions/extractions in the V_2O_5 nanowires (Figure 2.10).[124] The full reversibility was able to increase the capacity by 17% and the energy density by 30%. In comparison, the bulk ω-$Li_3V_2O_5$ kept the structure of the ω-phase and retains 0.4 lithium atoms, when fully delithiated. A chemical lithiation method was used to intercalate lithium ions into V_2O_5 nanowires, which offered similar results as electrochemical lithiation. The transformation of V_2O_5 into the ω-$Li_3V_2O_5$ phase was highly affected by the width and the thickness of V_2O_5 nanowires. Narrower nanowires support more lithium to insert into the internal after the formation of the ω-phase on the surface. Thin V_2O_5 nanowires allowed phase transformation to complete within 10 s, the Li diffusion coefficient of which was three orders of magnitude faster than that of bulk V_2O_5. The reason for the faster phase transformation of thin nanowires was that the thin thickness reduced activation barrier of the lattice distortion during lithium intercalations. Zhai *et al.* improved the conditions of hydrothermal treatment and successfully prepared the centimetre-long V_2O_5 nanowires with an aspect ratio of $\sim 10^5$–10^6 (Figure 2.11a).[120] When measured as a cathode material for LIBs, these V_2O_5 nanowires exhibited a high capacity of 351 mAh g^{-1} and a high Coulomb efficiency of 99%. The novel properties of the centimetre-long V_2O_5 nanowires also create great prospects for field-emitters, lithium-ion batteries, photodetectors, interconnects, and optoelectronic devices. The commercialization of V_2O_5 nanomaterials was largely restricted by the difficulty of maintaining high homogeneities for large-scale production. Rui *et al.* developed a cost-effective and green strategy for the scalable preparation of crystalline V_2O_5 nanobelts in ambient conditions.[127] In a typical synthesis

process (Figure 2.11b), a given amount of commercial V_2O_5 powder was thoroughly stirred in an aqueous NaCl solution for 72 hours, which can produce high yield of V_2O_5 nanobelts after centrifugation. The surface area of these nanobelts was 14 times higher than that of the V_2O_5 precursor. There were no templates, surfactants, or expensive precursors (e.g. vanadyl triisopropoxide and vanadium acetylacetonate) involved in the whole process. A dissolution–recrystallization mechanism resulted in the formation of V_2O_5 nanobelts. Basically, partial dissolution of V_2O_5 particles in NaCl solution generated free vanadium(V) species including $[V_{10}O_{28}]^{6-}$ and VO_2^+. These vanadium species recrystallize at an adequate concentration and create crystalline V_2O_5 nuclei on the surface of V_2O_5 particles. The depositions on the seeds gradually grow into pure [010]-oriented V_2O_5 nanobelts. Binder-free bulky papers were fabricated by the intertwining V_2O_5 nanobelts with the acid-treated multi-walled carbon nanotubes. As for LIBs, the bulky paper electrode exhibited excellent high-rate performance by delivering 144 mAh g^{-1} at 20 C.

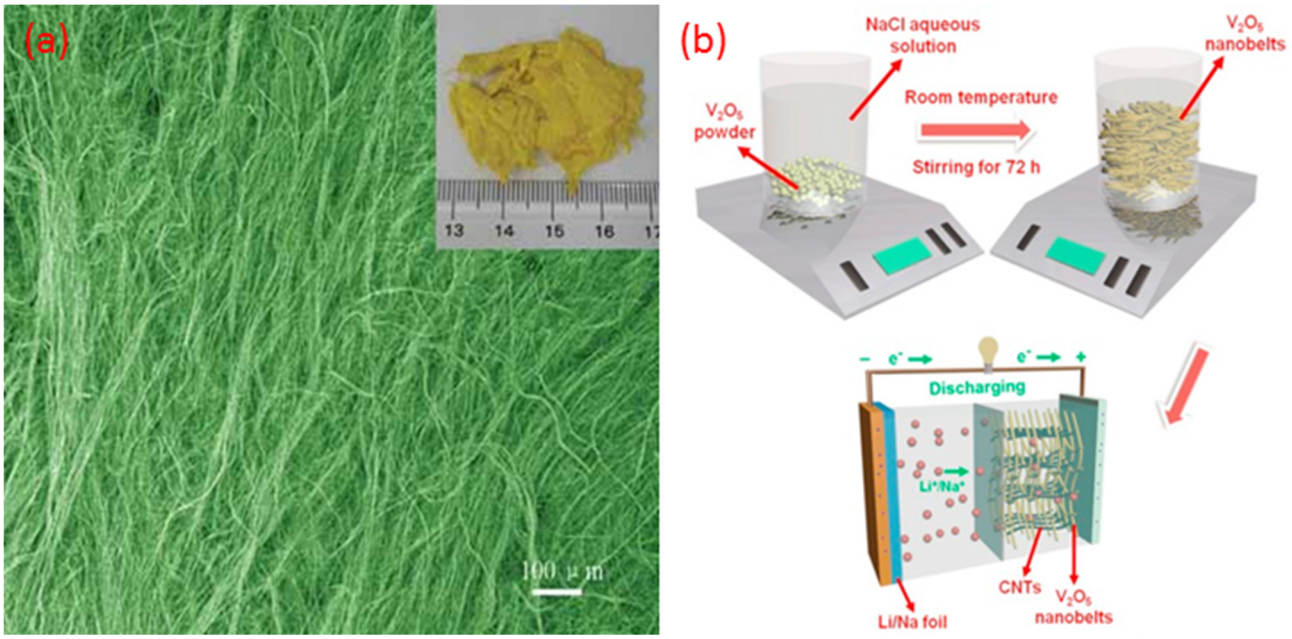

Figure 2.11 (a) SEM image and a photograph (inset) of the centimeter-long V_2O_5 nanowires;[120] (b) Schematic diagram of the scalable synthesis of V_2O_5 nanobelts at room temperature as cathode materials for LIBs.[127]

Other 1D nanostructures, such as nanorods, nanotubes, and nanofibers were also investigated for V_2O_5.[128-131] Takahashi *et al.* synthesized V_2O_5 nanorod arrays by electrochemical deposition, using $VOSO_4$ aqueous solution and polycarbonate membrane template.[128] The V_2O_5 nanorods exhibited uniform growth along the same direction in a

large area, which had a length of around 10 μm and diameters of 100 - 200 nm. The electrochemical properties of the nanorod arrays were investigated in comparison with sol−gel-derived V_2O_5 films. The current density and energy storage density of the V_2O_5 nanorods were 5 times higher than those of the sol−gel-derived film. Similar procedures of electrochemical deposition can also be used to grow V_2O_5 nanotube arrays by applying lower voltages and shorter deposition time.[131] Due to the large surface area and short diffusion lengths, the as-prepared nanotube arrays showed an initial capacity of 300 mAh g^{-1}, which is double that of the amorphous V_2O_5 films. Yu *et al.* reported porous V_2O_5 nanofibers with greatly improved lithium storage capacity of 370 mAh g^{-1}.[129] Sol–gel and electrospinning were combined to synthesize the V_2O_5 nanofibers. The V_2O_5 nanofibers with a diameter of around 350 nm were constructed by interconnected nanoparticles. The specific surface area of the V_2O_5 nanofibers is ~97 m^2 g^{-1}.

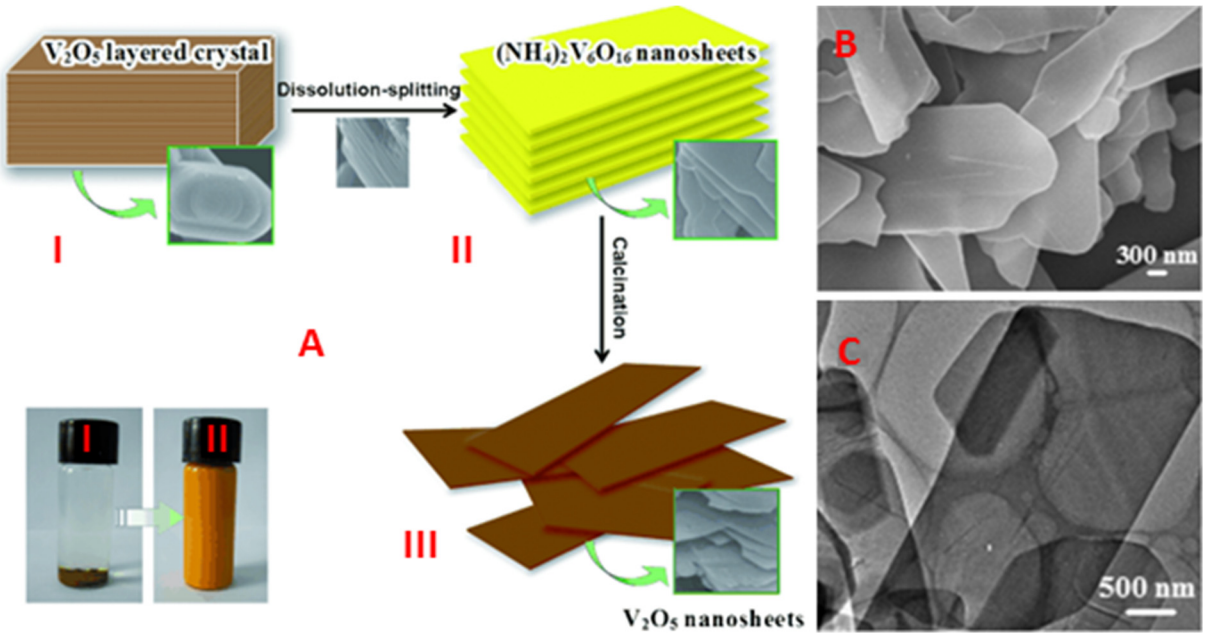

Figure 2.12 Schematic illustration (A) of the synthesis of V_2O_5 nanosheets by a dissolution–splitting method. SEM image (B) and TEM image (C) of $(NH_4)_2V_6O_{16}$ nanosheets.[121]

The synthesis of 2D V_2O_5 nanosheets has been explored with various strategies.[109,121,132,133] Inspired by the exfoliation of layered graphite into graphene, the nanosheets of metal oxides might also be obtained from the peeling-off of a bulk crystal with a layered structure. Wang *et al.* successfully synthesized V_2O_5 nanosheets from the exfoliation of layered V_2O_5 bulk crystals by a dissolution–splitting method.[121] The

synthesis procedures were illustrated in Figure 2.12. The water solution of commercial V_2O_5 power and ammonium persulfate (APS) was uniformly mixed by stirring for 48 h at 50 °C. The NH_4^+ ions of APS are inserted into the interlayer spaces of the V_2O_5 crystals, generating an intercalated compound $(NH_4)_2V_6O_{16}$. As amphoteric $(NH_4)_2V_6O_{16}$ is easily dissolved in an acid environment of $S_2O_6^{2-}$, nanosheets were gradually exfoliated from bulk crystals in a splitting process. The precursor of $(NH_4)_2V_6O_{16}$ nanosheets was transformed into V_2O_5 nanosheets after annealing. The V_2O_5 nanosheets had thin thickness of 10–20 nm. The by-products exhibited improved lithium storage performance including high specific capacity (290 mAh g^{-1}), stable cycling, and good rate performance (144 mAh g^{-1} at 10 C and 95 mAh g^{-1} at 20 C). Liang *et al.* employed a bottom–up solvothermal approach to synthesize ultra-large VO_2(B) nanosheets with a lateral size over 100 μm, which is the largest nanosheets ever reported.[133] The VO_2 nanosheets were composed by 3-8 stacked layers that had an ultrathin thickness of 2–5 nm. The use of isopropanol is essential for the formation of nanosheet structures. After annealing, the VO_2 nanosheets can be transformed into the V_2O_5 nanosheets with well-retained sheet structures (Figure 2.13). When used as a cathode for LIBs, the V_2O_5 nanosheets showed excellent rate capability and cycling performance. The voltage window was selected between 2.5 and 4 V, which allowed a maximum of one lithium intercalation. The V_2O_5 nanosheets not only possessed a capacity of 106 mAh g^{-1} at an ultra-high current density of 5 A g^{-1}, but also achieved a capacity fading of 92.6% for 500 cycles at the current density of 1.5 A g^{-1}. In order to make large-scale production, a facile, green, and low-cost approach was developed to synthesize leaf-like polycrystalline V_2O_5 nanosheets.[132] The nanosheets were built by smaller nanorods. In a typical synthesis, the diluted solution of V_2O_5 powders and H_2O_2 was treated by stirring and ultrasonication to form a V_2O_5 gel. This V_2O_5 gel was further diluted, freeze-dried, and annealed at 450 °C in air to acquire the V_2O_5 nanosheets. As for the electrochemical properties for LIBs, the leaf-like V_2O_5 nanosheets outstood with high reversible capacity, excellent rate capability, and good cycling stability.

However, low-dimensional nanostructures face many challenges, when the sizes are reduced to nano-scale. Self-aggregation is a common problem for nanomaterials, due to high surface energy.[134] Low tap density caused by high porosity is directly responsible for small volumetric energy density and thick electrodes.[135,136] Thick electrodes bring difficulties for electrolyte penetration and maintaining conductive paths. The large electrolyte/electrode contact also induces more side reactions and poor thermal stability,

resulting in safety hazards and poor cycling stability.[137] Fabricating hierarchical 3D superstructures is a promising strategy to ease these problems. Nanostructures are used as basic blocks to further build a hierarchical 3D superstructure, which can possess the advantages of both nano-sized primary particles and micron-sized secondary particles.[138-141] Hierarchical nanostructures also show strong structural stability for volume changes during charging and discharging.

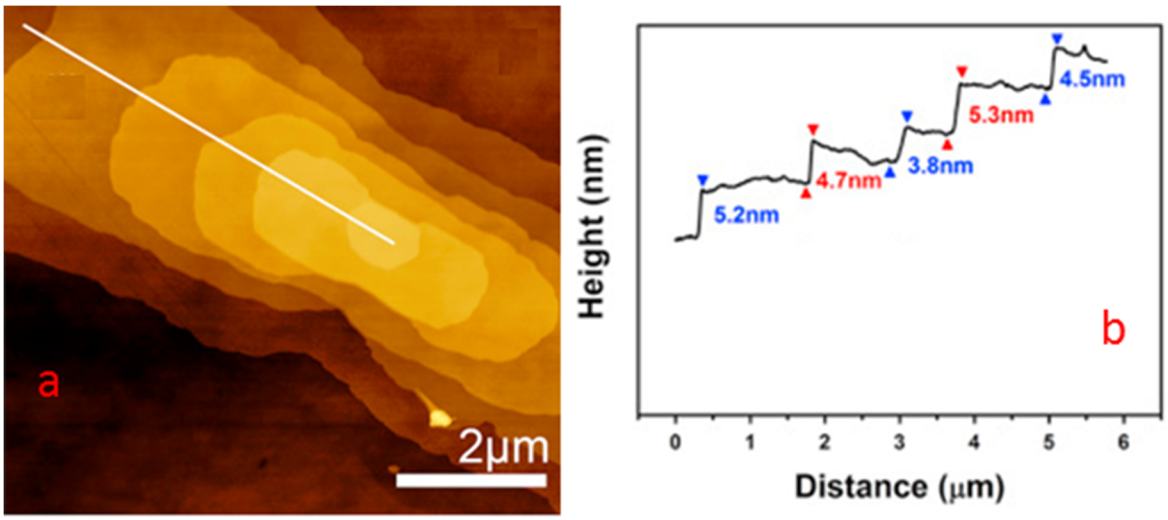

Figure 2.13 AFM image (a) and height profile (b) of the V_2O_5 nanosheets with multi-layer stacking structure. The height profile in figure b corresponds to the white line in the figure a. The parallel stacked layers nanosheets have about 3–5 nm in thickness.[133]

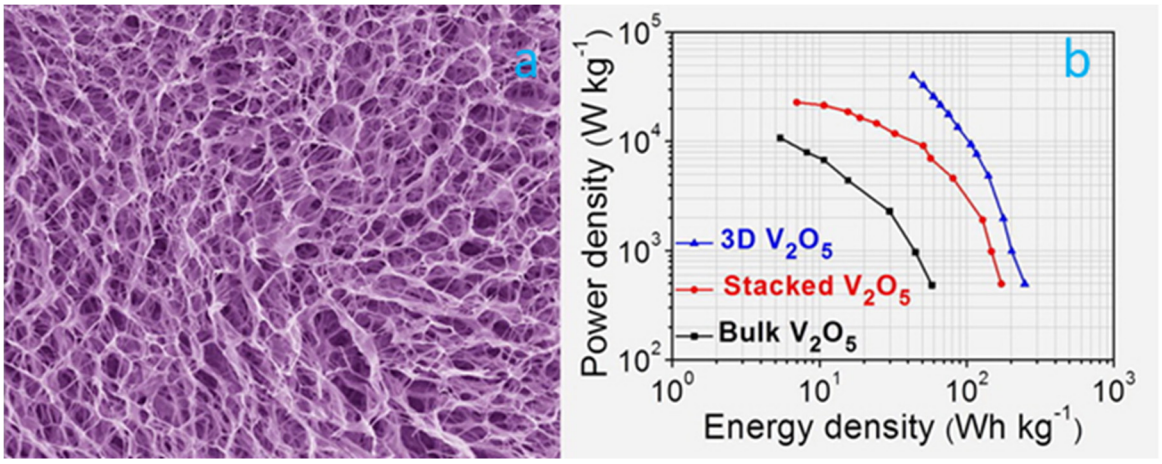

Figure 2.14 (a) FESEM image of the hierarchical 3D V_2O_5 sponge superstructure built by highly interconnected V_2O_5 nanosheets. (b) The dependences of power densities on energy densities of 3D V_2O_5, stacked V_2O_5 film, and bulk V_2O_5 electrodes. The stacked V_2O_5 film was prepared by drying in a conventional vacuum oven.[142]

A hierarchical V_2O_5 sponge superstructure was built by highly interconnected V_2O_5 nanosheets (Figure 2.14a).[142] This hierarchical structure had multilevel pores, ultrathin pore walls, and a high surface area of 133 m^2 g^{-1}. The pore sizes ranged from several microns to tens of microns. The ultrathin V_2O_5 nanosheets possessed a thickness of 4 nm and lateral dimensions from 500 nm to micrometers. An efficient strategy combining hydrothermal treatment and freeze-drying was employed to synthesize this hierarchical material by using raw chemicals of only V_2O_5 powder and diluted H_2O_2. The interconnected V_2O_5 nanosheets were formed during the hydrothermal process. The subsequent freeze-drying generated the porous hierarchical structure by subliming ice. This robust and porous superstructure offered resistance of aggregation, fast electrolyte penetration, large electrolyte/electrode contact, and ease of strains caused by volume changes. Therefore, this material achieved the highest electrochemical performance ever reported, when used as an electrode for supercapacitor. The capacitance retention kept over 90% after 4000 cycles. The large energy density of 107 Wh kg^{-1} was matched with a high power density of 9.4 kW kg^{-1} (Figure 2.14b).

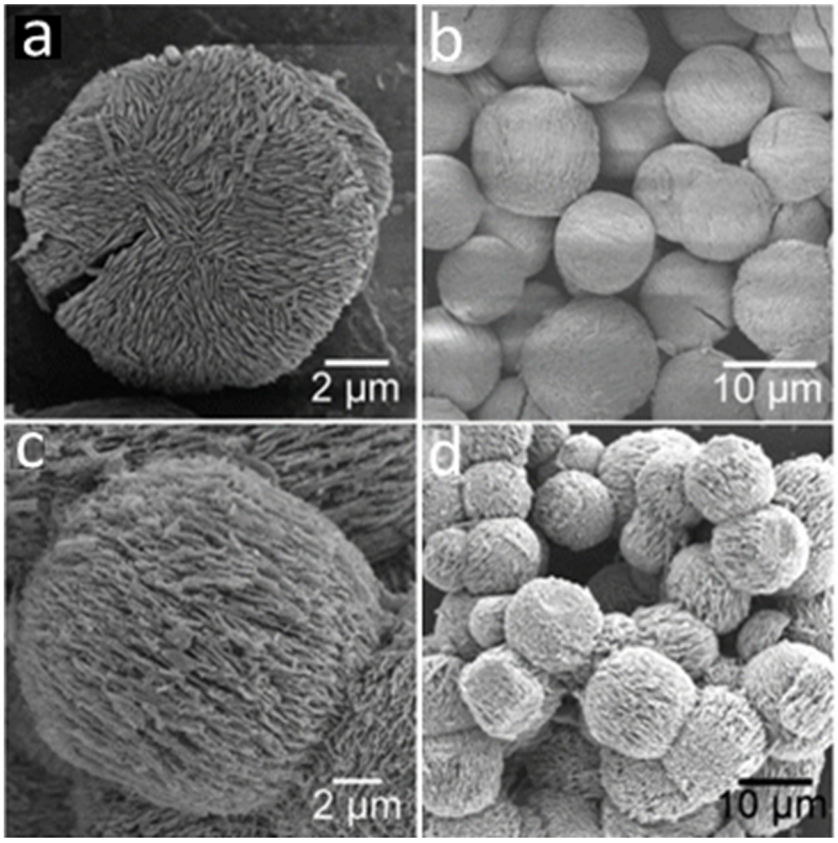

Figure 2.15 FESEM images of 3D porous V_2O_5 microspheres before (a-b) and after (c-d) annealing. The microspheres were comprised of highly oriented nanofibers.[143]

A facile synthesis of 3D porous V_2O_5 microspheres was realized by an additive-free solvothermal method.[143] The precursor microspheres with diameters of 4-10 μm were comprised of highly oriented nanofibers (Figure 2.15). The porous V_2O_5 microspheres were formed after calcination, which well preserved the structures of the precursor microspheres. During the synthesis process, nanofibers were quickly formed within 5 mins. To reduce the overall surface energy, the nanofibers self-aggregated into fan-like structures within 15 mins. The continuing aggregation trended to have preferred alignments, which finally turned intermediate structures into porous V_2O_5 microspheres in 1.5 h. Due to the 3D hierarchical structure, these V_2O_5 microspheres performed a slow capacity fading with a capacity of 130 mAh g^{-1} for the 100th cycle at 0.5C and excellent high-rate capability with 105 mAh g^{-1} at 30C.

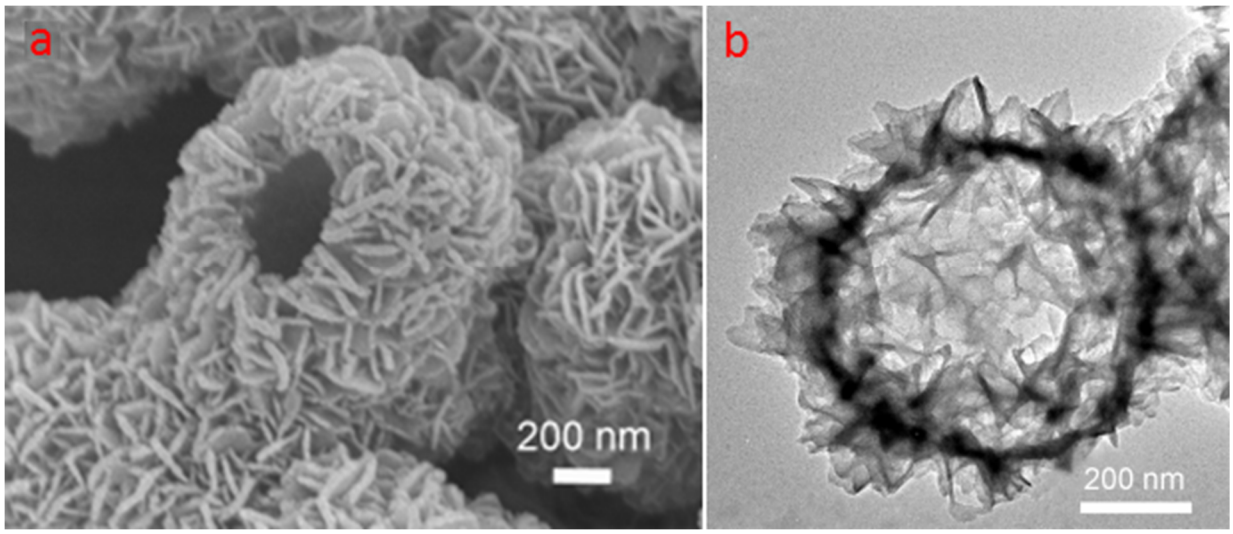

Figure 2.16 (a) FESEM and (b) TEM images of the precursor of hierarchical V_2O_5 hollow microspheres prepared by a solvothermal method at 200 °C for 12 h. The composition of the raw solution included VOC_2O_4 (2 mL, 0.0825 M) and ethylene glycol (20 mL).[140]

Hierarchical V_2O_5 hollow microstructures is another 3D nanostructure attracting extensive research interest, as their hollow interiors and porous shells can offer large free volume for easy electrolyte penetration and even distribution of the strains induced by volume changes.[122,144,145] Pan *et al.* introduced a simple template-free solvothermal method to synthesize hierarchical V_2O_5 hollow microspheres, the shells of which were assembled by nanosheets.[140] The structural evolution process was controlled by the inside-out Ostwald-ripening mechanism. Solid microspheres were formed by the interaction between VOC_2O_4 and ethylene glycol. In order to lower the overall surface energy, the interior material

preferred being dissolved and recrystallized as nanosheets on the exterior surfaces. Hollow precursor microspheres were completely composed of nanosheets after adequate reaction time (Figure 2.16). The microspheres have a diameter of about 1 μm, while the nanosheets showed a thickness of around 20 nm and a size of nearly 200 nm. The hollow precursor microspheres can be annealed to easily form V_2O_5 hollow microspheres without obvious structural changes. When used as cathode materials for LIBs, the hierarchical V_2O_5 hollow microspheres nearly reached theoretical capacity, and exhibited high rate capability as well as excellent cycling stability.

2.2.3 **Carbon modified V_2O_5**

Surface modification of V_2O_5 with conductive carbon materials has been a dominating strategy to promote the battery performance of V_2O_5.[36,106,146-150] Porous carbon, carbon nanotube, and graphene are widely used carbonaceous materials. These carbon materials provide fast channels for electron transportation and enhance the electrical conductivities of electrodes. The surface carbon coating can effectively reduce side reactions, prevent the agglomeration of active materials, and restrict volume changes during cycling.[151,152] The compact contacts between carbon and V_2O_5 can facilitate the access of charge carriers to active materials.[153]

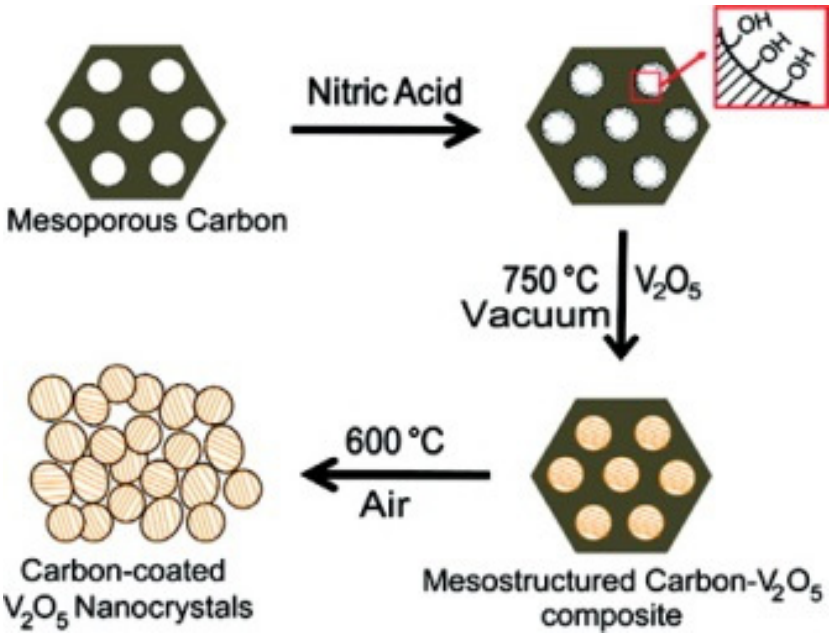

Figure 2.17 Schematic illustration for the synthesis carbon-coated V_2O_5 nanocrystals with mesoporous carbon as a hard template by a capillary-induced filling approach.[36]

Porous carbon with an ordered mesoporous structure was utilized as a hard template to synthesize carbon-coated V_2O_5 nanocrystals by a capillary-induced filling approach.[36] The synthesis procedures were illustrated in Figure 2.17. The porous carbon had an average pore size of 3.8 nm and a high surface area of 1048 m^2/g, which was first treated with concentrated nitric acid to generate -OH and -COOH functional groups on the surface. The mixture of V_2O_5 and the treated porous carbon was calcinated in vacuum with a temperature of 750 °C. As V_2O_5 started to melt from 690 °C, the strong capillary force attracted the liquid V_2O_5 into the mesopores of the hard template. A mesostructured carbon/V_2O_5 composite was formed after natural cooling. A process of removing most carbon was conducted at 600 °C in air to obtain carbon-coated V_2O_5 nanoparticles. The V_2O_5 nanoparticles with diameters of 10 to 20 nm were covered by a 2 nm thin layer of carbon. These carbon coated V_2O_5 nanocrystals showed an outstanding rate performance with 130 mAh g^{-1} preserved at 68C in a voltage window of 2-4 V. Odani *et al.* prepared the core/cell composites of V_2O_3/carbon by heating $VO(OC_2H_5)_3$ at 700 °C under autogenic pressure in a sealed vessel.[153] The V_2O_3 nanoparticles (30–100 nm) were uniformly coated with by a 15 nm thick layer of carbon. These V_2O_3/carbon composites were annealed at 400 °C in air to form V_2O_5 nanoparticles coated with a thin carbon layer (4 nm in thickness). The carbon coating was composed of disordered graphene layers with an interlayer spacing of 3.8 Å, which allowed lithium ions easily pass through the carbon shells. The carbon-coated V_2O_5 nanoparticles didn't require any additional conductive agents for electrode fabrication, leading to an enhanced specific capacity close to its theoretical value. The cycling and rate performance of the carbon-coated V_2O_5 nanoparticles was also better than those of the nanoparticles without carbon coating.

Carbon nanotubes (CNTs) are unique one-dimensional carbon nanomaterials combining many superior properties such as excellent electric/thermal conductivity, low density, strong mechanical strength, and high chemical stability.[154-158] Integrating nanostructures with carbon nanotubes (CNTs) has also been an attractive strategy to improve the electrochemical properties of V_2O_5.[146,147,149,159,160] Hybrid nanocomposites can offer advanced performance that is not possessed by an individual component. The V_2O_5 nanostructures can be composited with CNTs by filling in the interior of CNTs,[160] coating on the surface of CNTs,[159] or intertwining CNTs.[147] An interpenetrative nanocomposite of ultra-long CNTs and V_2O_5 nanowires was prepared as freestanding and highly robust electrode materials for flexible LIBs, which are promising in wearable devices and roll-up displays.[147] A facile in situ hydrothermal treatment method was used to generate the

interpenetrative growth of V_2O_5 nanowires through the meshes of CNT networks, after the uniform dispersion of CNTs in the precursor solution (Figure 2.18). The subsequent vacuum filtration fabricated the precipitate into a robust freestanding composite film, which met the requirements of a high-performance electrode material with high rate capability and excellent cycling stability. The CNTs offers fast transport paths for electrons, while V_2O_5 nanowires reduce the diffusion lengths for lithium ions. The voids within the interpenetrative network facilitate the easy penetration of electrolyte. In addition, the robust network increases the structural stability of the freestanding electrode.

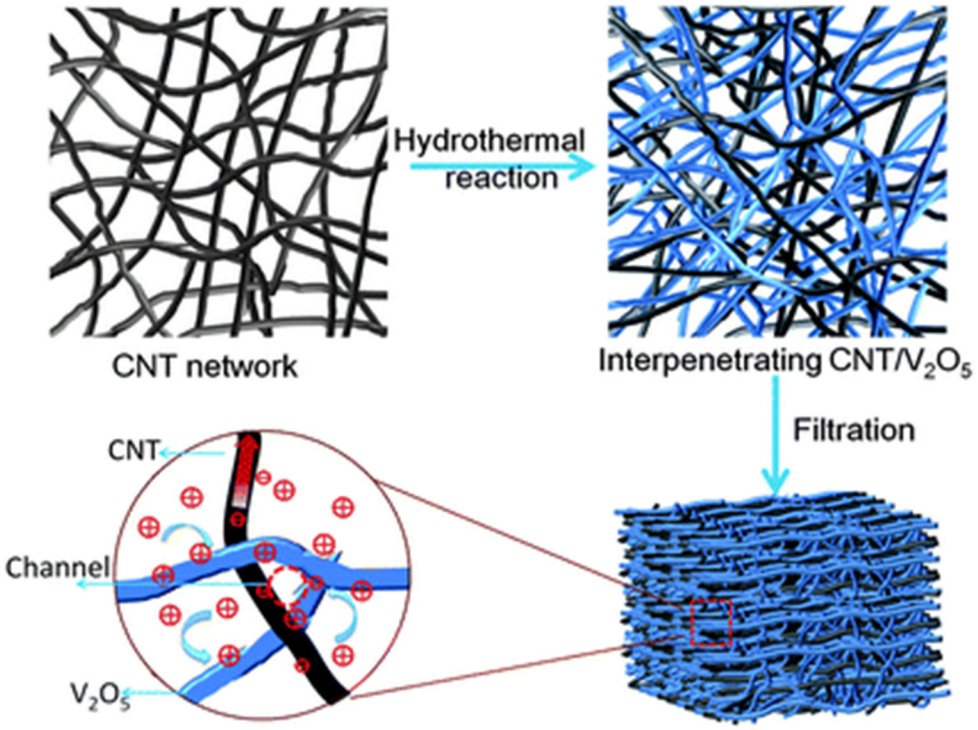

Figure 2.18 Schematic diagram of synthesizing the nanocomposites of interconnected carbon nanotubes and V_2O_5 nanowires.[147]

Chen *et al.* developed a MWCNT/V_2O_5 core/shell sponge as promising LIB cathode material with high areal capacity and power density.[159] As shown in Figure 2.19, the MWCNT sponge served as a structural backbone and nanostructured current collector, on which uniform V_2O_5 coating with 17 nm in thickness was deposited by an atomic layer deposition (ALD). This MWCNT/V_2O_5 sponge is favorable for fast electron transport, short lithium diffusion, and easy electrolyte penetration. The areal capacity of the MWCNT/V_2O_5 sponge was as high as 816 μAh/cm^2 at 1C rate (1.1 mA/cm^2) in a voltage range of 4.0–2.1 V, which was 450 times that of a planar V_2O_5 thin film. At a high current rate of 50C (55.9

mA/cm^2), this composite preserved the areal capacity of 155 μAh/cm^2, leading to a high power density of 21.7 mW/cm^2. Therefore, the MWCNT/V_2O_5 core/shell sponge is an exceptional thin film cathode for LIBs with high robustness and energy-power.

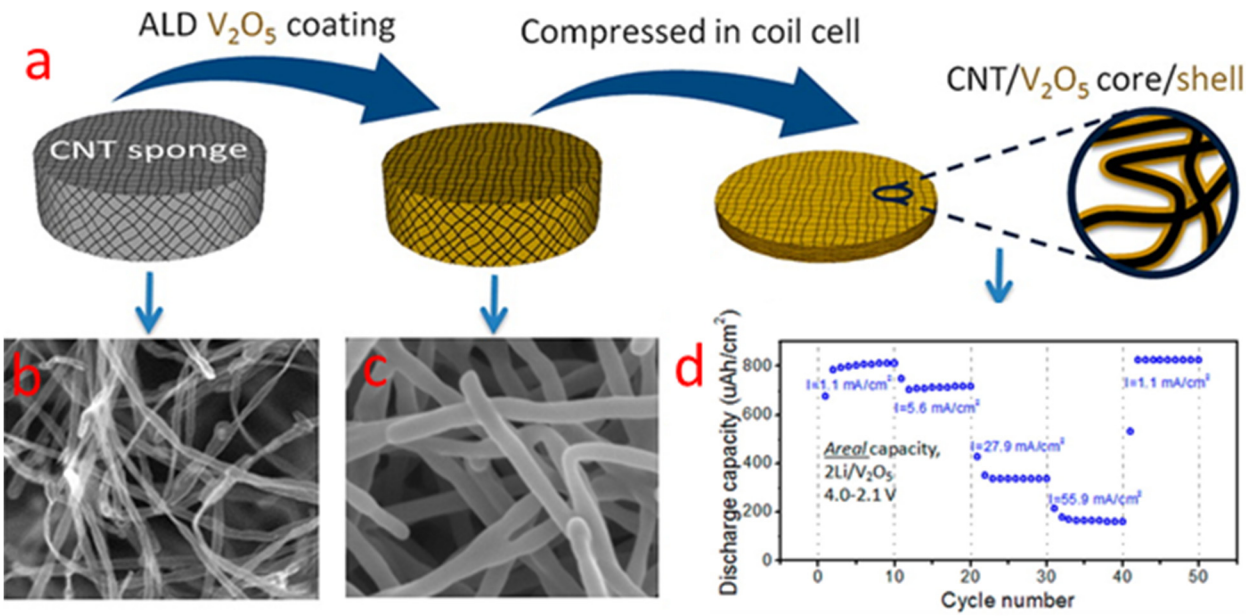

Figure 2.19 (a) Schematic illustration of the synthesis of V_2O_5-coated MWCNT sponge. The thickness of the sponge is reduced from 2 mm to 170 μm after compression in coin cell. SEM images of MWCNT sponge before (b) and after (c) 1000 cycles of atomic layer depositions of V_2O_5. Rate performance (d) of the MWCNT/V_2O_5 sponge in the voltage range of 4.0–2.1 V at different current densities.[159]

A novel nanostructured composite with efficient mixed-conducting networks was achieved by introducing V_2O_5 nanoparticles into carbon tube-in-tube (CTIT).[149] In the CTIT, a new tube is self-assembled by exfoliated carbon along the original carbon nanotube as a hard template. This V_2O_5/CTIT composite simultaneously created an electronic pathway and a lithium-ion pathway, where CTITs not only serve as electronic wires that facilitate the transport of electrons, but also provide the channels for the electrolyte easy access to active materials (Figure 2.20a). In a typical synthesis, an aqueous solution of vanadate oxalate penetrated into CTIT in virtue of the capillary force of the nanotubes. The following heat treatment in air at 400 °C for 2 h led to the crystallization of V_2O_5 nanoparticles. CTITs worked as nanoreactors by use multiple channels to confine the growth of V_2O_5 nanoparticles. The majority of nanoparticles were formed in the interiors of the CTITs, while some large V_2O_5 particles were attached on the exterior surfaces (Figure 2.20b). The mixed-conducting nanostructure greatly shortens the diffusion length of lithium ions and

supports the high rate performance for LIBs. The V_2O_5/CTIT composite can cycle at a high current rate of 40C with a preserved capacity of 90 mAh g^{-1}.

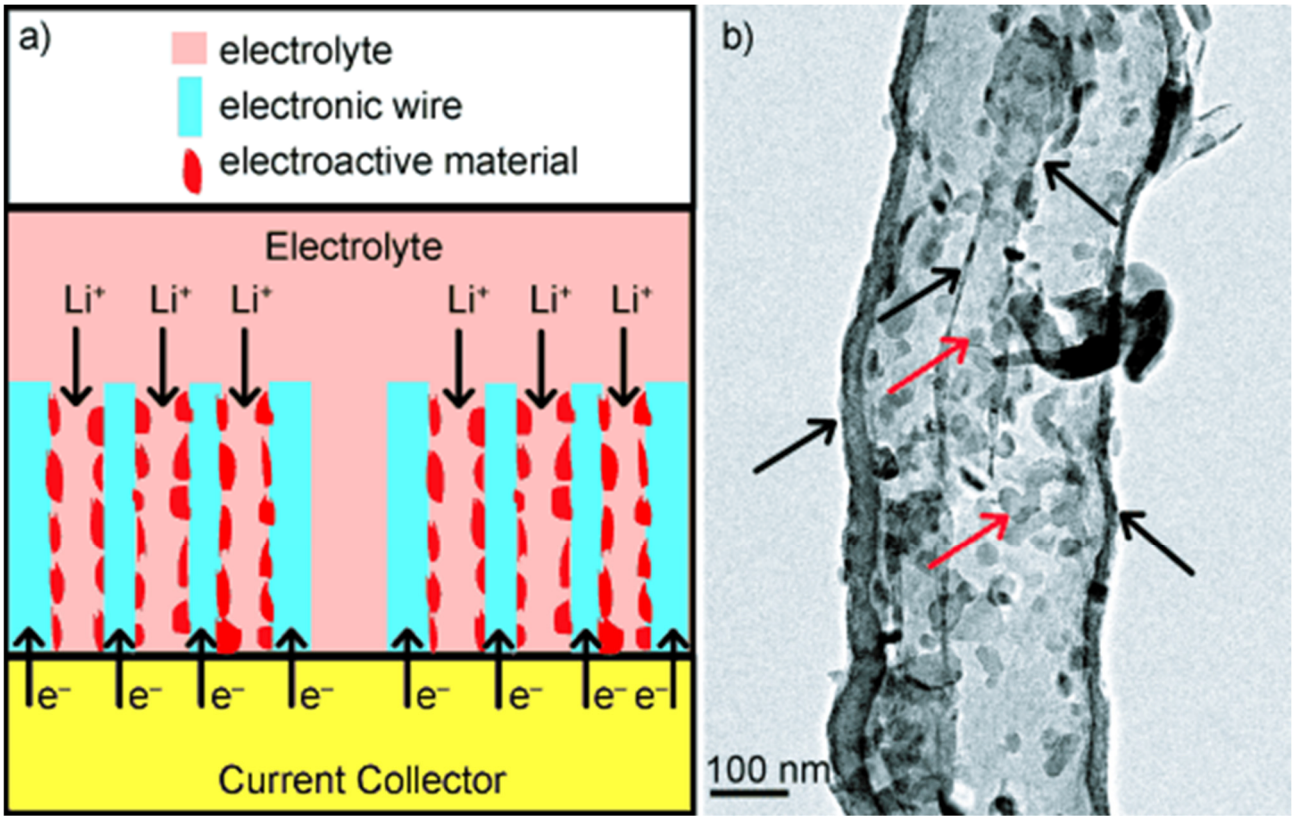

Figure 2.20 (a) Schematic illustration of the novel efficient dual-conducting network in the V_2O_5/carbon tube-in-tube composite. (b) TEM image of the V_2O_5/carbon tube-in-tube composite, where the most V_2O_5 nanoparticles were encapsulated within carbon tube-in-tube. The red and black arrows represent V_2O_5 nanoparticles and the walls of carbon tube-in-tube.[149]

Another excellent 1D composite structure encapsulated V_2O_5 nanosheets into a carbon nanotube by the method of combining electrospinning and chemical vapor deposition (CVD).[160] The carbon nanotubes encapsulating V_2O_5 nanosheets (V_2O_5@G) have diameters of around 150 nm and lengths of several microns, which were interwoven to form a flexible web (Figure 2.21). The preparation of V_2O_5@G started with producing precursor nanowires by the electrospinning of polyvinyl pyrrolidone solution containing a vanadium source and tetraethylorthosilicate. Layered graphitic carbon with average thickness of 5 nm was then deposited on the precursor nanowires in the presence of methane at 1070 °C in a CVD process (Figure 2.21e). Due to the good electric conductivity and mechanical strength, the film of V_2O_5@G web was directly used as a freestanding

electrode for flexible LIBs. This freestanding electrode showed ultra fast and stable Li-ion storage performance. It retained a capacity of over 90 mAh g^{-1} at a high rate of 100C, and also showed a small capacity fading of 0.04% per cycle over 200 cycles. Noteworthy, an energy density of ca. 360 W h kg^{-1} at a power rate of 15.2 kW kg^{-1} is one of the best results ever reported for V_2O_5-based cathode materials.

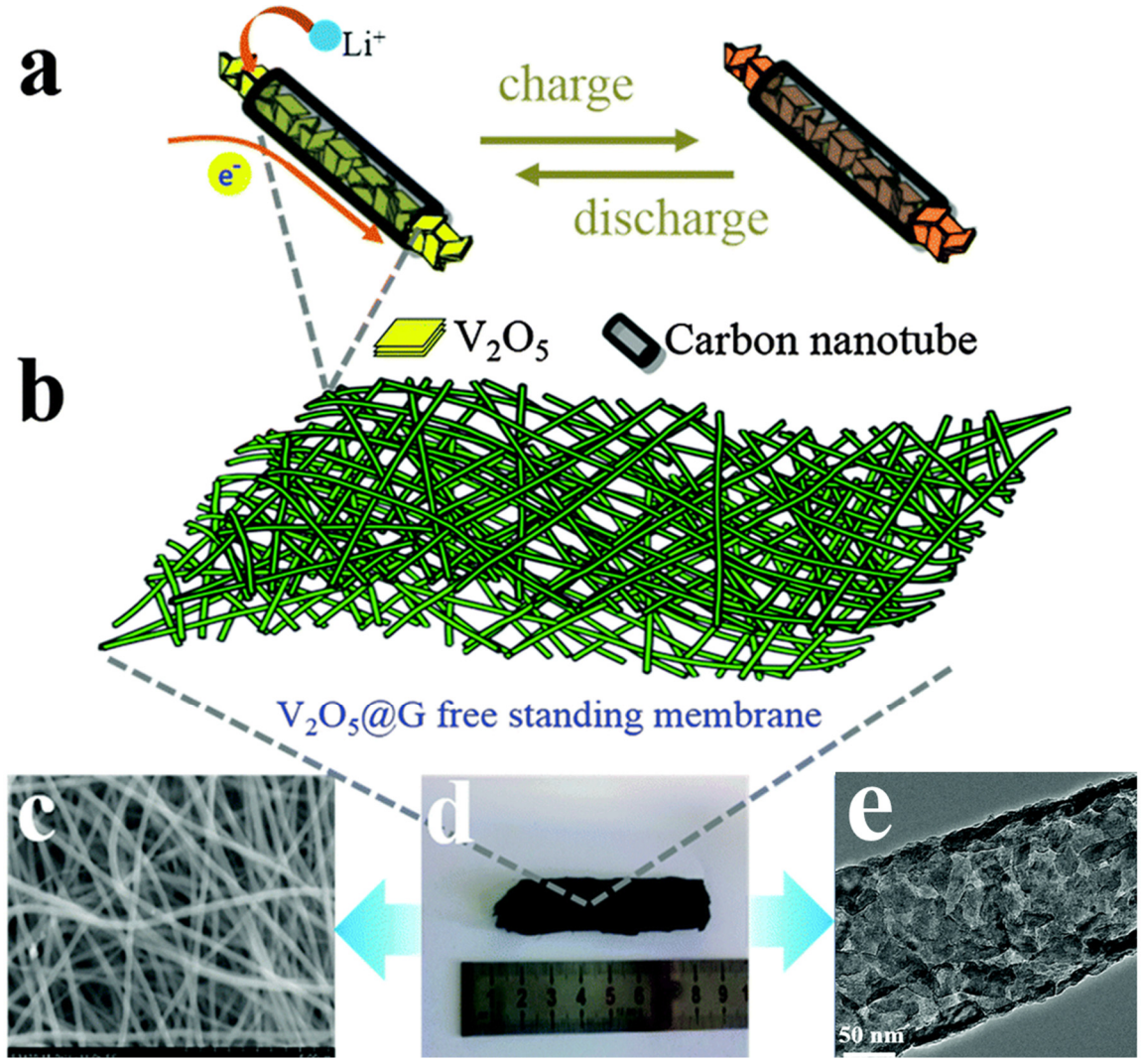

Figure 2.21 (a) Schematic illustration of a carbon nanotube encapsulating V_2O_5 nanosheets (V_2O_5@G). (b) Schematic illustration of the flexible V_2O_5@G membrane interwoven by nanocables. (c) SEM image and (d) photograph of the V_2O_5@G membrane. (e) TEM image of a V_2O_5@G nanocable.[160]

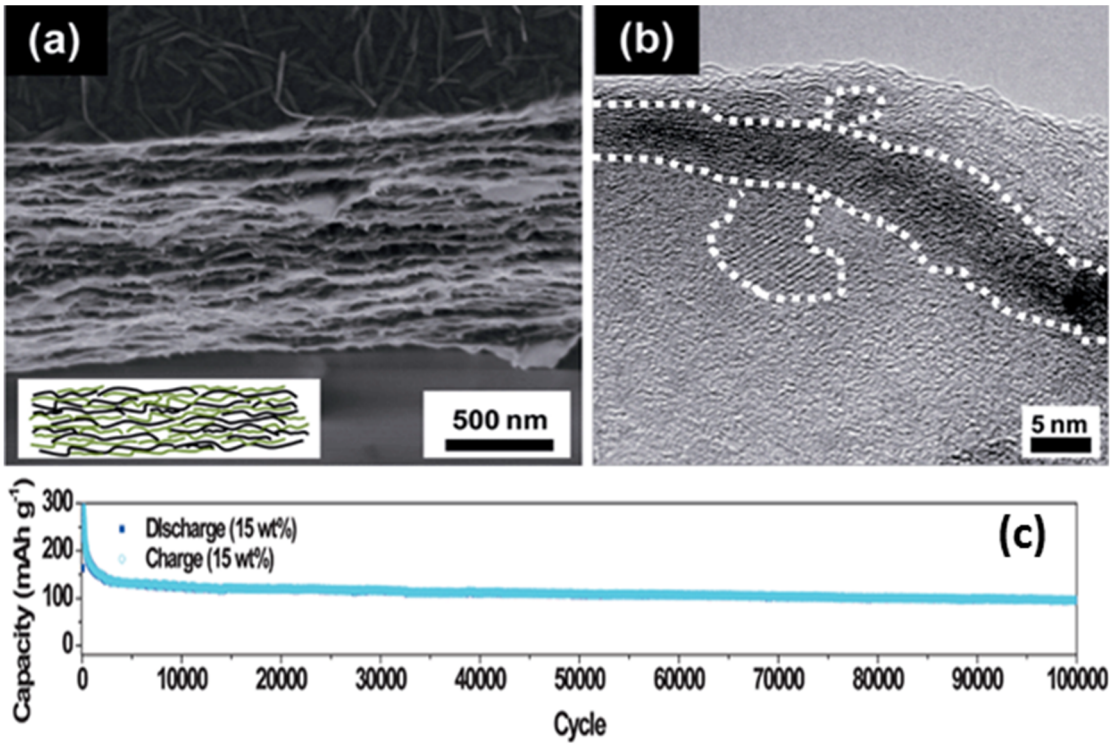

Figure 2.22 (a) SEM image of the cross-section of the V_2O_5 nanowire–GO composite paper. The inset is a schematic illustration for the uniform distribution of graphene nanosheets (black) and V_2O_5 nanowires (green) within the composite paper. (b) HRTEM image of the V_2O_5 nanowire–GO composite paper. A V_2O_5 nanowire (dashed lines) was laid on a GO nanosheet. (c) Cycling performance of the V_2O_5 nanowire–graphene (15 wt%) composite paper measured with a current density of 10000 mA g^{-1} between 1.7 V and 3.8 V for 100000 cycles.[161]

Graphene is a monolayer carbon sheet with the honeycomb (hexagonal) lattice of sp^2-bonded carbon atoms.[162] Graphene has been considered as an extraordinary carbon since its discovery, due to the high electric conductivity of 10^3–10^4 S m^{-1}, the ultrahigh surface area of 2630 m^2 g^{-1}, strong mechanical strength, and high chemical stability.[163] Graphene also has several derivatives, such as graphite oxide, graphene oxide (GO), and reduced graphene oxide (rGO). In the process of chemical oxidation, bulk graphite is first oxidized to hydrophilic graphite oxide, followed by being exfoliated into individual GO sheets with oxygen-containing functional groups like OH or COOH groups.[162] As the non-conductive nature, GO sheets need to be transformed into conducting rGO by a chemical reduction process or a thermal reduction process.[164,165] Graphene has been employed to hybrid with V_2O_5 nanostructures via various strategies to improve the electrochemical performance for LIBs.[110,148,161,166-168]

V_2O_5 nanowires were homogeneously integrated with graphene sheets to form a robust V_2O_5 nanowire-graphene composite paper via a simple vacuum filtration process.[161] Individual preparations were conducted for graphene oxides by a modified Hummer's method[169] and V_2O_5 nanowires by a hydrothermal treatment process. The uniform mixture of graphene and V_2O_5 nanowires were filtered to obtain a V_2O_5 nanowire–GO composite paper. A following thermal treatment at 350 °C with Ar/H_2 led to the formation of V_2O_5 nanowire-graphene composite paper, which was used as a freestanding electrode for LIBs. The V_2O_5 nanowires have then thickness of ∼10 nm and long lengths of ~ 100 μm, which was evenly dispersed within regularly stacked GO nanosheets (Figure 2.22). This composite electrode exhibited extremely high cycling stability and high-rate performance. When measured at a current density of 10000 mA g^{-1}, the V_2O_5 nanowire-graphene composite cycled up to 100000 cycles with a stable specific capacity of 94.4 mAh g^{-1} (Figure 2.22c). The extremely long cycle numbers are two or three orders of magnitude larger than those of conventional electrode materials, suggesting that highly organized nanostructured electrodes can address the poor cycling issues. The homogeneous distribution of graphene and V_2O_5 nanowires provided excellent charge transfer and robust composite structure, responsible for the outstanding cycling and rate performances. Moreover, the small nanosize of thin V_2O_5 nanowires and abundant voids within the composite paper ensured the fast lithium diffusion and high utilization of electro-active sites.

Rui *et al.* reported the rGO-supported porous V_2O_5 spheres (V_2O_5/rGO) as a high-power cathode material for LIBs.[166] Initially, the nanoparticles of vanadium oxide with diameters of 10–50 nm were grown on the surfaces of rGO sheets in a facile solvothermal process (Figure 2.23a). The precursor nanoparticles were oxidized to obtain the V_2O_5/rGO composites by annealing in air at 350 °C, where the V_2O_5 spheres were evenly anchored on the rGO sheets. The V_2O_5 spheres had a hollow porous structure with diameters of 200–800 nm and pore sizes of ~ 50 nm (Figure 2.23b). The formation of the large V_2O_5 spheres was generated by the self-assembly of vanadium oxide nanoparticles during annealing to reduce their total surface energy. The V_2O_5/rGO composites showed superior battery performance with high specific capacities, small capacity fading, and excellent rate capability. The composite of V_2O_5 with 46 wt% rGO achieved good capacity retention of 85% for 50 cycles at around 0.3C in a voltage window of 2-4 V. As for high-rate performance, this samples preserved the specific capacities of 128 and 102 mAh g−1 at current rates of 13 C and 19 C. The excellent battery performance was contributed from

the novel structures of the V_2O_5/rGO composites, due to high electric conductivity, fast lithium diffusion, easy electrolyte penetration, and good structural stability.

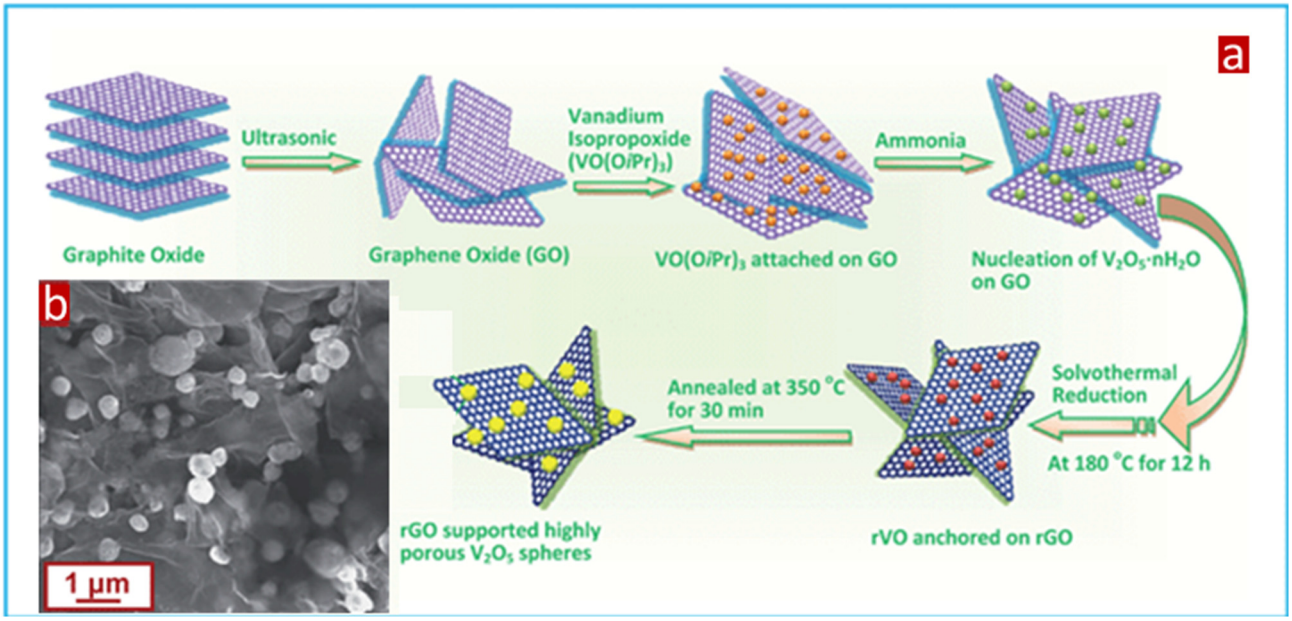

Figure 2.23 (a) The schematic illustration of the preparation of the rGO-supported porous V_2O_5 spheres (V_2O_5/rGO). First, graphite oxide was well exfoliated to form graphene oxide by a modified Hummers method and adequate ultrasonication. Vanadium isopropoxide ($VO(OiPr)_3$ was then easily attached on the GO surfaces, and nucleated into $V_2O_5{\cdot}nH_2O$ with ammonia. A solvothermal treatment was used to produce the composites of rGO and reduced vanadium oxide particles, which were oxidized into the V_2O_5/rGO composite by annealing. (b) SEM image of the composite of V_2O_5 with 46 wt% rGO.[166]

A hierarchical nanocomposite of V_2O_5 nanosheets self-assembled on rGO sheets was prepared by a solvothermal method.[110] The interconnected V_2O_5 nanosheets stood on the surfaces of rGO sheets (Figure 2.24). This hierarchical structure not only provided high porosity and surface area, but also largely prevented aggregation. In a typical synthesis, vanadium oxytriisopropoxide ($VO(OiPr)_3$) and GO were dispersed into ethyl alcohol with ultrasonication to form a uniform precursor solution. The functional groups on the GO surfaces can work as nucleation centers, where $V_2O_5{\cdot}nH_2O$ nanosheets started to grow when the precursor solution reached a critical concentration. This step produced a hierarchical nanocomposite of $V_2O_5{\cdot}nH_2O$ nanosheets and rGO sheets, which was further dehydrated to form the V_2O_5 nanosheets/rGO hierarchical composite by annealing at 300 °C in air. When applied as cathode materials for LIBs, the V_2O_5 nanosheets/rGO

nanocomposite showed excellent cycling stability and rate capability. The composite can be cycled at a high current density of 15 A g−1 (50C) and preserved a capacity of 76 mAh g^{-1}. The slow capacity fading was indicated by a capacity loss of 48% after 160 cycles at 2C. Except the individual advantages of V_2O_5 nanosheets and rGO sheets, the hierarchical structure is another significant factor for the excellent battery performance of the V_2O_5 nanosheets/rGO nanocomposite.

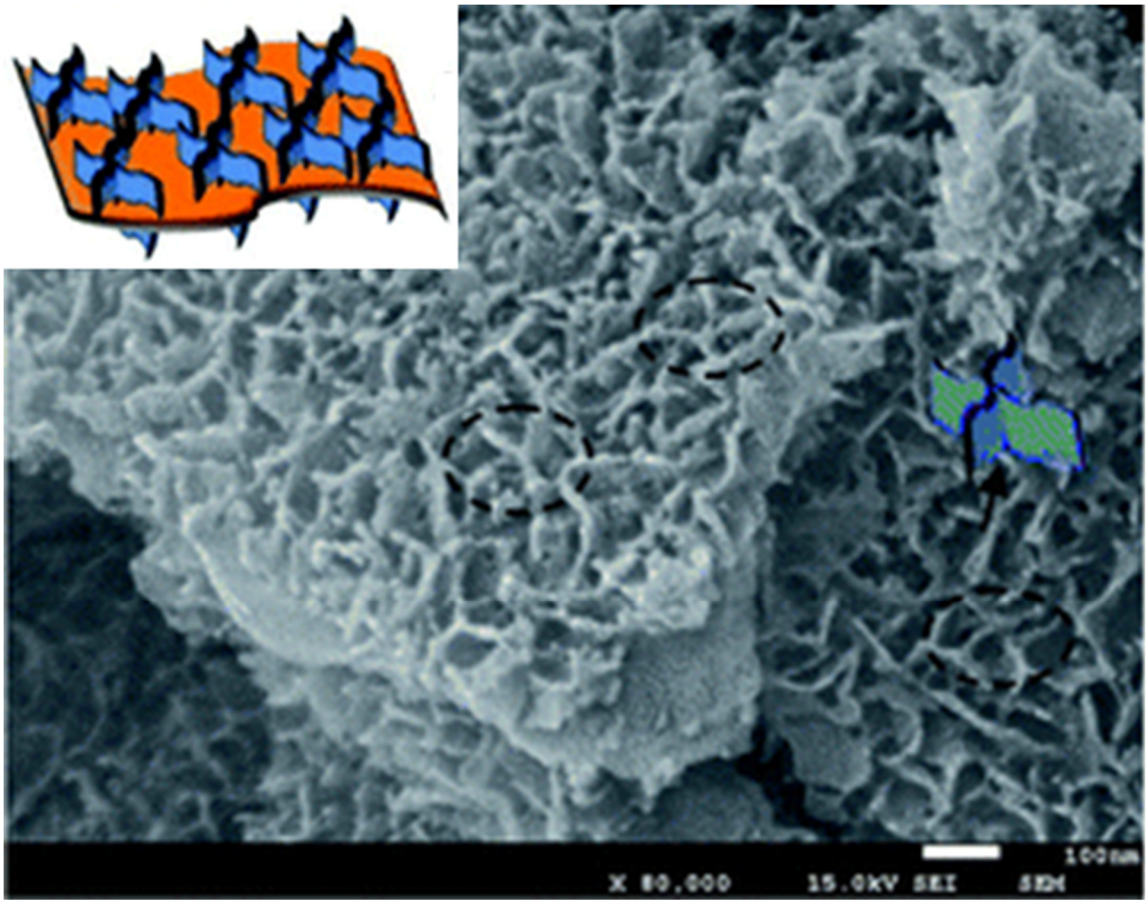

Figure 2.24 SEM images of the V_2O_5 nanosheets/RGO hierarchical composite. The inset is a schematic diagram of the hierarchical structure, where self-assembled V_2O_5 nanosheets were uniformly attached on the rGO sheets.[110]

2.2.4 **Cation-doped V_2O_5**

Different from carbonaceous materials that only enhance the surface electric conductivity of active materials, element doping enables the increase of inherent electric conductivities of active materials. As the low electric conductivity of V_2O_5 highly limits its electrochemical performance, a wide variety of metal cations has been doped into V_2O_5 enhance the

intrinsic electric conductivity, including silver,[170] copper,[171] manganese,[172] aluminum,[173] titanium,[174] and so on. The successful doping of silver ions was reported to increase the electric conductivity of V_2O_5 by over two orders of magnitude.[175,176] Metal cations can be situated between the layers of V_2O_5, and interact with the oxygen atoms of VO_5 pyramids, which increase the stability of the V_2O_5 layered structure.[173] Therefore, the doping of transition metals is favorable to enhance the battery performance of V_2O_5–based electrode materials.

The formation of low valence V^{4+} ions within V_2O_5 can induce surface defects such as oxygen vacancies, which can improve the electric conductivity and cycling stability of V_2O_5.[177] Thermal treatments in an ultrahigh vacuum or in reducing/inert gas atmosphere are good approaches to introduce low valence vanadium ions in V_2O_5.[178,179] Song *et al.* reported the V_2O_5 nanoflakes self-doped by V^{4+} ions as a LIB cathode with enhanced rate and cycling performance.[180] The V^{4+} doped V_2O_5 nanoflakes (V–V_2O_5) were synthesized by a facile hydrothermal method followed with a combustion process. During the hydrothermal treatment, the raw solution containing NH_4VO_3 and $C_2H_2O_4$ produced a dark blue precipitate of $NH_4V_4O_{10}$ and VO_2. The dark blue color is an indicator for the existence of low valence vanadium ions. As $NH_4V_4O_{10}$ and VO_2 are easily oxidized to form V_2O_5 above 350 °C in air, the dark blue precipitate was mixed with 2-ethylimidazole to offer a reduction atmosphere of CO and NO during annealing at 400 °C in air. This reduction atmosphere is essential for the formation of the V^{4+} doped V_2O_5 nanoflakes. It was the first time that an high proportion of tetravalent vanadium ions up to 17.4% had been induced in V_2O_5 by a simple method of one-step combustion. The electrical conductivity of the V–V_2O_5 nanoflakes was 2.86×10^{-5} S cm^{-1}, which is over an order of magnitude higher than that of the V_2O_5 nanoflakes without V^{4+} ions (N–V_2O_5). As for the electrochemical properties for LIBs, The V–V_2O_5 nanoflakes exhibited enhanced rate and cycling performance. The capacity retention of V–V_2O_5 nanoflakes was 89% at a current density of 100 mA g^{-1} after 100 cycles, around 1.3 times that of the N–V_2O_5 nanoflakes. At a high current density of up to 4000 mA g^{-1}, the V–V_2O_5 nanoflakes retained a specific capacity of 139 mAh g^{-1}, while the N–V_2O_5 nanoflakes only showed a much smaller capacity of 77 mAh g^{-1}. The lithium diffusion coefficient of V–V_2O_5 nanoflakes was calculated to be 2 orders of magnitude higher than that of the N–V_2O_5 nanoflakes. The excellent battery performance of the V–V_2O_5 nanoflakes can be ascribed to both the nanostructure and the mixed valence of vanadium ions. The nanoflake structure leads to a high surface area, fast lithium transport, and easy electrolyte penetration. The coexistence of V^{4+} and V^{5+} ions not

only enhances the intrinsic electric conductivity and lithium diffusion coefficient, but also decreases the Ohmic polarization. The oxygen vacancies associated with V^{4+} ions can reduce strains of volume changes and improve structural stability during cycling.

Silver vanadium oxide $Ag_2V_4O_{11}$ has been known as a high-capacity cathode material for primary LIBs to power implantable biomedical devices.[181] The lithium storage of $Ag_2V_4O_{11}$ is based on the combination displacement/intercalation (CDI) mechanism, which enables lithium ions to intercalate into both the vacant sites and the other sites occupied by silver ions.[182] During discharge, Ag^+ ions are reduced to form Ag metals on the surfaces of the active material, while lithium ions are inserted into the oxide lattice.[183] During charge, silver ions return into the oxide lattice with the deintercalation of lithium ions. However, the displacements of Ag^+ ions by lithium ions lead to the collapse of the $Ag_2V_4O_{11}$ structure, due to the large ionic radii mismatch between Ag^+ and Li^+ ions ($r_{(Ag+)}$ = 1.15 Å and $r_{(Li+)}$ = 0.76 Å).[184] The structural irreversibility of $Ag_2V_4O_{11}$ prevents its use in rechargeable LIBs. Hu *et al.* introduced that the nonstoichiometric single-crystalline β-$Ag_{0.33}V_2O_5$ (β-SVO) nanowires synthesized by a one-pot hydrothermal method exhibited structural reversibility during CDI process, which worked as a high-capacity cathode material for LIBs.[170] The whole synthesis did not use any template or surfactant. The reducing agent of acetophenone played a crucial role in the formation of β-SVO nanowires that contain the mixed V^{5+}, V^{4+} and V^{3+} ions. As a cathode material for LIBs, the β-$Ag_{0.33}V_2O_5$ nanowires achieved a reversible intercalation of 1.95 Li^+ ions per formula. The crystal structure of the β-SVO nanowires was still well retrieved after eight cycles. Therefore, the design of nonstoichiometric $Ag_{0.33}V_2O_5$ nanowires is an effective strategy to enhance the structural stability and battery performance of electrode materials based on the CDI mechanism.

Li *et al.* investigated the effects of Sn doping on the material and electrochemical properties of the homogeneous Sn-doped V_2O_5 thin film.[185] A sol-gel method was used to prepare Sn-doped V_2O_5 sol formed by H_2O_2, V_2O_5, and $SnCl_4{\cdot}5H_2O$ as precursors. This sol was cast on the glass substrates of fluorine-doped tin oxide, which was further annealed at 450 °C in air to get the Sn-doped V_2O_5 thin film. The Sn-doped V_2O_5 exhibited an orthorhombic V_2O_5 phase without any impurity. The Sn doping induced the lattice to expand along the *c*- and *b*- axes, indicating the Sn^{4+} ions are possibly located between the layers of V_2O_5, and are bonded with the oxygen atoms of VO_5 pyramids. The insertions of the Sn^{4+} ions are favorable to the structural stability of the Sn-doped V_2O_5. The pure V_2O_5 thin film was consisted of nanobelts, while the Sn-doped V_2O_5 thin film was composed of

small nanoparticles. The Sn^{4+} ions might change the surface energy of the sol, and serve as nucleation centers for the growth of nanoparticles. In addition, the higher concentration of V^{4+} ions was induced by Sn doping within the Sn-doped V_2O_5, than that of pure V_2O_5 thin film. The Sn doping also led to the smaller charge-transfer resistance and larger lithium diffusion coefficient of the Sn-doped V_2O_5 thin film. These contributions from Sn doping enabled the Sn-doped V_2O_5 film to be a good cathode material for LIBs with much better cycling performance. The Sn-doped V_2O_5 film exhibited a capacity of 334 mAh g^{-1} at a current density of 500 mA g^{-1} after 50 cycles, over two times the capacity of 157 mAh g^{-1} for the pure V_2O_5 film.

2.2.5 **Polymer-coated V_2O_5**

Conducting polymers have high conductivities by showing excellent capability of conducting electrons and ions. The high conductivities are highly associated with the oxidation (charged) state of conducting polymers, which is resulted from chemical oxidation of corresponding monomers.[186] Some other advantages of conducting polymers are also favorable for their applications in energy storage, including good chemical stability, high coulombic efficiency, and excellent electrochemical reversibility.[187] Therefore, designing hybrid composites of V_2O_5 with conducting polymers can realize great improvements in the battery performance of V_2O_5 for LIBs. There are three conducting polymers widely used in developing V_2O_5–based cathode materials, such as polypyrrole (PPy),[188-191] polyaniline (PANI),[192-194] and polythiophene,[195-198] The easy synthesis and the commercial availability of both polymers and monomers are the driving forces for the extensive research on these conducting polymers.

The polymer coating on the surface of V_2O_5 is a common method to improve the poor electric conductivity and cycling stability of V_2O_5. Conducting polymers not only enhance the electric conductivity on the V_2O_5 surfaces, but also isolate V_2O_5 from dissolution into the electrolyte.[199] As a result, polymer coated V_2O_5 composites can possess much better cycling and rate performances. Gittleson *et al.* incorporated polyaniline coating with V_2O_5 nanowires to form V_2O_5/PANI core/shell composites as cathode materials for LIBs.[192] The V_2O_5 nanowires were obtained by a hydrothermal method, which was further coated with PANI by in situ polymerization of aniline. The contents of PANIs ranged from 21 wt% to 51 wt% by adjusting polymerization conditions. The initial capacities of the V_2O_5/PANI

composites ascended with the increasing content of PANI. The V_2O_5 with 51 wt% PANI had the 1st discharge capacity of 350 mAh g^{-1}, close to two times that of the pure V_2O_5 nanowires. At a high rate of 440 mA g^{-1} (1 C), the 51% PANI composite still preserved a capacity with 57% higher than that of the pure V_2O_5. In general, PANI coating realized the enhancements in the capacity, cycling stability, and rate capability of the V_2O_5/PANI composites. Zhao *et al.* reported V_2O_5@polypyrrole hybrid material with enhanced lithium storage capability and cycling stability.[188] The micro–nanosized V_2O_5 coated with PPy was prepared by a hydrothermal treatment process followed by in-situ polymerization. The initial capacity of the V_2O_5@PPy composite was lower that of V_2O_5 without PPy, as a result of small contribution of PPy to the capacity of the whole electrode. But the hybrid material exhibited much slower capacity fading with cycling. The V_2O_5@PPy composite retained a discharge capacity of 170 mAh g^{-1} after 100 cycles, while the pure V_2O_5 only possessed a corresponding capacity of 130 mAh g^{-1}. The improved cycling performance of the V_2O_5@PPy composite was attributed to the surface protection and fast electron transport of PPy coating.

Conducting polymers can serve as conductive binder to guarantee good mechanical integrity and electric conductivity of carbon-free electrodes.[200] The use of a conductive binder excludes insulating binders (such as PVDF) and conductive agents (like carbon black) from the electrode, which can reduce the negative effects of these additives on the electrode battery performance. An *et al.* employed the poly(3-hexylthiophene)-block-poly(ethylene oxide) copolymer (P3HT-b-PEO) as the conductive binder for a V_2O_5 composite cathode with improved electrochemical performance.[201] The P3HT-b-PEO copolymer is both electron- and ion- conducting, where P3HT and PEO blocks are connected with covalent bonds. The electrodes were obtained by casting the aqueous mixture of V_2O_5 xerogel and P3HT-b-PEO directly onto stainless steel coins. The V_2O_5 xerogel was consisted of loosely stacked V_2O_5 sheets. The V_2O_5 xerogel with 10 wt% of P3HT-b-PEO (denoted as P10) exhibited tightly packed V_2O_5 sheets with uniform surface, indicating even distribution of the conductive P3HT-b-PEO binder between adjacent V_2O_5 sheets. P10 had no capacity fading with a stable capacity of 180 mAh g^{-1} at 0.1C up to 250 cycles. The V_2O_5 xerogel only kept a capacity of 77 mAh g^{-1} till 30 h, after which the electrode cannot be fully discharged. Compared with the appearance of large cracks on the V_2O_5 xerogel after cycling, P10 didn't show obvious cracking on the surface, confirming the excellent mechanical integrity. The higher electric and ionic conductivities of P10 were

also revealed from the electrochemical impedance spectrum. Therefore, the carbon-free V_2O_5 composite electrode with P3HT-b-PEO is a high-performance electrode for LIBs.

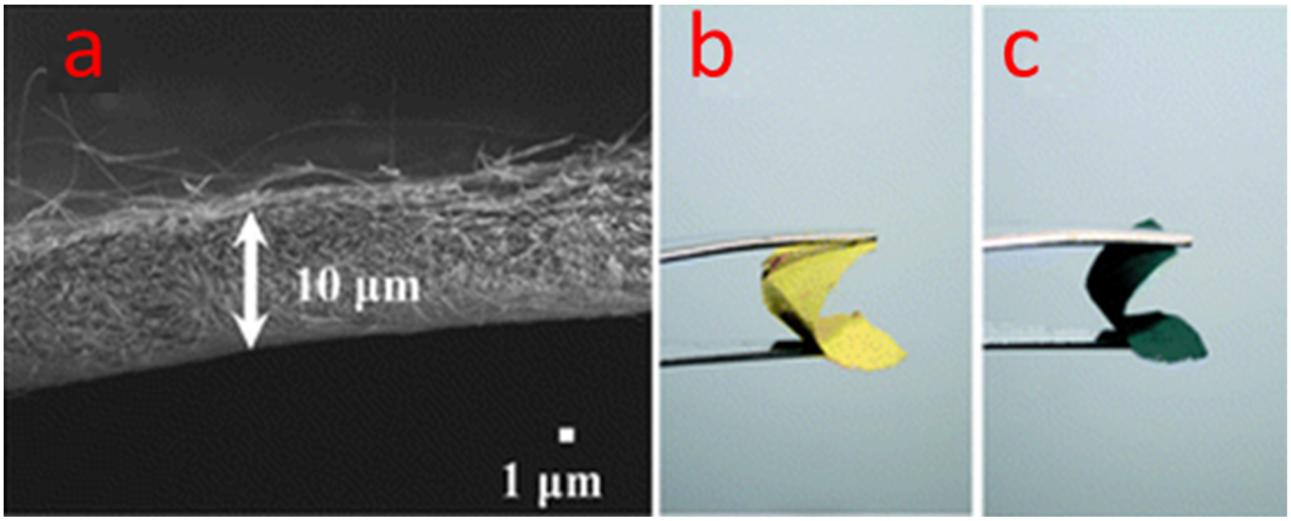

Figure 2.25 FESEM image (a) of the cross-section of the free-standing V_2O_5–polypyrrole thin film with a thickness of 10 µm; Photographs of the pure V_2O_5 film (b) and the V_2O_5–polypyrrole film (c) with good flexibility under bending conditions.[189]

Some V_2O_5 composites with conducting polymers can be directly used as freestanding electrodes for bendable or wearable LIBs. The conducting polymers within freestanding electrodes not only offer the good electric conductivities, but also function as binders to enhance the electrodes' mechanical strength. Freestanding electrodes don't need substrates and conductive agents, due to their adequate electric conductivities and high mechanical durability. Noerochim *et al.* presented a flexible paper-like V_2O_5–polypyrrole film electrode as a freestanding cathode for LIBs.[189] The thin film was composed of highly interconnected nanowires with uniform PPy coating. A modified vacuum filtration technique was used to obtain a soft and robust thin film with a thickness of about 10 µm (Figure 2.25). The V_2O_5–PPy film exhibited a superior cycling performance with a capacity of 187 mAh g^{-1} at a current density of 40 mA g^{-1} after 100 cycles, far beyond the 33 mAh g^{-1} of pristine V_2O_5 film in the same conditions. There were no cracks observed in the electrode after the repetitive bending tests. The battery performance of the V_2O_5–PPy film was only slightly affected by mechanical bending. The great battery performance and durability of the V_2O_5–PPy film were attributed to the synergistic contributions from the inorganic V_2O_5 nanowires and the organic PPy coating.

Table 2.1 The electrochemical performance of the V_2O_5-based hybrid materials for LIBs.

Strategies	Material	Voltage range [V]	Capacity [mAh g^{-1}]	Current density [mA g^{-1}]	Cycles	Rate capability		Ref.
						[mAh g^{-1}]	[A g^{-1}]	
Carbon coating	Carbon-coated V_2O_5 nanocrystals	2.0−4.0	288	1000	50	130	10	[36]
	Carbon-coated V_2O_5 nanoparticles	2.0−4.0	270	15	50	–	–	[153]
	V_2O_5/mesoporous carbon composite	2.0−4.0	163	500	100	70	5	[202]
CNT composition	V_2O_5 nanoparticles/ carbon tube-in-tube	2.0−4.0	265	59	20	90	5.88	[149]
	V_2O_5 nanowire/MWCNT	1.8−4.0	260	70	50	169	2.80	[147]
	CNTs encapsulating V_2O_5 nanosheets	2.0−4.0	211	150	200	90	30	[160]
	V_2O_5 nanosheets assembled on CNTs	2.0−4.0	190	294	100	116	8.82	[203]
	V_2O_5 nanosphere/MWCNT layer-by-layer composite	2.0−4.0	200	294	100	130	1.18	[204]
Graphene composition	rGO-supported porous V_2O_5 spheres	2.0−4.0	202	90	50	102	5.70	[166]
	V_2O_5 nanowires/ graphene	1.7−3.8	192	1000	3000	256	10	[161]
	V2O5 nanosheets self-assembled on rGO	2.0−4.0	102	600	160	76	15	[110]
	3D V_2O_5/rGO/CNT composite	2.0−4.0	220	294	80	100	5.88	[148]
	V_2O_5 nanoparticles embedded in rGO balls	2.0−4.0	214	1000	100	200	1.50	[168]
	V_2O_5/rGO xerogel	1.5−3.7	252	443	150	201	4.43	[167]
Metal doping	Self-doped V^{4+}−V_2O_5 nanoflakes	2.0−4.0	260	100	100	139	4	[180]
	Al-doped V_2O_5/rGO nanocomposite	2.0−4.0	247	300	50	122	3	[173]
	ZrO_2-doped V_2O_5 particles	1.5−4.0	222	294	50	–	–	[205]
	Mn-doped V_2O_5 flakes	2.0−4.0	201	300	50	171	1.50	[206]
	Sn-doped V_2O_5 microspheres	2.0−4.0	212	200	50	163	2	[207]
Polymer coating	PEDOT/ V_2O_5 nanobelt / graphite foam	2.0−4.0	265	1500	500	115	24	[195]
	PANI-coated V_2O_5 nanowires	1.5−4.0	95	44	50	125	0.44	[192]
	PPy-coated V_2O_5 nanowires	1.5−4.0	188	40	100	–	–	[189]
	PPy-coated V_2O_5 rods	2.0−4.0	170	7	100	–	–	[188]

Modifying V_2O_5 nanostructures with carbon materials, metal doping, or polymer coating is the major direction to produce high-performance V_2O_5 cathode materials. Table 2.1 compared the electrochemical performance of the representative V_2O_5–based cathode materials along this direction. Combining multiple strategies together to modify V_2O_5 nanostructures could be significant for future breakthrough. It is highly expected to generate synergy effects on enhancing battery performance of V_2O_5 nanomaterials.

2.3 Summary

Traditional cathode materials only exhibit low specific capacities, which highly restrict the battery performance of LIBs. $LiCoO_2$, $LiMn_2O_4$, $LiFePO_4$, and their derivatives are not able to reach specific capacities over 200 mAh g^{-1} yet. Developing superior cathode materials with high energy density is of great urgency. V_2O_5 is considered as the best candidate for cathode materials to achieve high energy density, since V_2O_5 allows more than two lithium ions to intercalate into its layered structure. The less mass of V_2O_5 is required to obtain the same specific capacity, in comparison with other cathode materials. However, the applications of the V_2O_5 cathode material are challenged by its low electric and ionic conductivity, irreversible phase transitions for cycling, and dissolution into the electrolyte.

Great research attention has been paid to improve the electrochemical performance of the V_2O_5 by nanostructures, carbonaceous materials, metal doping, and conductive polymers. The nanostructured V_2O_5 materials possess high surface area and nano-scale particle sizes, which generate high amount of active sites and short diffusion paths for lithium ions. The 3D hierarchical V_2O_5 nanostructures were further developed to produce high tap densities and robust morphologies, beyond the abilities of common nanostructures. In addition, the V_2O_5 nanomaterials still have the problem of low electric conductivity. The carbon materials and conductive polymers have been widely integrated with the V_2O_5 nanomaterials to build excellent conductive networks. The metal-doped V_2O_5 nanomaterials can exhibit great electrochemical performance by enhancing intrinsic electric conductivities.

In order to further enhance the battery performance of the V_2O_5–based cathode materials, crucial strategies are needed to raise the ionic conductivity and to eliminate irreversible phase transitions. However, there were only few reports related to these two aspects. It is highly desired to increase the fundamental understanding on the slow ionic conductivity

and the irreversible phase transitions of V_2O_5. Moreover, novel designs of combining multiple approaches are essential in achieving V_2O_5 cathode materials with high energy and power densities.

3 Experiment methods

This chapter introduces technical processes and principles related to sample preparation and property measurements. Electrode materials prepared by different synthesis methods were investigated by systematic material characterizations. Following electrode preparation, battery assembly was carried out in a glove box. Multiple electrochemical measurements were conducted to evaluate battery performance of coin cells.

3.1 Chemical reagents and materials

Table 3.1 The information of the chemical reagents used in this thesis.

Reagent	**Formula**	**Purity**	**Supplier**
1-Methyl-2-pyrrolidinone (NMP)	C_5H_9NO	99.5%	Sigma-Aldrich
3,4-ethylenedioxythiophene (EDOT)	$C_6H_6O_2S$	97%	Sigma-Aldrich
Acetonitrile	CH_3CN	99.80%	Sigma-Aldrich
Aluminium foil	Al	N/A	TMI
carbon black	C	Super P	Timcal
Copper(II) nitrate trihydrate	$Cu(NO_3)_2{\cdot}_3H_2O$	> 99%	Sigma-Aldrich
CR2032 Coin cells	N/A	N/A	Biyuan, China
Diethyl carbonate (DEC)	$C_5H_{10}O_3$	≥ 99 %	Sigma-Aldrich
Ethanol	C_2H_5OH	≥ 99.5 %	Merck
Ethylene carbonate (EC)	$C_3H_4O_3$	99%	Sigma-Aldrich
Hydrogen peroxide	H_2O_2	30%	Chem-Supply
Iron (III) chloride	$FeCl_3$	97%	Sigma-Aldrich
Lithium hexafluorophosphate	$LiPF_6$	98%	Sigma-Aldrich
Lithium metal	Li	N/A	Biyuan, China
LP30 electrolyte	$LiPF_6$ in EC/DEC (1:1)	N/A	Biyuan, China

Melli-Q water	H_2O	5 ppb (TOC)	Millipore
Multi-walled carbon nanotube	C	> 99%	Timesnano
pluronic P123	$(C_3H_6O.C_2H_4O)n$	N/A	Sigma-Aldrich
Polyproylene separator	$(C_3H_6)n$	N/A	Biyuan, China
Poly(vinylidene fluoride) (PVDF)	$(CH_2CF_2)n$	N/A	Sigma-Aldrich
Vanadium(V) oxide	V_2O_5	≥99.6%	Sigma-Aldrich

3.2 Occupational Health, Safety and Welfare

The policies for occupational health, safety and welfare (OHS&W) in the University of Queensland were well conducted for working on this research project. Diverse health and safety trainings were completed for this project, including laboratory safety, chemical safety, general workplace safety, and fire safety. All the experiments were performed in a safe manner following safe working procedures. Appropriate personal protective equipment was worn when using chemicals, including lab coat, safety glass, closed-in shoes, nitrile gloves, and mask (P2). All experiments involving toxic or volatile chemicals were carried out in a fume hood.

3.3 Material synthesis

3.3.1 **Hydrothermal method**

The hydrothermal method is an outstanding approach to synthesize nanostructured materials, due to simplicity, low temperature, fast reaction, and pollution free. It also offers good control over the size and shape of nanostructures.[208] The hydrothermal synthesis involves liquid chemical reactions of solids and solvents in a closed system with the conditions of high pressure and high temperature. Hydrothermal treatment generates supercritical conditions, in which precursors produce nano-scale morphologies that can not be realized by classic synthesis approaches. Various parameters need be selected and adjusted for premium hydrothermal conditions, including temperature, duration, PH values, concentration of solvents, autoclave volumes, as well as templates and additives.[209] Teflon lined stainless steel autoclaves are typical reactors for hydrothermal reactions. The autoclaves used in this thesis were purchased from Shenzhen Biyuan Electronics Co. Ltd.,

China. Liquid reactants are thermally treated in the sealed autoclaves under self-generated vapor pressure. After natural cooling down to room temperature, the products are repeatedly washed with distilled water to remove impurities.

In Chapter 6, V_2O_5 nanobelts were synthesized by a facile hydrothermal method with H_2O_2 as the solvent. Nano morphologies were controlled by the temperature and time of hydrothermal treatments. The direct reactions between V_2O_5 and H_2O_2 don't request any addition of organic surfactants or inorganic ions, avoiding the impurities of foreign ions or organic ligands. Moreover, the vanadium concentration can be accurately controlled by H_2O_2 volume. The formation process of $V_2O_5 \cdot nH_2O$ can be described as following: H_2O_2 solution is highly acidic with a low PH value of 1.5. The dissolution of V_2O_5 into H_2O_2 generates an orange solution of unstable diperoxo $[VO(O_2)_2]^-$ species. These anions undergo two-step transformations into monoperoxo $[VO(O_2)]^+$ cations and $[VO_2]^+$ vanadates. A decavanadic acid $[H_2V_{10}O_{28}]^{4-}$ solution is obtained after several hours, which finally changes into hydrated vanadium oxides.[210] The chemical reactions for this complex formation process are demonstrated with Equation 3.1:[211,212]

$$V_2O_5 + 4H_2O_2 \rightarrow 2[VO(O_2)_2(OH_2)]^- + 2H^+ + H_2O \quad (1)$$

$$2[VO(O_2)_2(OH_2)]^- + 4H^+ + 2H_2O \rightarrow 2[VO(O_2)(OH_2)_3]^+ + O_2 \quad (2)$$

$$V_2O_5 + 2H^+ + 2H_2O_2 + 3H_2O \rightarrow 2[VO(O_2)(OH_2)_3]^+ + O_2 \quad (3)$$

$$2[VO(O_2)(OH_2)_3]^+ \rightarrow 2[VO_2]^+ + O_2 + 6H_2O \quad (4)$$

$$10[VO_2]^+ + 8H_2O \leftrightarrow {H_2V_{10}O_{28}}^{4-} + 14H^+ \quad (5)$$

3.3.2 **Reflux**

Reflux is an efficient technique for liquid-phase reactions to minimize the loss of a solvent and to maintain stable temperature. A reflux apparatus includes a hot plate, an oil bath, a flask, a condenser tube, ring stands, and water hoses. Typically, a flask containing liquid reactants is heated in an oil bath. The hot vapor of the solvent goes up into a cold condenser with circulating water. The vapor is condensed back to the solvent in the flask. The loss of the solvent is so minor that no solvent need be compensated for a long time, which is the highlight of reflux. In addition, stable thermal heating accelerates the reaction speed by offering necessary energy. The reaction temperature can be manipulated by choosing appropriate solvents with different boiling points.

3.3.3 **Chemical oxidative polymerization**

Chemical oxidative polymerization is a green polycondensation method with the lowest loading of monomers.[213] The only product after the polymerization is water. The temperature required for polymerization is also moderate. Typically, monomers are assembled into polymer chains under the action of an oxidizing agent. During the oxidation process, monomer molecules possess radical cation sites by abstracting two protons, and are connected by covalent bonds to form polymers.[214] As the oxidizing agent is needed in each stage of polymer growth, the molar ratio of the oxidizing agent and the monomer need to be appropriate. In chapter 5, poly(3,4-ethylenedioxythiophene) (PEDOT) was prepared by corresponding monomers in the presence of the $FeCl_3$ oxidizing agent at appropriate temperature.

3.4 Material Characterization

3.4.1 **X-ray diffraction**

X-ray diffraction (XRD) is a well-known technique to identify the chemical compositions and the crystal structures of materials. X-rays are special electromagnetic waves with the wavelengths of several angstroms (Å), comparable to the interplanar spacing in crystal lattices. Every set of crystallographic planes in materials diffract the x-rays in a specific direction to generate constructive interference. The conditions for constructive interference have to follow the Bragg's law ($n\lambda = 2d\sin\theta$), where n is an integer.[215] This equation defines the relationship of the X-ray wavelength (λ) with lattice spacing (d) and incident angle (θ). As a polycrystalline material have all the crystal faces randomly exposed, the possible angles of diffraction can be detected by scanning the material in a range of incident angles. In the XRD pattern, characteristic diffraction peaks on different 2θ angles correspond to various lattice planes. Every material has a set of unique lattice spacing, which can be directly converted from the diffraction peaks of the XRD pattern. In this thesis, polycrystalline powders were used to collect XRD patterns.

3.4.2 **Scanning electron microscopy**

Scanning electron microscopy (SEM) is a primary technique to investigate the surface morphologies of nanomaterials. SEM employs high-energy electron beams to scan material surfaces. The interactions between a sample and an electron beam produce secondary electrons, backscattered electrons, and x-rays. These signals can reveal information about surface morphology, composition, and chemical elements. Secondary electrons are low-energy electrons emitted from the top 15 nm of the specimen surface. Secondary electrons are collected easily to generate a secondary electron image, which is the best to show topographical information. Secondary electron images can reach a resolution of lower than 10 nm. As for the material with low electric conductivity, a thin layer of metal need be coated on its surface. The low electric conductivity can induce surface charging to block the paths of secondary electrons. In this thesis, the V_2O_5-based materials were coated with a 15 nm layer of platinum prior to SEM imaging.

3.4.3 **Transmission electron microscopy**

Transmission electron microscopy (TEM) is a high-resolution imaging instrument to investigate the internal morphology, crystal orientation, and phase identification of an ultra-thin specimen. An electron beam with high energy is used to interact with an ultra-thin specimen by passing through it. A detector is placed underneath the specimen to collect transmitted electrons for generating a TEM image. A typical TEM can achieve a high resolution of better than 1 nm. TEM images can show the internal morphology and the lattice fringe of a specimen. Selected area electron diffraction (SAED) is also available in TEM to examine the crystallographic experimental of a specimen. The size of selected area only has hundreds of nanometers. With small de Broglie wavelength, electron beams can be diffracted by the crystal lattice of a specimen in particular directions. SAED can identify the phase of a crystalline material, similar to XRD. In a SAED pattern, diffraction spots represent lattice planes, and the distances between spots correspond to interplanar spacing. In this thesis, an accelerating voltage of 100 kV was applied to the TEM (JEOL JEM-1010), while 120 kV was selected for the high-resolution TEM (JEOL JEM-2100).

3.4.4 **Energy dispersive X-Ray spectroscopy**

Energy Dispersive X-Ray (EDX) spectroscopy is used to conduct elemental analysis of a specimen. When high-energy electron beams hit the atoms of a specimen, x-rays are released from the stimulated atoms. Each element possesses a unique atomic structure, so that the x-rays emitted from an element is different from others. EDX can identify the elemental composition of a specimen and quantify the elements. EDX is commonly integrated with SEM and TEM. The EDX in SEM has a resolution of around one micron, while the resolution of EDX reaches few nanometres in TEM.

3.4.5 **Thermal gravimetric analysis**

Thermal gravimetric analysis (TGA) is to investigate the weight loss of a material dependent on the increasing temperature. The weight loss might be related to volatilization, decomposition, and oxidation. The maximum temperature need be kept below the melting point of the material. Appropriate gas atmosphere is required during the thermal heating, such as inert or reactive gas. In this thesis, TGA was used to calculate the content of conductive additives in the V_2O_5 composite materials. The sample loadings were around 5 mg.

3.4.6 **Brunauer-Emmette-Teller surface area analysis**

Brunauer-Emmette-Teller (BET) surface area analysis is a widely used method to calculate the surface area of a porous material. Based on the Langmuir theory, gas molecules are physically absorbed to form a monomolecular layer on the surface of material. The BET theory is extended to multilayer absorption according to Equation 3.2:[216]

$$\frac{1}{v\left[\left(\frac{P_o}{P}\right)-1\right]} = \frac{c-1}{v_m c}\left(\frac{P}{P_o}\right) + \frac{1}{v_m c}$$

Where v is the mass of absorbed gas, P/P_o is relative pressure, v_m is the mass of absorbed monolayer gas, and c is BET constant. The relationship of $1/v[(P_o/P)-1]$ and P/P_o is kept linear in the range of $0.05 < P/P_o < 0.35$. The specific BET surface area (S_{BET}) is calculated as Equation 3.3:

$$S_{BET} = \frac{v_m N s}{aV}$$

Where N is Avofadro's number, s is the absorption cross section, V and a are the molar volume and molar mass of absorbent. In this thesis, samples were degassed at 120 °C overnight to remove residual water before BET measurements. The sample loading was around 150 mg. Liquid nitrogen was used to provide low temperature for BET testing.

3.4.7 **Fourier transform infrared spectroscopy**

Fourier transform infrared spectroscopy (FTIR) is considered as the fingerprint of a material by determining characteristic molecular vibrations that absorb infrared radiation. When infrared ray is transmitted through a molecule, the infrared ray can be absorbed if its frequency matches the vibrational energy levels of a molecule. FTIR reflects the dependence of molecular vibrations on the frequencies of infrared rays. There are no two molecules sharing the same FTIR, as a molecule has unique bond vibrations. Attenuated total reflection-Fourier transform infrared (ATR-FTIR) spectra is a special technique suitable to thick or strongly absorbing specimens. Instead of being transmitted, the infrared ray is reflected on the surface of the material directly contact with an ATR crystal. The infrared ray can only penetrate into the top few microns of the material surface.

3.4.8 **X-ray photoelectron spectroscopy**

X-ray photoelectron spectroscopy (XPS) is a leading technique to investigate the elemental compositions, oxidation states, and electronic states of elements in a specimen. A beam of x-rays is applied to irradiate a specimen, and electrons are then released from the surface of this specimen. The kinetic energy and numbers of electrons are collected to produce x-ray photoelectron spectroscopy. The penetration depth of x-rays is within 10 nm for XPS. The results of XPS can only reflect the elemental information on the surface of material.

3.5 Electrode preparation and cell assembly

In order to have good mechanical stability and electric conductivity, LIB electrodes were prepared with three components, including active materials, binders, and conductive agents. Polyvinylidene fluoride (PVDF) was selected as the binder, which was dissolved in *N*-methyl-2-pyrrolidone (NMP) with a concentration of 50 mg/ml. Carbon black was used

as the conductive agent. The electrode slurry was prepared by mixing an electroactive material, carbon black and polyvinylidene fluoride (PVDF) at appropriate mass ratios. The solid loading for the slurry was adjusted by adding extra NMP. The slurry was cast onto an aluminum foil and dried at 70 °C for 12 h. A manual cutter is used to cut the cathode disks with a diameter of 15 mm. The mass loading of each active material was around 2 mg.

The CR2032 type coin cells are assembled in glovebox (MBraun Company, Germany) under ultra-pure Ar atmosphere, where both moisture and oxygen levels were less than 0.1 ppm. A metallic Li disk is chosen as the counter electrode. The electrolyte solution was made up of 1.0 M $LiPF_6$ in ethylene carbonate (EC) and dimethyl carbonate (DMC) (1:1, w/w). Two pieces of round sheet of polyethylene membrane were placed between the two electrodes as separators. A steel spacer and a steel spring are applied between the anode and the negative cell shell to make sure a close contact of each component. Figure 3.1 shows the schematic diagram of a coin cell assembling. After assembly using a crimping machine (MTI company, China), the coin cells are put aside for 12 hours, and are then loaded for electrochemical testing.

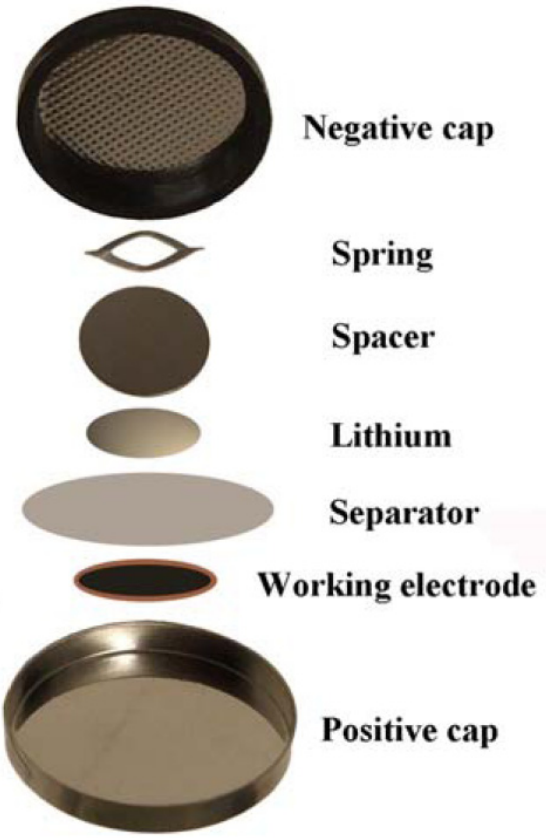

Figure 3.1 Schematic illustration of coin cell assembly.

3.6 Electrochemical measurements

Electrochemical measurements were conducted to evaluate the battery performance of coin cells, including galvano-static charge/discharge, cyclic voltammetry, and electrochemical impedance spectroscopy.

3.6.1 **Galvano-static charge/discharge**

The cycling performance of electrode materials is investigated by galvanostatic charge/discharge at a constant current density. The discharge capacity (Q) equals the total electrons during the time of full discharge, which can be calculated from the current and the time $Q = I \times t$. In comparison, the rate capabilities of electrode materials were examined by galvanostatic charge/discharge at a series of different current densities. In this thesis, coin cells were charged and discharged by using a Battery Testing System (Neware, China).

3.6.2 **Cyclic voltammetry**

Cyclic voltammetry (CV) is employed to study the behavior of electrochemical reactions when the potential sweeps within a selected voltage window. The operating potential changes linearly at a constant speed, and current densities are collected as a function of the potential. Distinctive current peaks appear at the potentials where redox reactions take place. In this thesis, CV measurements were performed on a CHI 660b electrochemical workstation.

3.6.3 **Electrochemical impedance spectroscopy**

Electrochemical impedance spectroscopy (EIS) is a powerful tool to evaluate the electric and ionic conductivities of electrode materials. Small AC potentials with a wide range of frequencies are applied to the open-circuit DC voltage. EIS can be expressed by the dependence of the imaginary part (Z”) on the real part (Z’). In a typical EIS spectrum, the semicircle at high frequencies is related to the kinetics of charge transfer, while the tail at low frequencies corresponds to the Li^+ diffusion within active materials.[217]

4 The effects of electrode composition and voltage window on the electrochemical properties of V_2O_5

4.1 Introduction

Conventional LIB electrodes consist of three components, including active material, binder, and electric conductive agent (e.g. carbon black). Conductive agents enhance the electric conductivities of electrodes, while the insulating binders adhere different electrode components together. Polymeric binders and conductive agents are inactive materials, which reduce the gravimetric energy density of LIBs. In an electrode, the contribution of each component is restrained by the other two.[218,219] More binders and active materials can decrease the electric conductivity of the electrode. More conductive agents can reduce the firm contacts between active materials and also cause side reactions with the electrolyte.[119,220] The electrochemical performance of an electrode is closely associated with the ratios of its three components.[221-223] Zheng *et al.* investigated the dependence of the electrochemical properties of the $LiNi_{0.8}Co_{0.15}Al_{0.05}O_2$ cathode on the electrode compositions.[221] The rate performance of the electrode is greatly affected by the polyvinylidene difluoride (PVDF)-to-acetylene black (AB) ratio. The rate capability of the electrode is independent of the active material content at a PVDF/AB ratio of 5:3. The increase in the active material content can enhance the rate performance above this ratio, or decrease the rate performance below this ratio.

V_2O_5 is a promising cathode material with high energy density for LIBs.[109,132,139,141,224] As a typical intercalation compound, V_2O_5 can exhibit a theoretical specific capacity of 440 mA h g^{-1}.[104-106] This capacity corresponds to the irreversible phase of ω-$Li_3V_2O_5$, allowing 3 Li^+ insertions per formula unit. However, the ω-$Li_3V_2O_5$ leads to large first capacity loss, and greatly depresses the cycling stability of V_2O_5.[99] The lithium insertion/extraction in V_2O_5 can be controlled by the voltage windows for discharge/charge.[99] Therefore,

adjusting the voltage windows is effective to improve the battery performance of the V_2O_5 by excluding the formation of the ω-$Li_3V_2O_5$ phase. The effects of the voltage windows on the battery performance of the V_2O_5 are important to understand the electrochemical mechanism.

The electrochemical performance of V_2O_5 is also restricted by its low electric conductivity and slow ionic diffusion coefficient.[42,43] Conductive agents and polymeric binders are necessary for the V_2O_5 electrodes to have good mechanical stability and electric conductivity. When too much inactive additives are used, the V_2O_5 electrode suffers from serious negative effects. The V_2O_5 electrode might not have sufficient electric conductivity, if the amount of inactive additives is inadequate. The electrochemical properties of the V_2O_5 electrode are closely related to the electrode compositions.

In this chapter, the effects of electrode composition and voltage window on the electrochemical properties of V_2O_5 were systematically investigated. The electrode compositions were adjusted by varying the ratios of carbon black (CB) and PVDF. Two electrodes were prepared with the different V_2O_5:CB:PVDF ratios of 7:2:1 and 8:1:1. In the voltage window of 1.5-4 V, the electrode with 20% of carbon black and 10% of PVDF exhibited better cycling and rate performance, due to adequate electric conductivities. The electrochemical properties of this electrode were further studied by changing the voltage windows of charge/discharge. The narrow voltage window of 2-4 V can eliminate the formation of irreversible ω-$Li_3V_2O_5$ phase and restrict V_2O_5 to have a maximum two lithium intercalation. The electrochemical reversibility and cycling performance of the electrode were greatly improved in the narrower potential range of 2-4 V.

4.2 Experimental

Commercial V_2O_5 powder, poly-vinylidene fluoride (PVDF), and *N*-methyl-2-pyrrolidone (NMP) were purchased from Sigma-Aldrich. The carbon black (Super P) was purchased from Timcal. The electrode was fabricated by mixing the commercial V_2O_5 powder, carbon black and PVDF at weight ratios of 70 : 20 : 10 and 80 : 10 : 10 in appropriate amount of the NMP solvent. The resulting slurry was pasted onto an aluminum foil and dried at 70 °C for 12 h. After that, the foil was punched into small disks with a diameter of 14 mm. The mass loading of the electrode material was around 1 mg. Metal lithium disks were used as anodes and the electrolyte solution was made up of 1.0 M $LiPF_6$ in ethylene carbonate

(EC) and dimethyl carbonate (DMC) (1 : 1, w/w). The CR2025 coin-type cells were assembled in an argon-filled glove box, where both moisture and oxygen levels were less than 0.1 ppm.

X-ray diffraction (XRD) data was collected by a Shimadzu diffractometer (XRD–6000, Tokyo, Japan) with Cu Kα radiation. The material morphology was imaged with a JEOL SU3500 scanning electron microscopy (SEM). The specific surface areas of the samples were measured by the Brunauer-Emmette-Teller (BET) method to investigate porosity.
The electrochemical properties of commercial V_2O_5 powder were investigated over different voltage ranges of 2.0–4.0 V and 1.5-4.0 V. The cells were charged and discharged at different current rates by using a Battery Testing System (Neware, China). Cyclic voltammetry (CV) and Electrochemical impedance spectroscopy (EIS) were performed on a CHI 660b electrochemical workstation. CV was carried out at a scanning rate of 0.1 mV s^{-1}.

4.3 Results and discussions

4.3.1 Material properties

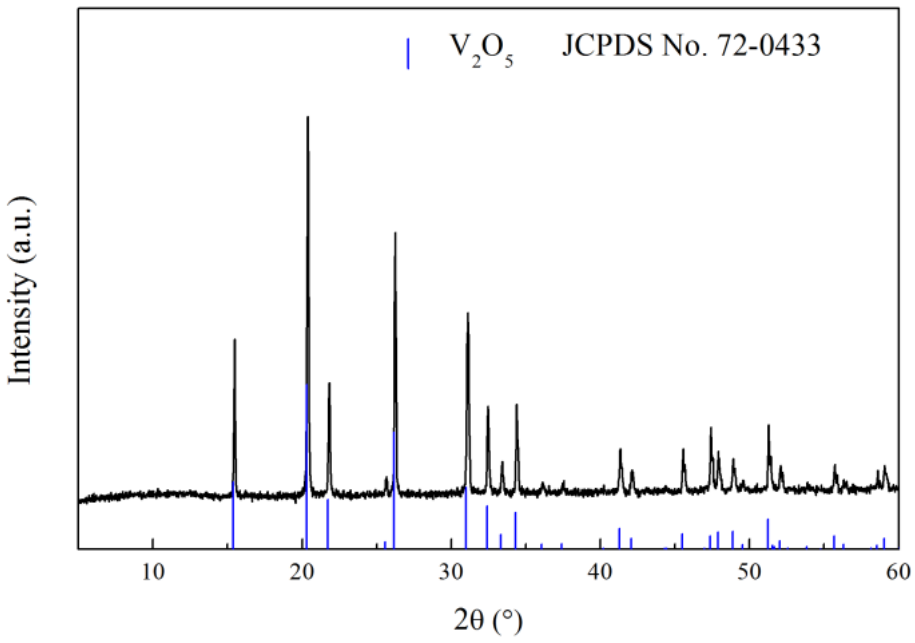

Figure 4.1 XRD pattern of commercial V_2O_5 powder.

The phase purity and crystallinity of commercial V_2O_5 powder were investigated by XRD (Figure 4.1). All the diffraction peaks can be indexed to the orthorhombic V_2O_5 phase (JCPDS card no. 72-0433, space group: *Pmnm (59), a = 11.51 Å, b = 4.369 Å, c= 3.563 Å*). No other phase is detected, which indicates the high purity of the commercial V_2O_5 powder. The morphology of commercial V_2O_5 powder was further examined by SEM (Figure 4.2). V_2O_5 is high-density agglomerates of tablet-shape particles. The tablet-shape particles are about 1-2 μm in length, 0.5-1 μm in width, and 200-600 nm in thickness. In terms of N_2 adsorption and desorption isotherm (Figure 4.3), the BET surface area of V_2O_5 were 4.2 m^2/g.

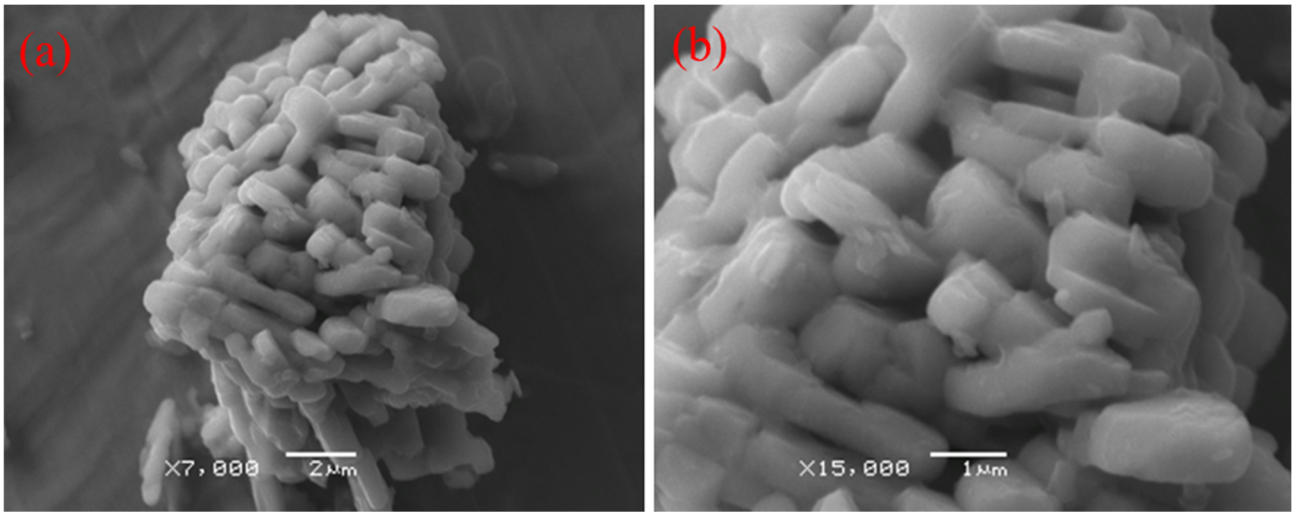

Figure 4.2 SEM images of commercial V_2O_5 powders at different magnifications.

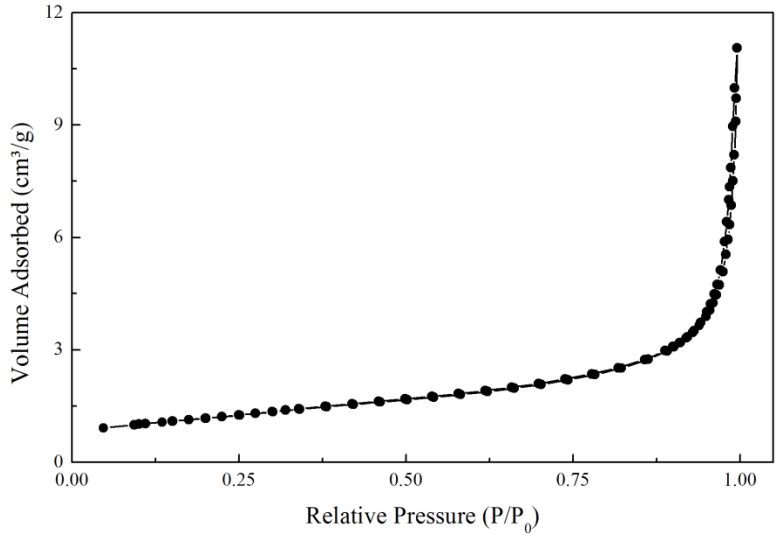

Figure 4.3 Nitrogen adsorption-desorption isotherms of commercial V_2O_5 powder.

4.3.2 **Effects of electrode composition**

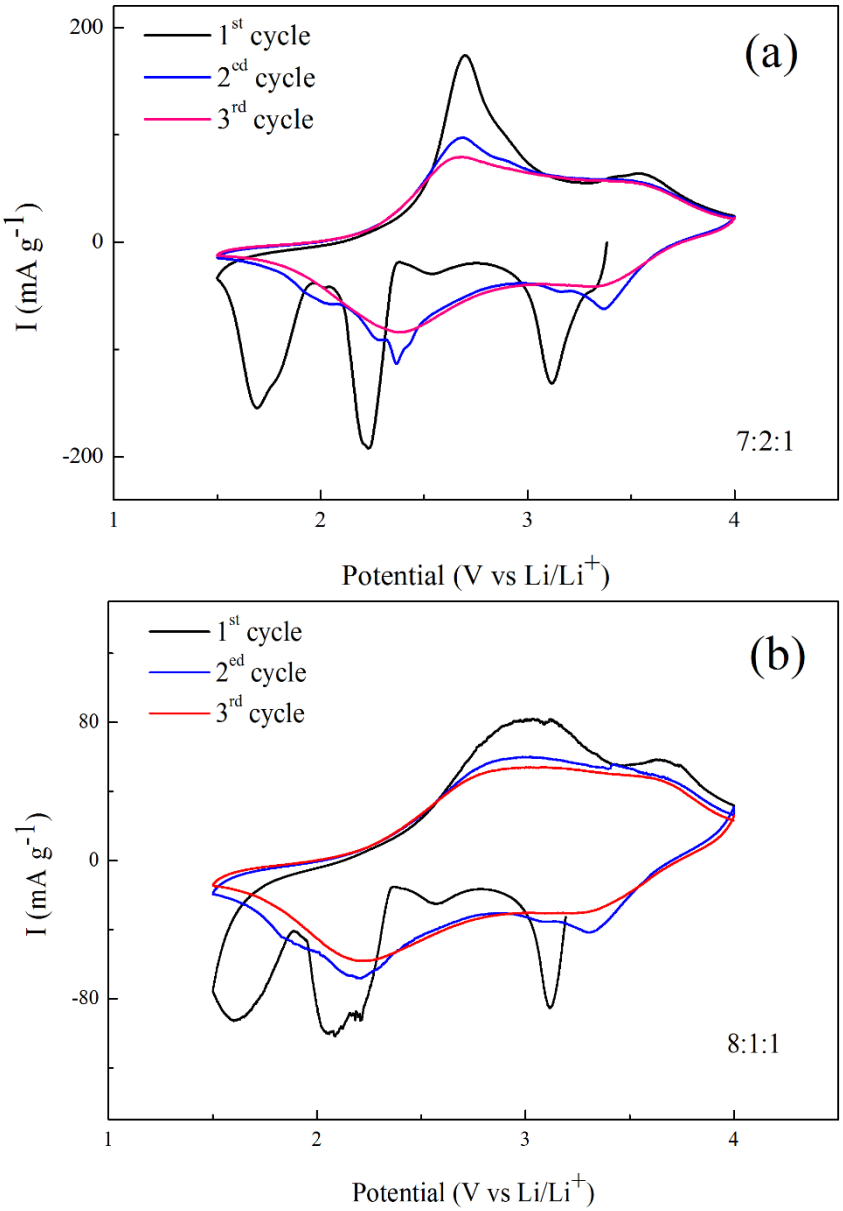

Figure 4.4 Cyclic voltammograms (first three cycles) of the V_2O_5 electrodes with different compositions a) 7V:2C:1P and b) 8V:1C:1P in the voltage range of 1.5-4.0 V.

To investigate the effects of electrode composition on battery performance, two V_2O_5 electrodes with different compositions were prepared. The weight ratios of V_2O_5 powder, carbon black, PVDF were 70 : 20 : 10 and 80 : 10 : 10, respectively. Figure 4.4 shows the CV curves of the two electrodes in the voltage range of 1.5-4.0 V. The corresponding coin cells exhibited open circuit potentials of around 3.4 V. The CV curve of the 7:2:1 electrode showed four reduction peaks (3.3 V, 3.1 V, 2.2 V, 1.7 V) in the first discharge, indicating a complex multi-step lithium intercalation process. As lithium ions are intercalated into the

layers of V_2O_5, the pristine α-V_2O_5 phase transforms consecutively to ε-$Li_{0.5}V_2O_5$, δ-LiV_2O_5, γ-$Li_2V_2O_5$, and ω-$Li_3V_2O_5$, respectively. Among the various $Li_xV_2O_5$ phases, the crystal structures of the γ-$Li_2V_2O_5$ and ω-$Li_3V_2O_5$ are not reversible with lithium insertion/extraction. There were only two oxidation peaks (2.7 V and 3.55 V) in the first charge. The large mismatching between cathodic and anodic peaks was attributed to the formation of the irreversible ω-$Li_3V_2O_5$ phase, which has a rock-salt cubic structure.[99] The ω-phase can't achieve full lithium delithiation in the first charge by trapping 0.4 lithium ion in its lattice.[113] The rock-salt phase also restricts lithium insertions to only obtain a final composition ω-$Li_{2.65}V_2O_5$ in the second discharge. As a result, lithium insertion/extraction is only reversible with the range of $0.4 < x < 2.65$ for ω-$Li_3V_2O_5$ phase. Some small shoulders appeared during the second discharge, similar to a previous report.[104] That is probably because non-reacted V_2O_5 in the first cycle reacts with Li^+ ions, due to the long Li^+ ion diffusion path within the large V_2O_5 particles.[225] There were only two pairs of stable redox peaks observed for the 7:2:1 electrode after the first cycle, which indicates stable reversibility.

In comparison with the CV curve of 7:2:1 electrode, the 8:1:1 electrode shows broad redox peaks with small current density. Three reduction peaks (3.1 V, 2.1 V, 1.6 V) were observed in the first discharge. The oxidation peaks were located at 3.0 V and 3.6 V in the first charging. The potential difference between reduction and oxidation peaks increased, suggesting enhanced polarization. Generally speaking, the conductivity and reversibility of 8:1:1 electrode is lower than that of 7:2:1 electrode.

Figure 4.5 illustrates the galvanostatic charge–discharge curves of the V_2O_5 electrodes with different compositions in the voltage range of 1.5-4.0 V at a current density of 0.1C. The discharge-charge plateaus of the 7:2:1 electrode corresponded to the redox peaks of its CV result. There were three typical plateaus (3.2 V, 2.3 V, and 1.85 V) in the first discharge, corresponding to the formations of δ-LiV_2O_5, γ-$Li_2V_2O_5$, and ω-$Li_3V_2O_5$ phases, respectively. The initial discharge capacity of the 7:2:1 electrode is 350 mAh g^{-1}. The first charge and the second discharge started to show smooth slopes without distinct voltage plateaus, revealing the formation of the irreversible ω-$Li_xV_2O_5$ phase. The first charge specific capacity drastically drops to 304 mAh g^{-1}. This large 1st cycle loss is 46 mAh g^{-1}, ascribed to the formations of the SEI and irreversible ω-$Li_3V_2O_5$ phase. The specific capacity further decreased to 277 mAh g^{-1} for the second discharge. In the following charge-discharge cycles, the capacity losses were much smaller, indicating that the

electrochemical reversibility of the 7:2:1 electrode became stable.[226] As for the 8:1:1 electrode, the charge-discharge profiles in the first 20 cycles are similar to those of the 7:2:1 electrode. However, the 1st cycle loss of the 8:1:1 electrode became larger by having the capacities of 349 mAh g^{-1} for the 1st discharge and 291 mAh g^{-1} for the 1st charge. The capacity also faded quickly to 268 mAh g^{-1} in the 2nd discharge. The poor reversibility of the 8:1:1 electrode was consistent with the observations in the CV curves.

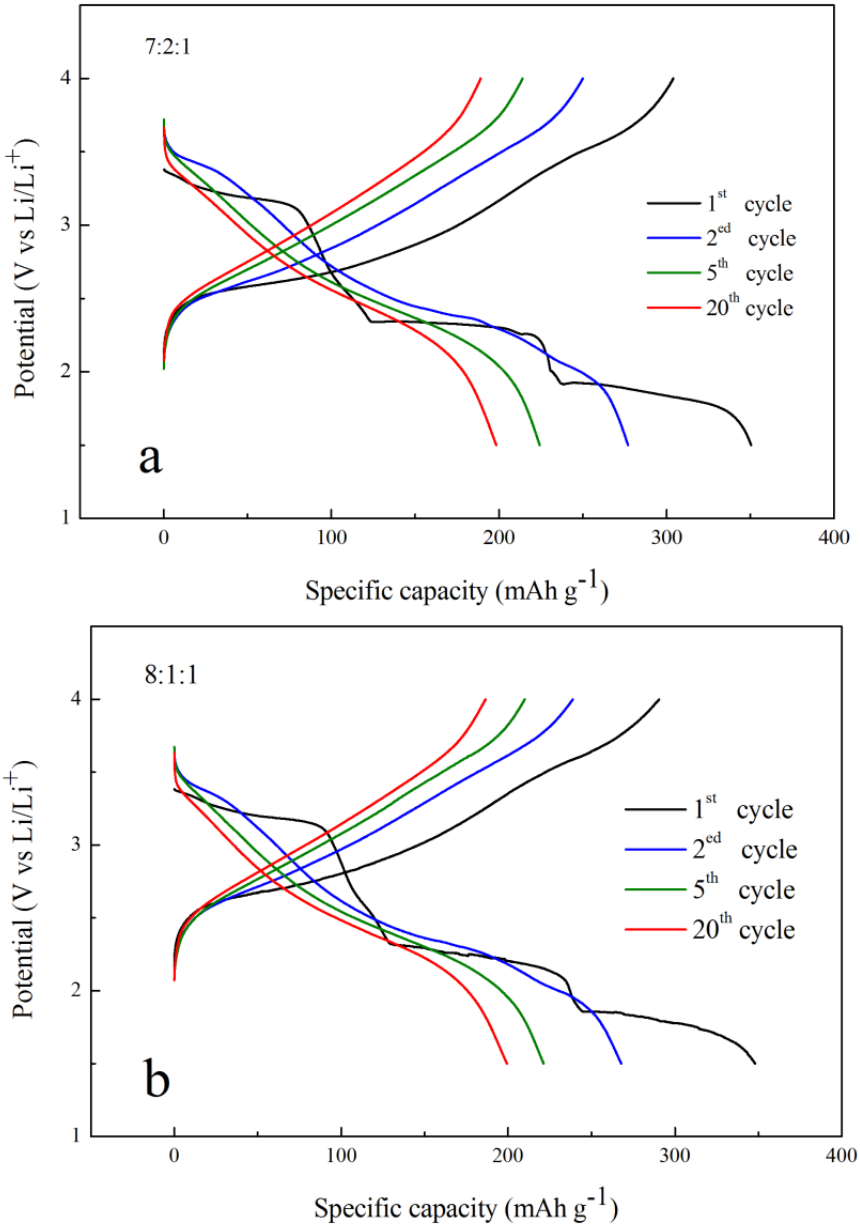

Figure 4.5 Galvanostatic charge–discharge curves of the V_2O_5 electrodes with different compositions a) 7V:2C:1P and b) 8V:1C:1P in the voltage range of 1.5-4.0 V.

Figure 4.6 shows the cycling performance of the V_2O_5 electrodes with different compositions at a current density of 0.1C in the voltage range of 1.5-4.0 V. The first discharge capacities were 351 mAh g^{-1} for 7:2:1 electrode and 348 mAh g^{-1} for 8:1:1 electrode, respectively. The discharge capacities decreased quickly in the first 20 cycles and then keep slightly reducing till 100th cycle. The large irreversible capacity loss in the initial 20 cycles should be associated with structural changes during lithiation and delithiation process, formation of a solid electrolyte interface (SEI) film, and vanadium dissolution into electrolyte.[227] The 100th discharge capacity of the 7:2:1 electrode is maintained at 164 mAh g^{-1}, corresponding to capacity retention of 47 %. The average capacity fading is 0.53 % per cycle. The 8:1:1 electrode had the 100th discharge capacity of 122 mAh g^{-1}, corresponding to capacity retention of 35 % and the average capacity fading is 0.65 % per cycle.

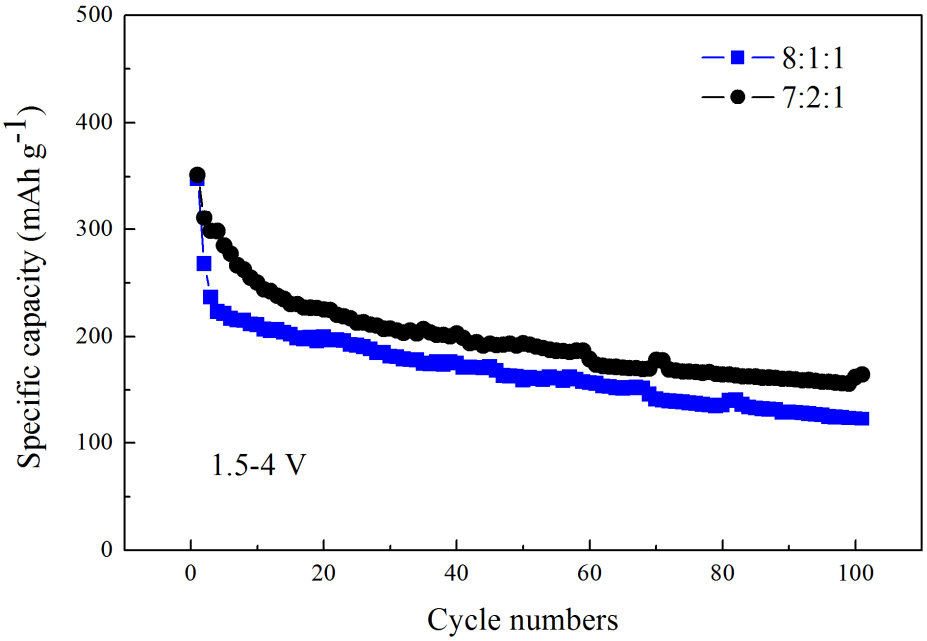

Figure 4.6 Cycling performance of the V_2O_5 electrodes with different compositions at a current density of 0.1 C in the voltage range of 1.5-4.0 V.

The rate performance (Figure 4.7) of the V_2O_5 electrodes was measured in the voltage range of 1.5-4.0 V. The capacity fading of both electrodes at low current densities were slow. The 7:2:1 electrode delivered specific discharge capacities of 247, 218, 187, 154, and 111 mAh g^{-1} at 0.1C, 0.2C, 0.5C, 1C, and 2C, respectively. In contrast, the specific discharge capacities of the 8:1:1 electrode were 219, 180, 150, 105, and 41 mAh g^{-1} at 0.1C, 0.2C, 0.5C, 1C, and 2C, respectively. At the current rate of 2C, the 7:2:1 electrode

remained 32% of the initial capacity, while the 8:1:1 electrode only preserved 12% of the initial capacity. Notably, the capacity of both electrodes quickly dropped close to 0 mAh g^{-1} when current rates increased up to 5 C and 10 C. The absence of discharging meant that the battery voltage dropped below the cut-off voltage (1.5 V), as the internal polarization resistance was too high at high current densities.[228]

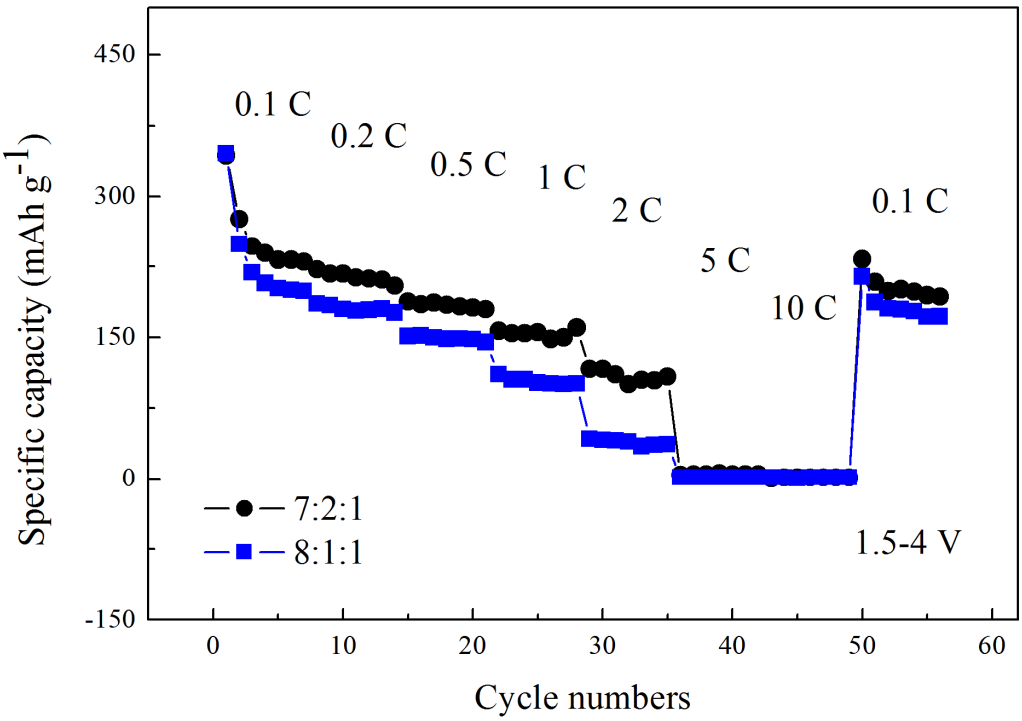

Figure 4.7 Rate performance of the V_2O_5 electrodes with different compositions in the voltage range of 1.5-4.0 V.

The electrochemical impedance spectra (EIS) of the V_2O_5 electrodes were shown in Figure 4.8. For a typical EIS measurement, the AC potential of 5 mV in the frequency range of 100 kHz - 1 mHz was applied to the open circuit voltage of a coin cell. There were two components in the EIS spectra of the V_2O_5 electrodes. The depressed semicircles in the range of high-to-medium frequencies were determined by the charge-transfer on the electrolyte/electrode interface. The diameter of a semicircle represents the charge transfer resistances (R_{ct}). The linear tails in the low-frequency range were related to the diffusion of Li^+ ions within the V_2O_5 lattice. The semicircle diameter of the 7:2:1 electrode was much smaller than that of the 8:1:1 electrode. The smaller charge-transfer resistance of the 7:2:1 electrode verified the better conductive network within the 7:2:1 electrode. This was in line with the observations in the CV curves.

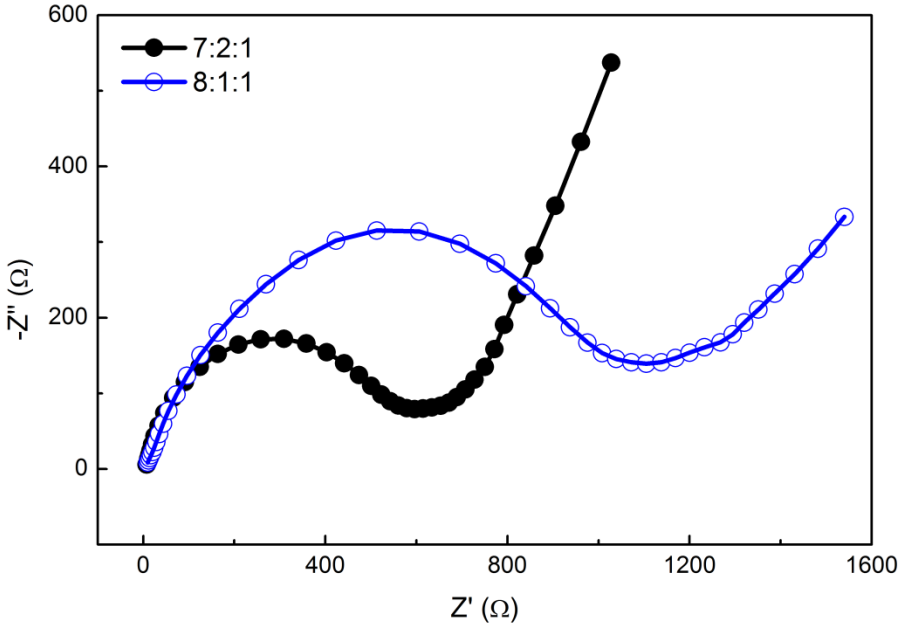

Figure 4.8 Electrochemical impedance spectra of the V_2O_5 electrodes with different compositions measured from 100 kHz to 1 mHz with a voltage amplitude of 5 mV.

The above electrochemical data confirmed that the battery performance of the 8:1:1 electrode was inferior to that of the 7:2:1 electrode. The 8:1:1 electrode exhibited faster capacity fading and lower rate capability. The less amount of carbon black in the 8:1:1 electrode resulted in lower electric conductivity of the electrode. The polarization resistance of the 8:1:1 electrode was also enhanced. Therefore, the electrode composition of 7:2:1 is preferred by V_2O_5 to show optimal battery performance.

4.3.3 **Effects of voltage window**

Lithium insertions/extraction in V_2O_5 is highly associated with the voltage window for charge and discharge. When tested between 1.5 and 4 V, the V_2O_5 can be transformed into the irreversible ω-$Li_xV_2O_5$ phase, which not only shows structural irreversibility, but also restricts the lithium reversibility within a limited range. The formation of the ω-$Li_xV_2O_5$ phase leads to large capacity loss and poor cycling stability. The battery performance of V_2O_5 can be enhanced by excluding the ω-$Li_xV_2O_5$ phase. A narrower voltage window of 2-4 V can avoid deep discharge and the formation of the ω-$Li_xV_2O_5$ phase. It is of significance to investigate the effects of the small voltage window on the electrochemical properties of V_2O_5.

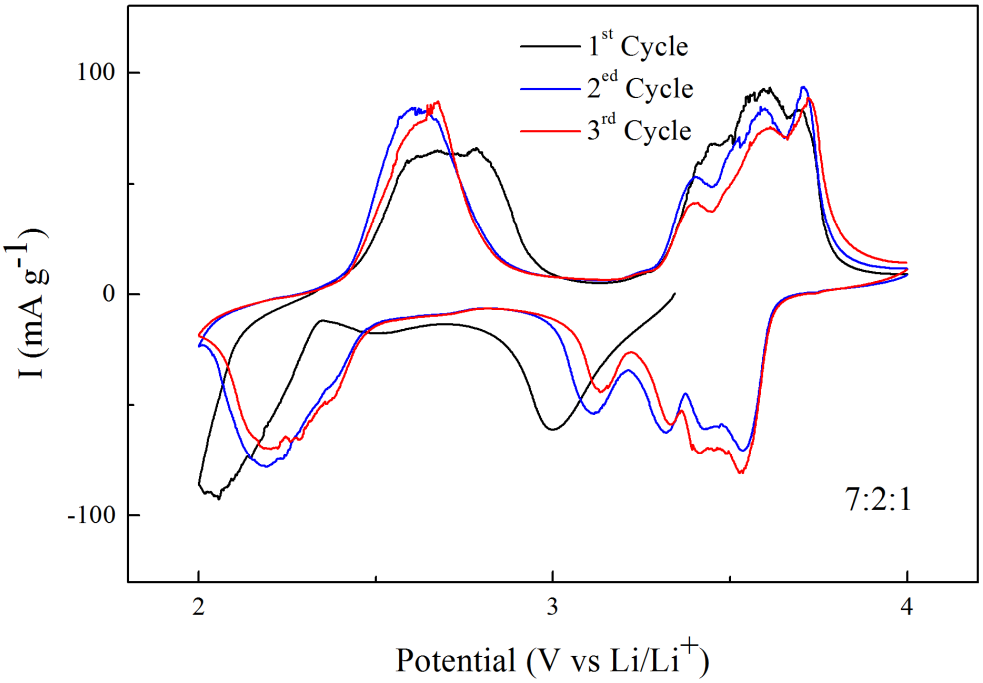

Figure 4.9 Cyclic voltammograms (first three cycles) of the 7V:2C:1P V_2O_5 electrode in the voltage range of 2.0-4.0 V.

Figure 4.9 shows the CV curves of the 7:2:1 V_2O_5 electrode in the voltage range of 2.0-4.0 V. The CV curves showed good reversibility with paired redox peaks. The cathodic peaks at 3.3 V, 3.1 V, and 2.2 V are caused by lithium intercalation to form ε-$Li_{0.5}V_2O_5$, δ-LiV_2O_5, and γ-$Li_2V_2O_5$ phases, respectively. Three anodic peaks at 2.6 V, 3.4, and 3.6 V are associated with the Li^+ ion deintercalation process of forming δ-LiV_2O_5, ε-$Li_{0.5}V_2O_5$, and α-V_2O_5, respectively. The redox pairs at 3.1/3.4 V and 2.2/2.6 V showed reduced potential differences, in comparison with those of the CV curves in 1.5-4 V. Extra redox peaks also appear as shoulders in the CV curves. When more than one lithium ion is intercalated into V_2O_5, the γ-$Li_2V_2O_5$ phase with an irreversible crystal structure is formed.[99] This irreversible structural changes might induce the mixture of α, ε and δ, γ phases, which is responsible for the extra peaks in the CV curves.[151] The Li insertion/extraction is still fully reversible in the γ-$Li_2V_2O_5$ phase. In general, the CV curve in the range of 2-4 V is more symmetrical than that of 1.5–4.0 V, illustrating better electrochemical reversibility. It is thus expected that charge–discharge cycling performance of V_2O_5 is better over the range of 2-4 V.

In the charge-discharge curves (Figure 4.10) of the 7:2:1 V_2O_5 electrode over the range of 2-4 V, both charging and discharge exhibited stable voltage plateaus, indicating good

structural stability during Li-ion insertion and extraction. The plateaus at 3.1 V and 2.3 V are ascribed to the formations of δ-LiV_2O_5 and γ-$Li_2V_2O_5$ phases. Moreover, multiple poorly-defined voltage plateaus also exist, consistent with the complex peaks in the CV curves. The first discharge capacity of 221 mAh g^{-1} is lower than the second discharge capacity of 250 mAh g^{-1}. This can be associated with an activation process with a slight increase in the discharge capacity for the first few cycles.[229] The capacity retention in first 20 cycles is 68% between 2 V and 4 V, while the value is 43% for the voltage window 1.5-4 V. Generally, the 7:2:1 V_2O_5 electrode exhibited lower capacity loss and better electrochemical irreversibility in the narrow voltage window of 2-4 V.

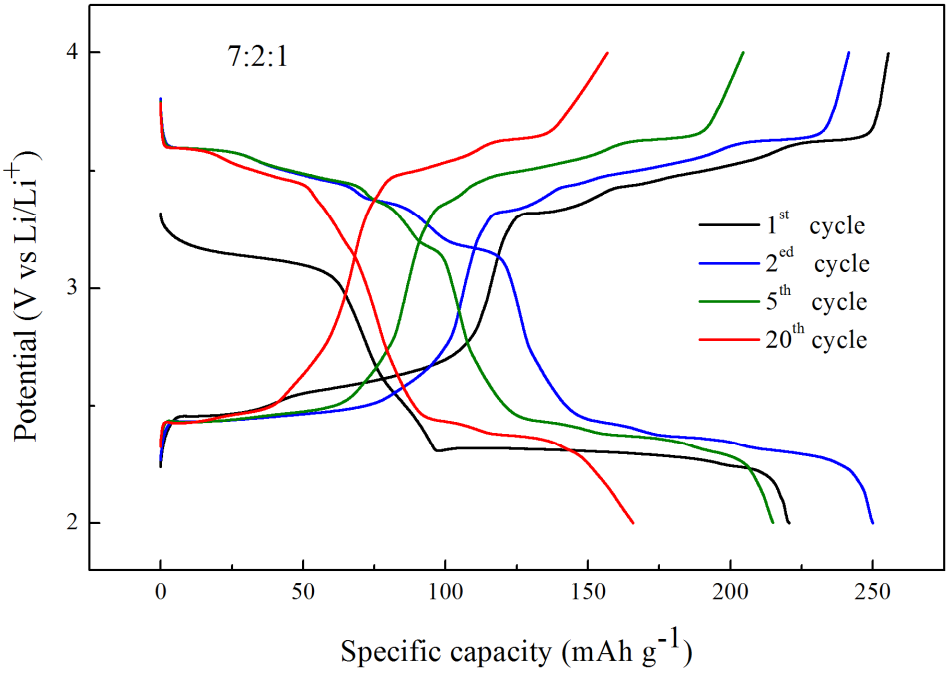

Figure 4.10 Galvanostatic charge–discharge curves of the 7V:2C:1P V_2O_5 electrode at a current density of 0.1 C in the voltage ranges of 2.0-4.0 V.

Figure 4.11a showed the cycling performance of the 7:2:1 V_2O_5 electrode in the voltage range of 2-4 V at a current density of 0.2 C for the first 100 cycles. The commercial V_2O_5 possessed the initial capacity of 256 mAh g^{-1} and the 100th capacity of 197 mAh g^{-1}. The capacity retention was 77% in 100 cycles, corresponding to an average capacity fading of 0.23 % per cycle. In comparison, the average capacity fading in the first 100 cycles is 0.53 % per cycle in the voltage range of 1.5-4 V. Figure 4.11b presents the rate performance of commercial V_2O_5 powder in the voltage range of 2.0-4.0 V. The commercial V_2O_5 exhibited quick capacity fading as current density increases. The capacity of V_2O_5 only remained

(132 mAh g^{-1}) half of the initial at 0.6C, and quickly dropped to 0 mAh g^{-1} at 3C with no discharging. The V_2O_5 showed specific discharge capacities of 254, 231, 135, and 118 mAh g^{-1} at 0.1 C, 0.3 C, 0.6 C, and 1C, respectively. The specific capacity at 1C corresponds to 45% of the initial capacity. The specific capacity of the 7:2:1 V_2O_5 electrode was recovered to 240 mAh g^{-1} when the current was set from 6C back to 0.1C. The rate performances of the 7:2:1 electrodes were still poor in the voltage ranges of both 1.5-4 V and 2-4 V, particularly at high current rate of above 2C. The low electric conductivity of V_2O_5 is responsible for the poor rate capabilities.

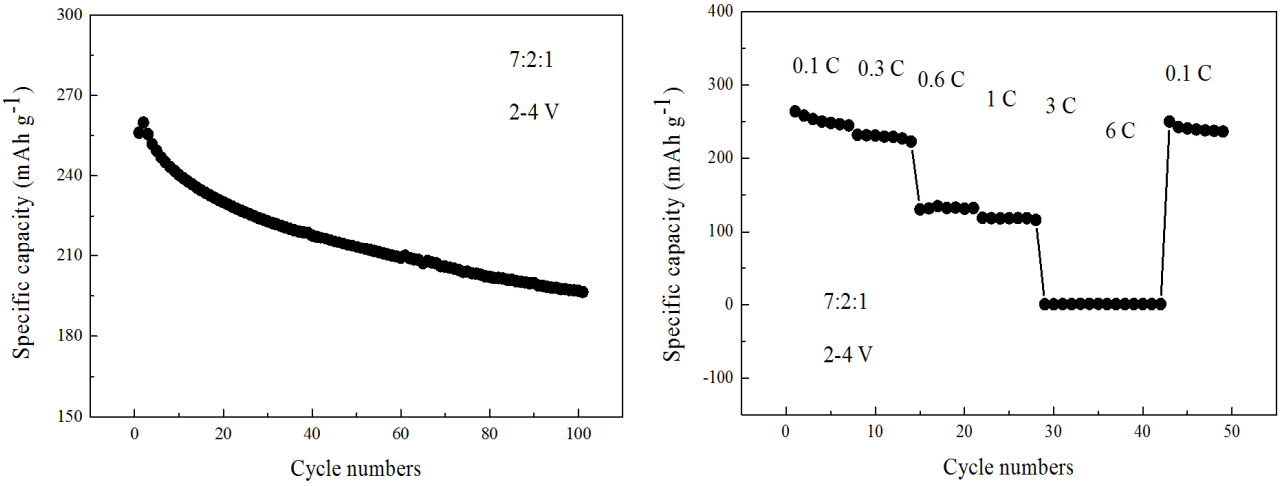

Figure 4.11 Cycling a) and rate b) performance of the 7V:2C:1P V_2O_5 electrode in the voltage range of 2-4 V.

4.3.4 **Conclusions**

In summary, the electrochemical properties of the commercial V_2O_5 powder are closely associated with electrode compositions and voltage windows. Two electrodes with the different compositions of 7:2:1 and 8:1:1 were employed to study the effects of electrode compositions on electrochemical properties between 1.5 and 4 V. The electrode composition of 7:2:1 gave rise to better battery performance. Due to the higher electric conductivity, the 7:2:1 V_2O_5 electrode exhibited improvements in electrochemical reversibility, cycling stability, and rate performance. The narrow voltage window of 2-4 V was selected to further enhance the battery performance of the 7:2:1 V_2O_5 electrode. The charge and discharge between 2 and 4 V eliminated the formation of irreversible ω-$Li_3V_2O_5$ phase and restricted V_2O_5 to have a maximum two lithium intercalation. The 7:2:1

V_2O_5 electrode achieved better electrochemical reversibility and cycling performance in the voltage range of 2-4 V. The average capacity fading of the 7:2:1 V_2O_5 electrode in the first 100 cycles is 0.23 % per cycle between 2-4 V, which is less than half of 0.53 % per cycle in the voltage range of 1.5-4 V.

5 A comparative study of V_2O_5 modified with multi-walled carbon nanotubes and poly(3,4-ethylenedioxythiophene) for lithium-ion batteries

5.1 Introduction

Vanadium pentoxide (V_2O_5) surpasses other conventional cathode material in terms of high energy density. But several drawbacks prevents its commercial use as a cathode in lithium-ion batteries, such as small Li^+ diffusion coefficient, low electrical conductivity, dissolution of vanadium into some electrolytes, and irreversible phase transitions for deep discharge.[42,43,110] To solve these problems, effective strategies are to modify V_2O_5 with carbon materials or conductive polymers.[106,146,149,150] Such modifications not only improve electrical conductivity and structural stability, but also prevent particle aggregation.

Multi-walled carbon nanotubes (MWCNTs) have been shown to be an effective carbon to improve the electrochemical performance of V_2O_5. Seng *et al.* reported a physical mixing method to modify V_2O_5 nanowires with MWCNTs.[230] The composite electrode possessed a capacity of 140 mAh g^{-1} after 50 cycles in the voltage range of 2.5–4.0 V, much higher than that of pure V_2O_5 nanowires (90 mAh g^{-1}). Jia *et al.* described an *in-situ* hydrothermal treatment approach to preparing V_2O_5/MWCNT nanocomposite electrode materials, which showed an excellent rate capability with a capacity of 169 mAh g^{-1} at 10C between 1.8 and 4.0 V (*vs.* Li^+/Li).[147] Using the layer-by-layer assembly strategy, Sun *et al.* prepared composite materials containing V_2O_5 nano-spheres and MWCNTs with a high reversible capacity of 275 mAh g^{-1} at 0.1C for the 50th cycle, realizing over 93% of the initial discharge capacity.[204]

Poly(3,4-ethylenedioxythiophene) (PEDOT) is a popular conductive polymer with a high electrical conductivity (550 S cm^{-1}) and a good electrochemical stability.[231] Chao *et al.* reported that V_2O_5/PEDOT core-shell nanobelt arrays possessed a specific capacity of 168 mAh g^{-1} at an extremely high rate (60C) for the 1000th cycle, corresponding to a capacity retention of 98%.[195] Mai *et al.* reported that a cucumber-like MnO_2 nanoparticle-enriched V_2O_5/PEDOT coaxial nanowire composite exhibited a capacity fading of 0.19% per cycle over 40 cycles at the current density of 50 mA/g, much smaller than the 1.46% of V_2O_5 nanowires.[231] Song *et al.* found that a composite electrode of V_2O_5 nanowire and PEDOT showed a great rate performance at 100 °C.[196]

As PEDOT and MWCNTs are both favorable for improving the battery performance of V_2O_5, it is of interest to investigate the combined effect of MWCNTs and PEDOT on the electrochemical property of V_2O_5. In this chapter, V_2O_5 was modified with MWCNTs and PEDOT by using physical mixing and chemical oxidative polymerization methods. The effect of the conductive additives on material properties and electrochemical properties was investigated. It was found that one of the composites containing only 10 wt% PEDOT possessed a capacity of 235 mAh g^{-1} for the 100th cycle at 0.2C, corresponding to a capacity retention of 94%. This sample also showed a good rate capability with a capacity of 125 mAh g^{-1} at 6C.

5.2 Experimental

A commercial V_2O_5 was obtained from Sigma-Aldrich. It was composed of micro-flakes that showed lengths of 1-2 μm, widths of 0.5-1 μm, and thicknesses of 200-600 nm. A MWCNT sample with diameters ranging from 8 to 15 μm and length of about 50 μm was supplied by Chengdu Organic Chemicals Co. Ltd., China. The rest chemicals used in the present work were purchased from Sigma-Aldrich.

5.2.1 **Modification of V_2O_5 with MWCNTs**

The physical mixing method was used to modify V_2O_5 with MWCNTs. Four samples with 5 wt%, 10 wt%, 15 wt%, and 20 wt% of MWCNTs, were prepared and were denoted as VC5, VC10, VC15, and VC20, respectively. In brief, 300 mg of commercial V_2O_5 powder was physically mixed with appropriate amount of MWCNTs in 40 mL of ethanol under

stirring for 30 min, followed by ultrasonication for 60 min. The solid products were filtered off, washed with ethanol, and then dried at 70 °C in a vacuum oven.

5.2.2 **Modification of V_2O_5 with PEDOT**

The PEDOT-modified V_2O_5 samples were prepared by using the chemical oxidative polymerization method as described elsewhere.[231] Four samples with PEDOT contents of 5 wt%, 10 wt%, 15 wt%, and 20 wt% were prepared and were denoted as VP5, VP10, VP15, and VP20, respectively. In brief, 100 mg of V_2O_5 was dispersed in 40 mL of acetonitrile under stirring for 10 min, followed ultrasonic treatment for 20 min. The mixture was transferred to a flask. A given amount of 3,4-ethylenedioxythiophene (EDOT) monomer was added under vigorous magnetic stirring for 60 min. Oxidizing agent $FeCl_3$ dissolved in 20 mL of acetonitrile was dropwise added. The final solution was refluxed at 86 °C for 12 h. The high reaction temperature is able to increase the PEDOT yield.[232] Dark blue products were filtered off, washed with ethanol and deionized water, and then dried at 70 °C in a vacuum oven.

5.2.3 **Modification of V_2O_5 with both MWCNTs and PEDOT**

The MWCNT-modified samples (VC5, VC10, VC15, and VC20) were subjected to further modification with 10 wt% of PEDOT to obtain samples VC5P10, VC10P10, VC15P10, and VC20P10, respectively. The preparation procedure was the same as that for the sample VP10.

5.2.4 **Characterization**

X-ray diffraction (XRD) measurements were performed on a Shimadzu diffractometer (XRD–6000, Tokyo, Japan) with Cu Kα radiation at a step size of 0.01º per second. Sample morphology was investigated using a JEOL SU3500 scanning electron microscopy (SEM). Thermal gravimetric analysis (TGA) was conducted in air from room temperature to 650 °C at a heating rate of 10 °C min^{-1} on a Shimadzu DTG-60A analyzer. Attenuated total reflection-Fourier transform infrared (ATR-FTIR) spectra were collected on a ThermoNicolet Nexus 6700 spectrometer equipped with a Diamond ATR accessory. For

each spectrum, 128 scans were collected at a resolution of 4 cm^{-1} over the range of 400-4000 cm^{-1}. Energy dispersive X-Ray (EDX) spectroscopy analysis was conducted on a transmission electron microscopy (TEM, JEOL JEM-2100) equipped with an energy-dispersive X-ray analyzer. X-ray photoelectron spectroscopy (XPS) spectra were acquired with a Kratos Axis ULTRA X-ray photoelectron spectrometer with a 165 mm hemispherical electron energy analyzer and monochromatic Al Kα (1486.6 eV) radiation at 225 W (15 kV, 15 mA).

5.2.5 **Electrochemical measurements**

The electrodes were fabricated by mixing an electroactive material, carbon black and polyvinylidene fluoride (PVDF) at a mass ratio of 70:20:10 in N-methyl-2-pyrrolidone (NMP). The slurry was coated onto an aluminum foil and dried at 70 °C for 12 h. The foil was then punched into small disks with a diameter of 14 mm. The mass loading of each active material was around 2 mg. Metallic lithium disk was used as the anode. The electrolyte solution was made up of 1.0 M $LiPF_6$ in ethylene carbonate (EC) and dimethyl carbonate (DMC) (1:1, w/w). CR2032 coin-type cells were assembled in an argon-filled glove box, where both moisture and oxygen levels were less than 0.1 ppm. The cells were charged and discharged over the voltage range of 2.0–4.0 V (*vs.* Li/Li^+) at different current rates by using a Battery Testing System (Neware, China). Cyclic voltammetry (CV) measurements were performed on a CHI 660b electrochemical workstation at a scanning rate of 0.1 mV s^{-1} over a voltage range of 2.0–4.0 V.

5.3 Results and discussion

5.3.1 **Physical characterization**

Figure 5.1 shows the XRD patterns of some representative samples. It can be seen that pure PEDOT exhibits three diffraction peaks at 6.5°, 12.8°, and 26.2°, which were indexed to (001), (002), and (110) planes.[198,233] The peaks at 2θ = 6.5° and 12.8° can be assigned to a structurally similar system where the interchain packing is along the pseudo-orthorhombic *a* axis, while the diffraction peak at 2*θ* = 26.2° can be attributed to the inter-chain planar ring-stacking distance.[234] As for pure MWCNTs, two diffraction peaks appear at 25.9° and 43.4°, corresponding to (002) and (100) planes respectively.[235] The

VC5, VP10, and VC5P10 samples were selected as representatives of composite samples. All the peaks of the three samples can be indexed to the orthorhombic V_2O_5 phase (JCPDS card no. 77-2418, space group: *Pmnm (59), a = 11.512 Å, b =3.564 Å, c= 4.368 Å*),[236] indicating that the main crystalline phase in these samples is V_2O_5. The peaks of MWCNTs and PEDOT were masked by the strong diffraction pattern of V_2O_5. The peak positions of VC5, VP10, and VC5P10 were consistent, indicating that the crystal structure of V_2O_5 was not changed by adding MWCNTs and PEDOT.

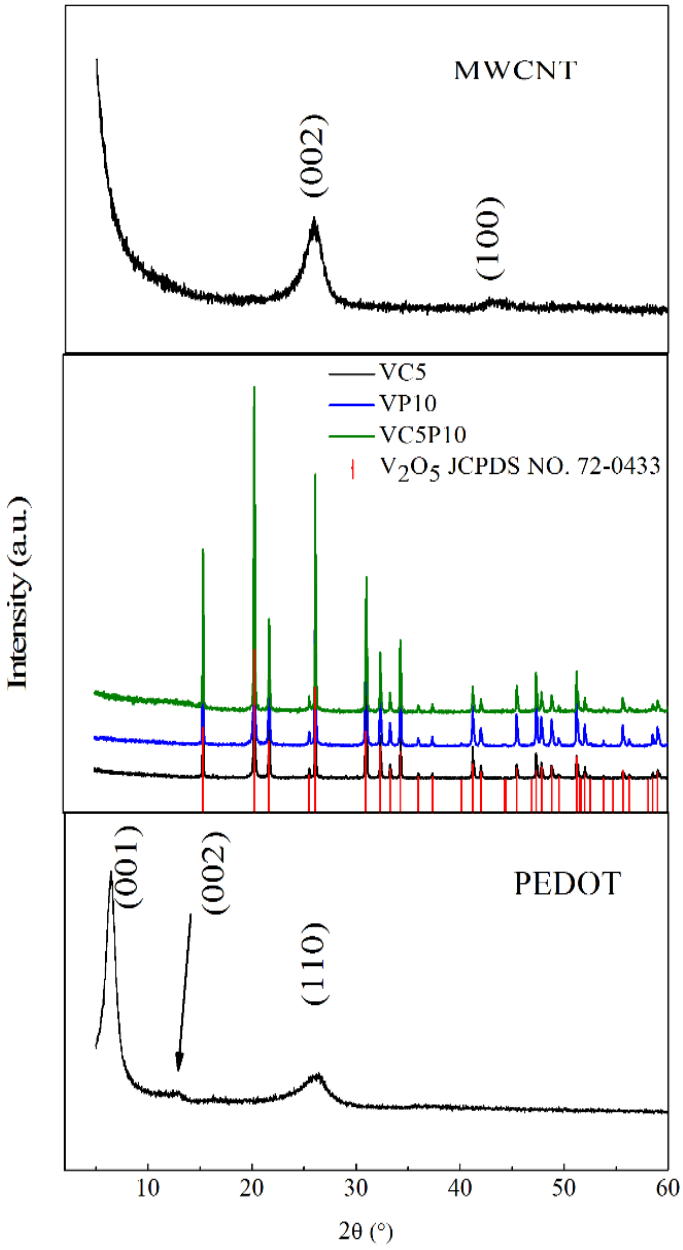

Figure 5.1 XRD patterns of different samples.

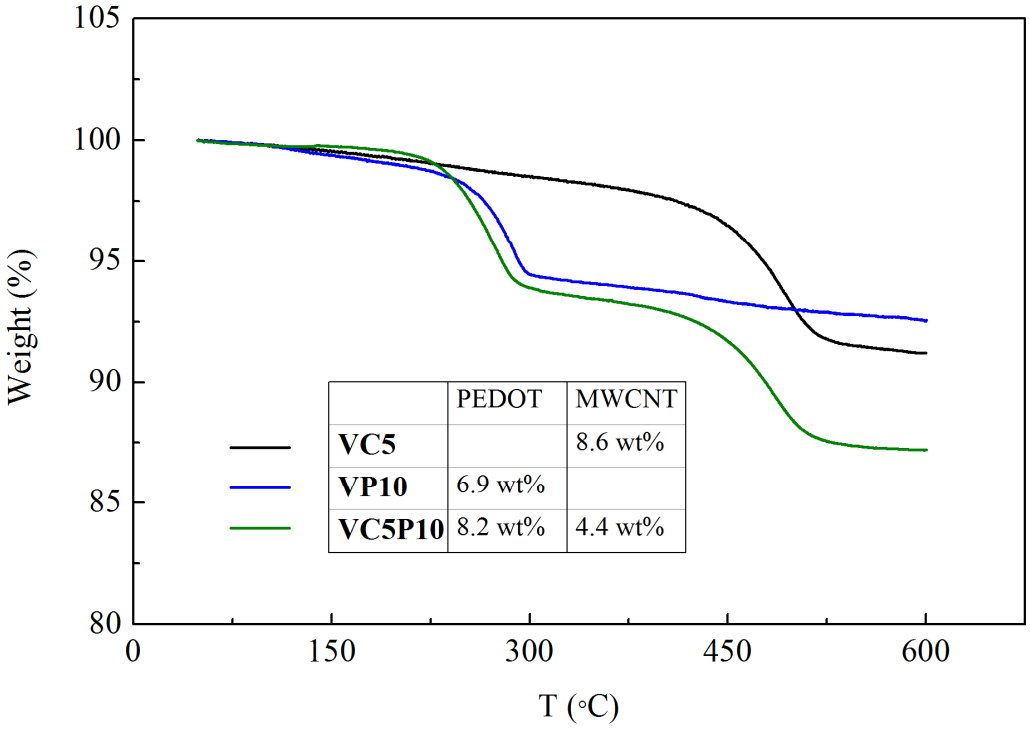

Figure 5.2 TGA curves of VC5, VP10, and VC5P10.

Figure 5.2 shows the thermogravimetric analysis (TGA) of the samples VC5, VP10 and VC5P10. All samples exhibited linear weight loss below 150 °C due to the removal of residual bound water and gas. The VC5 showed a dramatic weight-loss from 400 °C, corresponding to the weight loss by burning off MWCNTs. The MWCNT content of the VC5 was calculated to be 8.6 wt%. In comparison, The VP10 sample contained 6.9 wt% of PEDOT that was decomposed through two weight-loss processes. The weight loss between 150 °C and 400 °C was ascribed to the decomposition of the ethylenedioxy groups of the PEDOT.[197] The loss after 400 °C was caused by the combustion of polymer components. The TGA curve of VC5P10 combined all features of both VC5 and VP10. The result revealed that VC5P10 included 8.2 wt% of PEDOT and 4.4 wt% of MWCNTs.

Figure 5.3 shows the SEM images of samples V_2O_5, VC5, VP10, and VC5P10. Commercial V_2O_5 consists of micron-flakes, which have sizes of 1-2 μm in length, 0.5-1 μm in width, and 200-600 nm in thickness. In the VC5 samples, V_2O_5 particles were intermixed with MWCNTs. However, the intertwining of V_2O_5 and MWCNTs was not highly even due to physical mixing. After the formation of PEDOT polymer, VP10 and VC5P10 display similar morphology to V_2O_5 and VC5, respectively. The elemental distributions of VP10 were investigated by energy-dispersive X-ray mapping (Figure 5.4). Vanadium,

oxygen, and sulfur were observed to distribute evenly along the VP10 particle. Sulfur is the signature of PEDOT, demonstrating the existence of PEDOT. EDX and SEM images were consistent, indicating that PEDOT was uniformly distributed on the surface of the V_2O_5 particles.

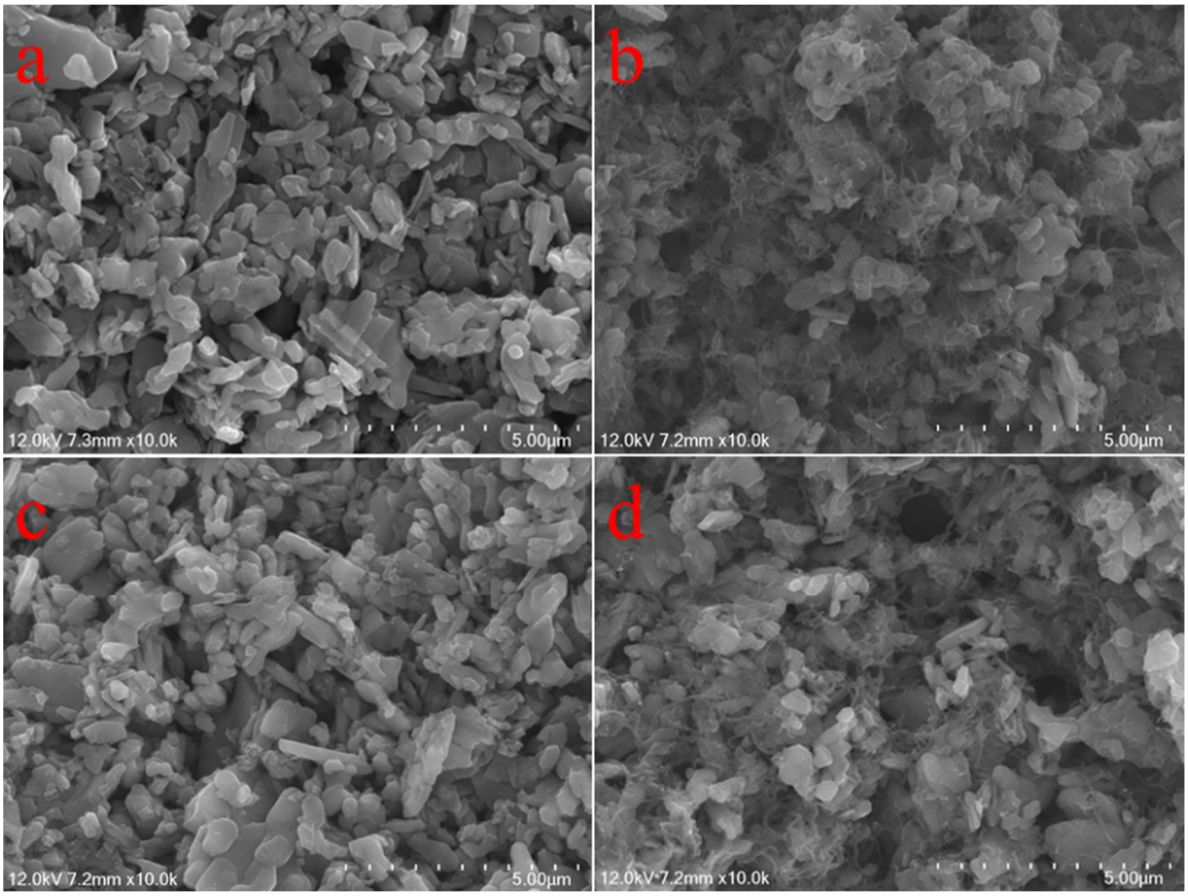

Figure 5.3 SEM images of a) V_2O_5, b) VC5, c) VP10, and d) VC5P10.

The V 2p and S 2p XPS spectra of the VP10 sample are presented in Figure 5.5. The V 2p and S 2p peaks arose from V_2O_5 and PEDOT, respectively. The V $2p_{3/2}$ signal was the sum of three peaks at 518.7 and 517.6, 516.2 eV, corresponding to V^{5+}, V^{4+}, and V^{3+}, respectively. The element of V^{4+} was the dominant specie, which was converted from V^{5+} during the polymerization process. Trace element V^{3+} was also formed due to the deep oxidation of the PEDOT monomer. V_2O_5 should act as an oxidizing agent for EDOT monomers.[237] The S 2p signals showed S $2p_{3/2}$ (164.0 eV), S $2p_{1/2}$ (165.2 eV), and an asymmetric tail at higher binding energies. The asymmetric tail is the result of positively charged sulfur within the thiophene ring (delocalization of π electrons) of PEDOT.[238]

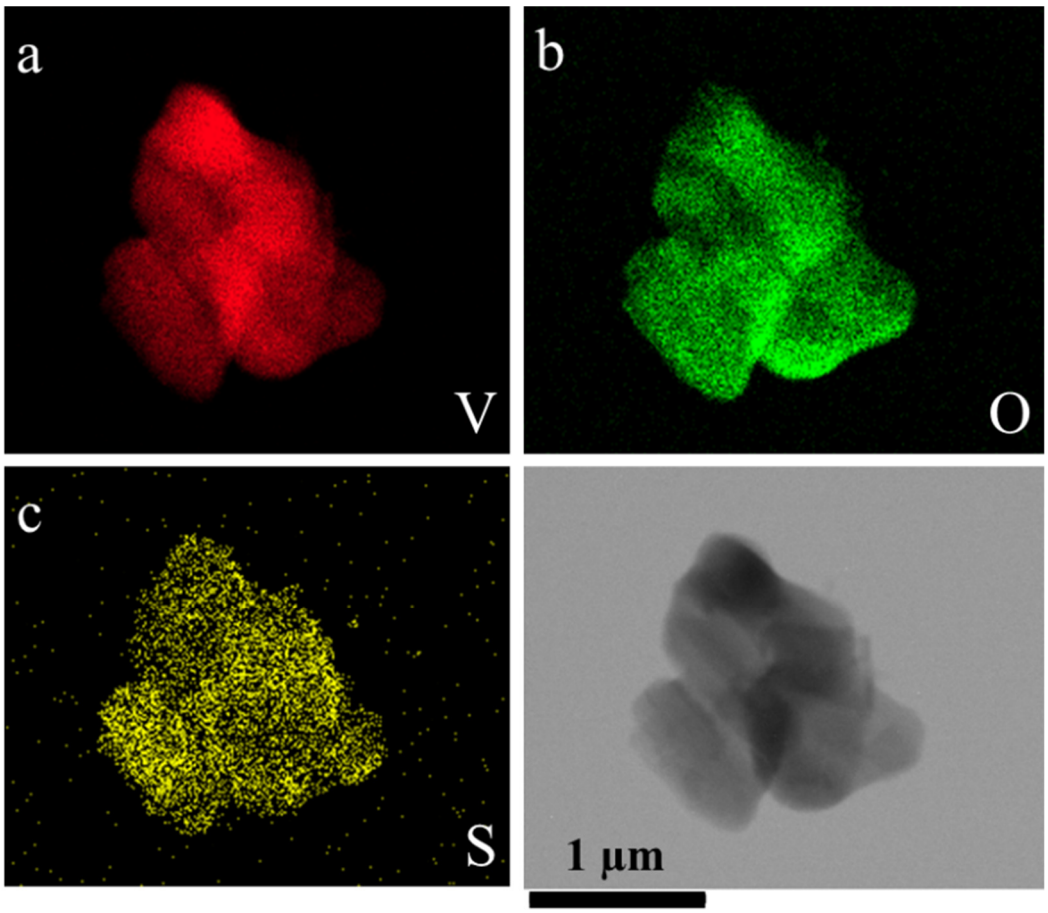

Figure 5.4 EDS mapping of a) V, b) O, c) S, and d) dark field TEM image of sample VP10.

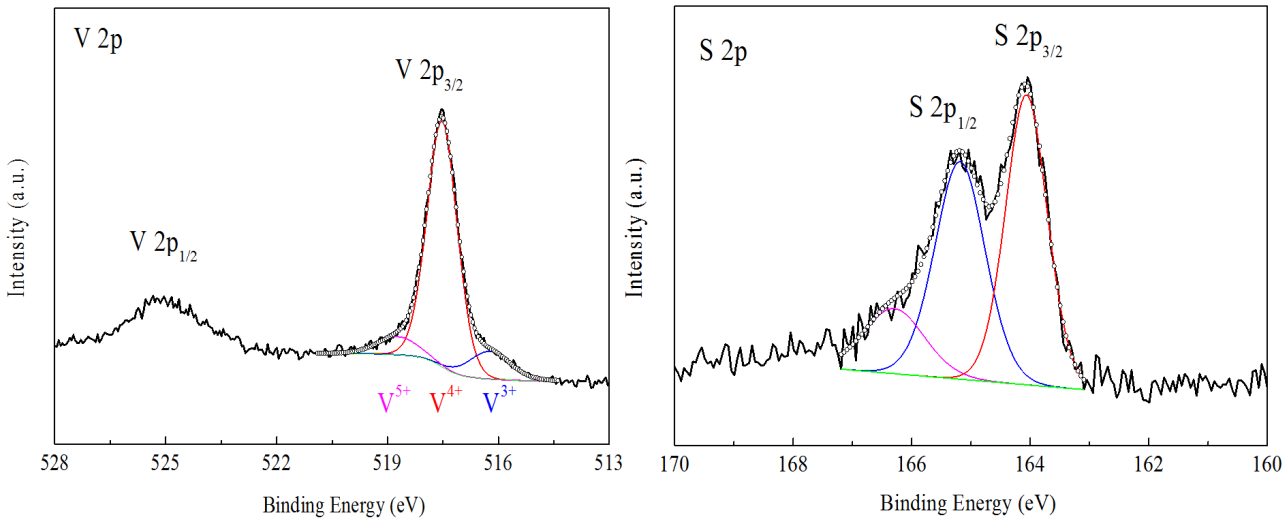

Figure 5.5 V 2p and S 2p XPS spectra of sample VP10.

The ATR-FTIR spectra of different materials were showed in Figure 5.6. The characteristic peaks of PEDOT, MWCNT, and V_2O_5 can be observed. The three main absorption bands

of V_2O_5 were found at around 1003, 803, 592 cm^{-1}, corresponding to terminal oxygen symmetric stretching mode of V=O, bridging oxygen asymmetric and symmetric stretching mode of V-O-V, respectively.[196] In the spectrum of pure PEDOT, the vibrations at 1293 and 1505 cm^{-1} resulted from the C–C and C=C stretching of the quinoidal structure of the thiophene ring. The vibrations at 1166, 1078 and 1034 cm^{-1} may originate from C–O–C bond stretching in the ethylenedioxy group. The C–S bond stretching in the thiophene ring can also be seen at 959, 825, and 661 cm^{-1}.[239] The bands of VP10 and VC5P10 were all assigned to PEDOT and V_2O_5, among which the intensity of V_2O_5 bands was reduced. It suggested that PEDOT in VP10 and VC5P10 was formed on the surfaces of V_2O_5 and MWCNTs.

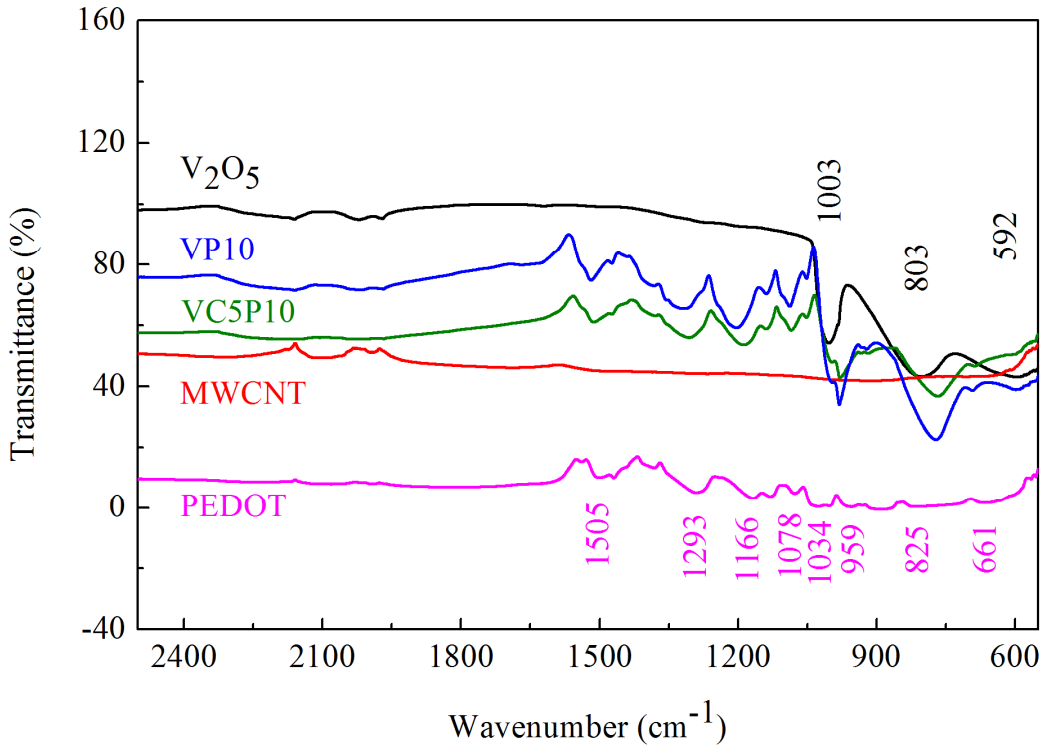

Figure 5.6 ATR-FTIR spectra of V_2O_5, PEDOT, MWCNT, VP10, and VC5P10.

5.3.2 **Electrochemical characterization**

Figure 5.7 shows the CV curves of different samples at the 3rd cycle measured between 2.0-4.0 V. Three pairs of main redox peaks can be observed for the commercial V_2O_5. The cathodic peaks at 3.33, 3.14, and 2.20 V were due to the formation of ε-$Li_{0.5}V_2O_5$, δ-LiV_2O_5, and γ-$Li_2V_2O_5$ phases, respectively. The discharge electrochemical reactions related to these phase transitions can be expressed as Equation 5.1: [240]

$\alpha\text{-}V_2O_5 + 0.5Li^+ + 0.5e^- \rightarrow \varepsilon\text{-}Li_{0.5}V_2O_5$

$\varepsilon\text{-}Li_{0.5}V_2O_5 + 0.5Li^+ + 0.5e^- \rightarrow \delta\text{-}LiV_2O_5$

$\delta\text{-}LiV_2O_5 + 1Li^+ + 1e^- \rightarrow \gamma\text{-}Li_2V_2O_5$

Three anodic peaks at 3.49, 3.39, and 2.67 V emerged when the active material changed its phase back to $\delta\text{-}LiV_2O_5$, $\varepsilon\text{-}Li_{0.5}V_2O_5$, and $\alpha\text{-}V_2O_5$, respectively.[241] Compared with V_2O_5, the current densities of those modified samples were larger, indicating that their electrical conductivities were enhanced due to the presence of electrically conductive MWCNTs and PEDOT. In particular, VP20 possessed the highest current density among the materials. The VP20 sample displayed cathodic peaks at 3.36 V, 3.16 V, and 2.20 V, and anodic peaks at 3.46 V, 3.39 V, and 2.60 V, respectively. The potential differences between the cathodic and anodic peaks were 0.1 V, 0.23 V, 0.4 V, which are smaller than that of V_2O_5 (0.16 V, 0.25 V, and 0.47 V). This suggests that the polarization of sample VP20 was reduced. [180,229] Besides the three pairs of main redox peaks, there were also other peaks observed, which are related to the irreversible structural changes of $Li_xV_2O_5$ during cycling. [240] [151]

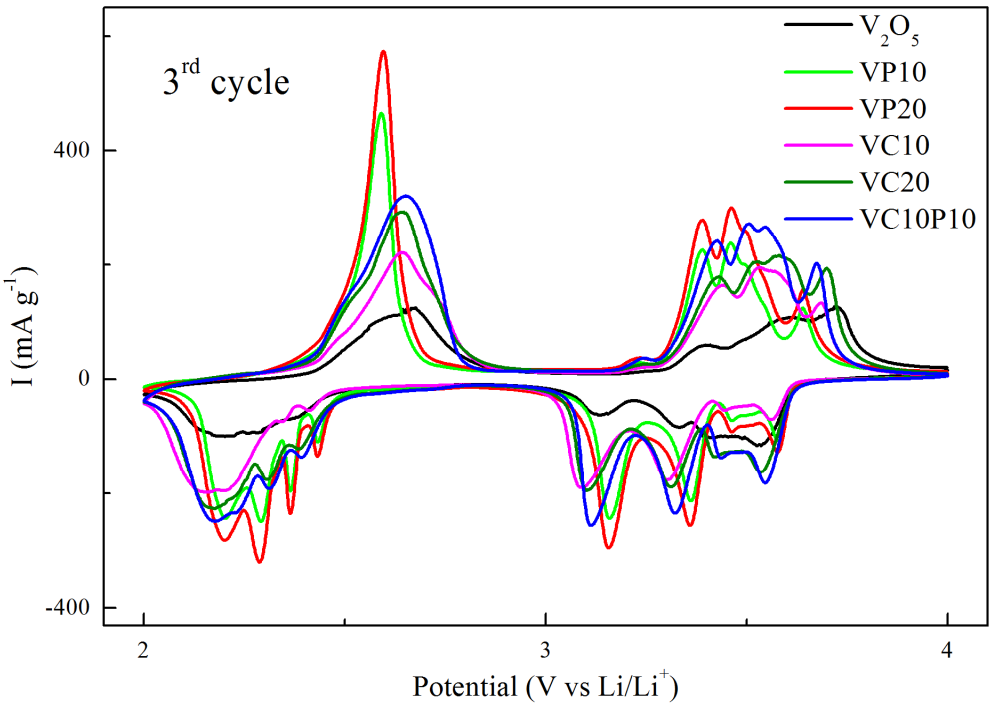

Figure 5.7 CV curves of V_2O_5, VP10, VP20, VC10, VC20, and VC10P10 for the 3rd cycle.

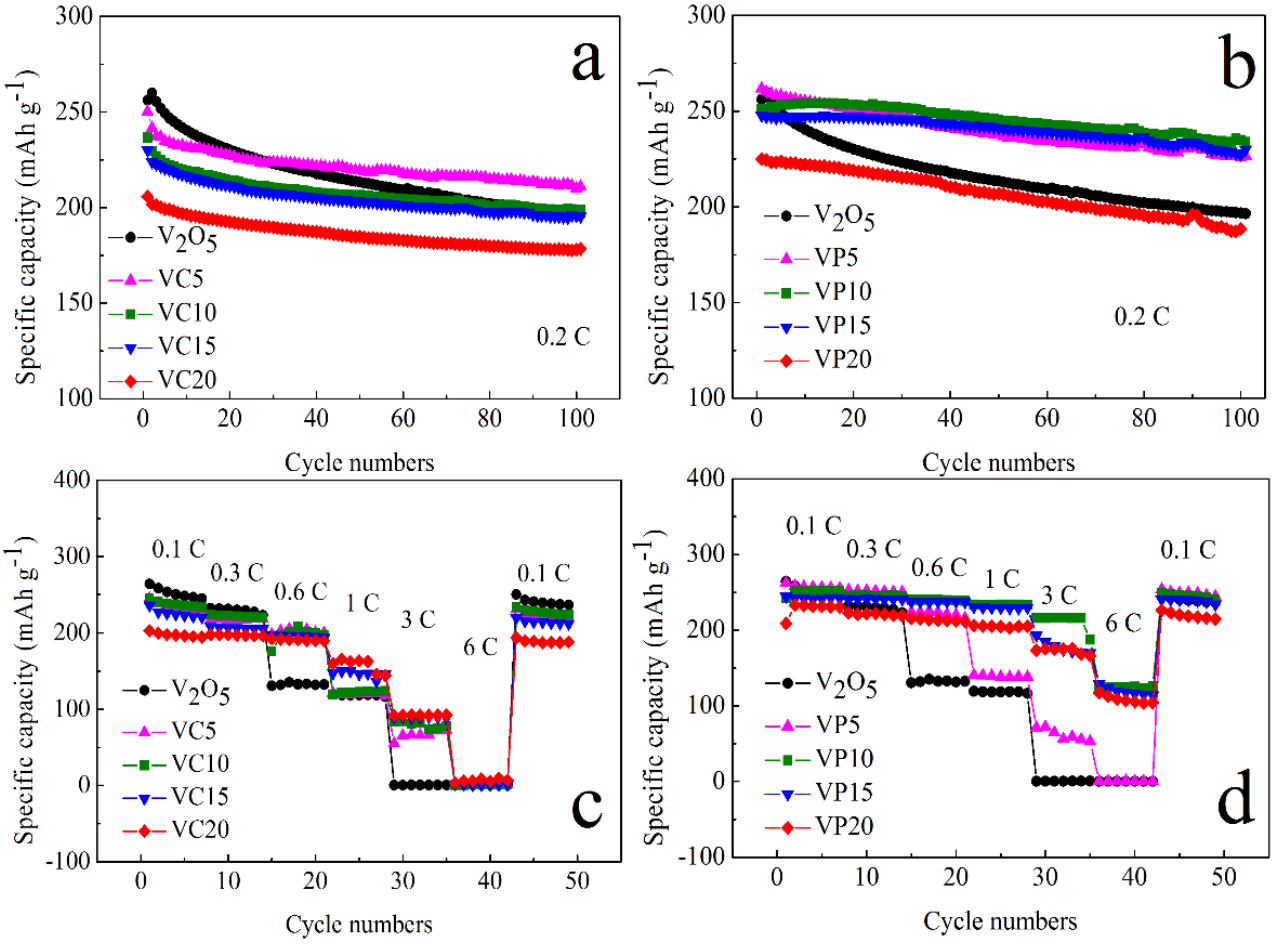

Figure 5.8 Cycling performance of a) VC and b) VP samples at 0.2C between 2.0 and 4.0 V. Comparison of rate capabilities of c) VC samples with V_2O_5 and d) VP samples with V_2O_5 at various current rates.

Figure 5.8a-b show the cycling performance of VC and VP samples measured at 0.2C between 2.0 and 4.0 V. The commercial V_2O_5 possessed an initial capacity of 256 mAh g^{-1}, and a capacity of 197 mAh g^{-1} at the 100th cycle. The capacity retention was 77% in 100 cycles, corresponding to an average capacity fading of 0.23 % per cycle. The cycling stability of V_2O_5 was enhanced by adding MWCNTs as conductive additives. VC5 had the initial capacity of 250 mAh g^{-1} and the 100th cycle capacity of 210 mAh g^{-1}, leading to the capacity retention of 84% after 100 cycles. The initial specific capacity of VC5 was slightly lower than that of pure V_2O_5, which is due to the reduced content of V_2O_5 active material.[242] The capacity retention of MWCNT-modified samples (VC) kept rising with higher amount of MWCNTs, up to 86.4% for VC20. As for the PEDOT-modified V_2O_5 samples (VP), the cycling performance showed dramatic improvements in contrast with that of V_2O_5. With 5 wt% of PEDOT, the capacity retention of VP5 was promoted to 86.3 %

for 100 cycles with the initial capacity of 262 mAh g^{-1}. The VP10 sample achieved the best cycling performance by having 251 mAh g^{-1} for the 1st cycle and the capacity of 235 mAh g^{-1} for the 100th cycle, which led to the excellent capacity retention of 94% for 100 cycles. The PEDOT-modified samples in present work showed a better cycling stability, in comparison with the reported V_2O_5/PEDOT nanowires that had 175 mAh g^{-1} for the 1st cycle and 116 mAh g^{-1} for the 40th cycle.[231]

The rate performances of VC and VP samples were shown in Figure 5.8c-d. The commercial V_2O_5 exhibited quick capacity fading as current density increases. The capacity of V_2O_5 only remained (132 mAh g^{-1}) half of the initial at 0.6C, and quickly dropped to 0 mAh g^{-1} at 3C with no discharging. The absence of discharging meant that the battery voltage dropped below the cut-off voltage (2 V), as the internal polarization resistance was too high at a high current density.[228] In comparison, the specific capacities of the VC samples increased with higher content of MWCNTs at large current densities between 1C and 3C. The VC5, VC10, VC15, and VC20 samples showed the capacities of 67, 81, 89, 93 mAh g^{-1} at 3C, respectively. The values were comparable to previously reported work.[242,243] The VC samples began to show almost no capacity at the high currents of 6C due to large polarization. But when the current density was set back to 0.1C, great capacity reversibility was achieved. For example, VC5 still got a high reversible capacity of 225 mAh g^{-1} when the current was reduced back to 0.1C after 6C.

Modification with PEDOT significantly improved the rate performance (Fig. 8d), especially at high current densities. VP5, VP10, VP15, and VP20 displayed specific capacities of 65, 217, 179, 175 mAh g^{-1} at 3C, and specific capacities of 0, 125, 119, 109 mAh g^{-1} at 6C, respectively. Among the samples modified with PEDOT, VP10 displayed the best rate performance. The specific capacities of VP10 were 252, 246, 240, 234, 217, 125 mAh g^{-1} at current densities of 0.1C, 0.3C, 0.6C, 1C, 3C, and 6C, respectively. The rate capability of VP10 is better than that of the reported V_2O_5/PEDOT nanowires.[231]

Figure 5.9 compares the battery performance of composites with different additives. VC5, VP10, and VC5P10 showed excellent electrochemical properties in their individual category. It can be seen from Fig. 9a that VP10 was the most stable sample against cycling at 0.2C with a capacity loss of 94% in 100 cycles. The rate capability of VP10 was also the best amongst. Therefore, the VP10 sample is the optimal material in terms of both cycling and rate performance.

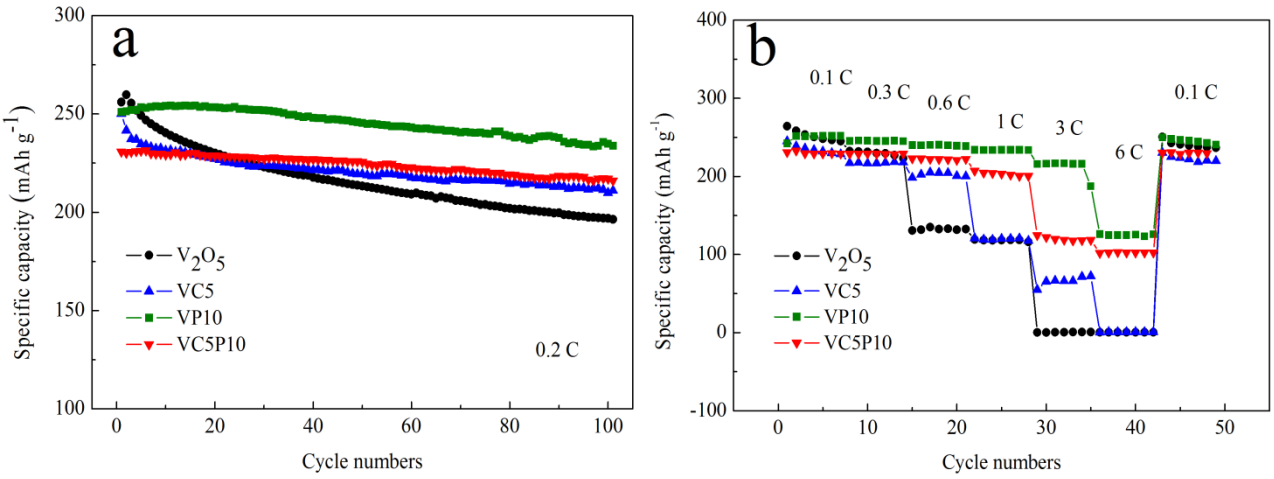

Figure 5.9 a) Cycling and b) rate performances of V_2O_5, VC5, VP10, and VC5P10 between 2.0 and 4.0 V.

Figure 5.10 displayed the discharge-charge curves of VP10 at 0.2C between 2.0 and 4.0 V. In the first cycle, VP10 showed a discharge capacity of 251 mAh g^{-1} and a charge capacity of 252 mAh g^{-1}, showing the first-cycle coulombic efficiency was 100%. Three consecutive plateaus in the first discharge were observed at 3.37 V, 3.19 V, and 2.33 V, corresponding to the formation of ε-$Li_{0.5}V_2O_5$, δ-LiV_2O_5, and γ-$Li_2V_2O_5$ phases in the lithium intercalation process. In the subsequent charge processes, lithium de-intercalation was reversible. The charge-discharge profiles at different cycles were overlapped, indicating excellent electrochemical reversibility.

The surface modification of V_2O_5 with the conducting polymer PEDOT significantly improved the battery performance of the commercial V_2O_5. PEDOT was formed as the protective layer on the V_2O_5 surface, which not only enhanced the stability of V_2O_5 against electrolyte, but also improved the electric conductivity of the PEDOT-modified V_2O_5. A PEDOT-modified sample with 10 wt% of PEDOT exhibited the best performance, showing the importance of controlling the mass of conducting polymer in modifying V_2O_5.

For the MWCNT-modified samples, MWCNTs improved the cycling performance and high-rate capability of V_2O_5. But the improvements were not as large as those of the PEDOT-modified samples. On the one hand, the conductivity of MWCNT-modified samples was lower than that of the PEDOT-modified samples. On the other hand, MWCNTs didn't contribute to the stability of V_2O_5 against electrolyte, different from PEDOT. Therefore, the

samples modified with both PEDOT and MWCNTs showed intermediate battery performance between those of the PEDOT-modified samples and those of the MWCNT-modified samples.

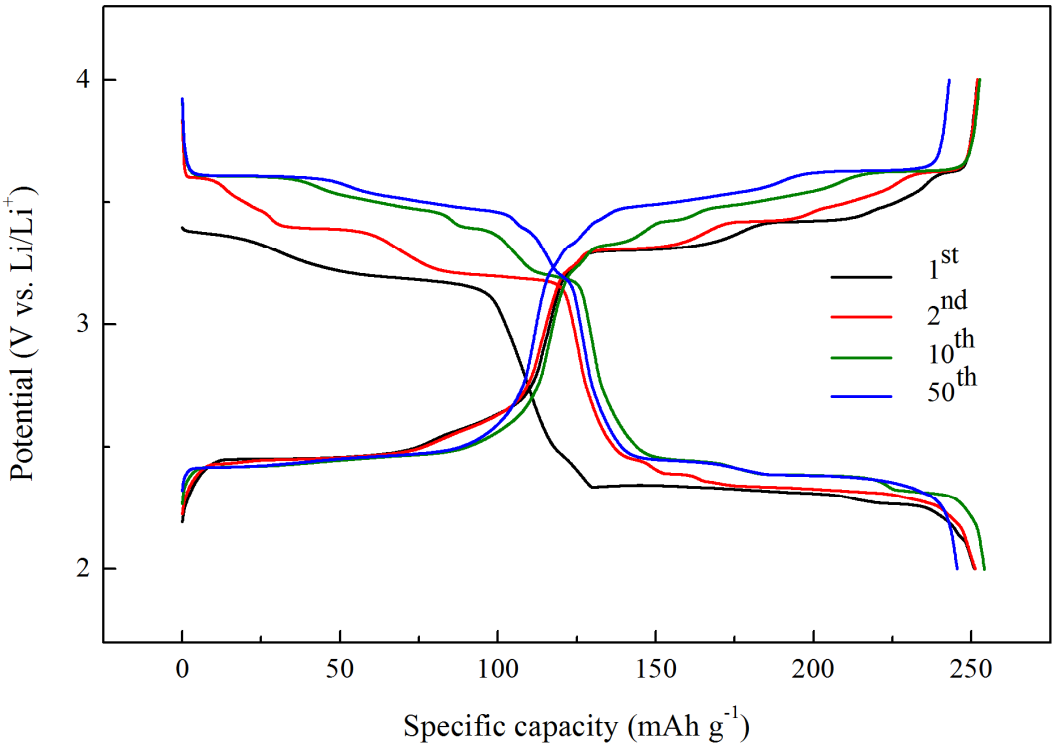

Figure 5.10 Discharge-charge voltage profiles of VP10 at 0.2C between 2.0 and 4.0 V.

5.4 Conclusions

In summary, modification of commercial V_2O_5 with PEDOT and MWCNTs can improve its electrochemical properties as a lithium-ion battery cathode. The orthorhombic structure of V_2O_5 was not affected upon modification with both components. However, PEDOT caused reduction of the majority of V^{5+} to V^{4+} and V^{3+}. With regard to contribution for battery performance, MWCNTs improved the electric conductivity of the modified V_2O_5, while PEDOT not only improved the electric conductivity but also enhanced the stability of V_2O_5 against electrolyte. The battery performance of the modified samples followed the order of PEDOT-modified V_2O_5, MWCNTs and PEDOT modified V_2O_5, and MWCNTs-modified V_2O_5. The V_2O_5 modified with 10 wt% of PEDOT exhibited the best electrochemical properties, by having excellent capacity retention of 94 % over 100 cycles and a high discharge capacity of 125 $mAhg^{-1}$ at 6C.

6 Single-crystalline orthorhombic copper vanadate nanobelts as cathode material for lithium-ion batteries

6.1 Introduction

Nanostructured V_2O_5 materials have been extensively studied to compensate the intrinsic weakness of V_2O_5. [104,106,132,142,244,245] Porous nanoscale structures can shorten Li^+ diffusion length, enhance the contact area between V_2O_5 and electrolyte, and accommodate the strain of Li^+ intercalation/deintercalation. Liu *et al.* synthesized V_2O_5 nanowire/graphene composite that exhibited high initial discharge capacities and exceptional rate capacities.[106] Zhu *et al.* reported that ultrathin V_2O_5 nanosheets with porous architecture achieved the capacitance retention of 90% after 4000 cycles for supercapacitors, and showed outstanding energy and power densities five times higher than commercial supercapacitors.[246] Moreover, robust three-dimensional (3D) hierarchical microstructures were self-assembled by nanoscale V_2O_5 building blocks.[122,141,144] These 3D hierarchical microstructures not only effectively suppress aggregation, but also have robust framework to buffer large volume changes during cycling. Mai *et al.* found that nanoflakes-assembled 3D hollow-porous V_2O_5 quasi-microspheres could show prominent capacity retention of 0.11% per cycle at high current rate of 1 A g^{-1} in 200 cycles.[144]

The electrochemical performance of V_2O_5 also can be improved by enhancing its inherent electrical conductivity with doping of transition metal cations, such as silver,[170] copper,[247] platinum,[248] aluminum,[249] Tin,[250] etc. Cation doping is able to turn V_2O_5 into mixed-valence vanadium oxide by generating a few V^{4+} ions, which leads to higher electrical conductivities.[241] Furthermore, the presence of doped cations within the slabs of V_2O_5 could increase the structural stability of V_2O_5, resulting in better cycling performance.[251]

Poor cycling stability is still a common difficulty for the nanostructured V_2O_5 materials, due to insufficient electric conductivity.[106,120] Integrating nanostructures with cation doping is expected to be an excellent strategy to prepare high-performance cathode materials for LIBs. In this chapter, the V_2O_5 nanobelts with copper doping were synthesized by a facile hydrothermal treatment method. The single phase Cu-doped V_2O_5 nanobelts were obtained with up to 4% of copper. Both the V_2O_5 and $Cu_{0.04}V_2O_5$ nanobelts were highly interconnected to form web networks. The width of the $Cu_{0.04}V_2O_5$ nanobelts was smaller than that of the V_2O_5 nanobelts. To investigate the formation mechanism of the V_2O_5 nanobelts, a series of samples were prepared with different reaction times. The XPS spectra confirmed the mixed valences of Cu and V elements in the $Cu_{0.04}V_2O_5$, favorable for better electric conductivity. When applied as the cathode material for LIBs, the $Cu_{0.04}V_2O_5$ nanobelts showed better cycling and rate performance than that of V_2O_5 nanobelts.

6.2 Experimental

In a typical synthesis of V_2O_5 nanobelts, 0.485 g of commercial V_2O_5 powder, 6.67 mL of 30% H_2O_2, and 40 mL of H_2O were mixed and kept stirring for 20 mins. The resulting transparent orange solution had vigorous bubbles by releasing oxygen gas. 37 mL of the mixture was then sealed into a 50 mL Teflon autoclave, and kept in oven at 190 °C for 30 h. In order to study the structural evolution process, hydrothermal treatments were also carried out at 190 °C for 10, 15, 20, and 25h. As for preparing single phase copper-doped V_2O_5 nanobelts, pluronic P123 and $Cu(NO_3)_2{\cdot}3H_2O$ were used as reducing agent and copper source, respectively. Appropriate amounts of P123 and $Cu(NO_3)_2{\cdot}3H_2O$ were added into the above-mentioned solution of V_2O_5 and H_2O_2, while keeping other parameters unaltered. The products were washed with distilled water several times. Finally, the precipitates were dried at 80 °C in vacuum for 12 h and then annealed at 400 °C for 1 h in air.

In order to check sample crystallinity, XRD measurements were performed on a Shimadzu diffractometer (XRD–6000, Tokyo, Japan) with Cu Kα radiation at a step size of 0.01º per second. The sample morphologies were investigated by using a scanning electron microscopy (JEOL, Model JSM-6460). Interior structures and element mapping were examined by a transmission electron microscopy (JEOL, Model JEM-2100) equipped with an energy-dispersive x-ray (EDX) analyzer. X-ray photoelectron spectroscopy (XPS)

spectra were measured to verify the valence state of vanadium and copper by a Kratos Axis ULTRA X-ray photoelectron spectrometer with a 165 mm hemispherical electron energy analyzer and monochromatic Al Kα (1486.6 eV) radiation at 225 W (15 kV, 15 mA). Nitrogen adsorption-desorption isotherms were measured at 77 K on Tristar II 3020. All samples were degassed at 120 °C for 12 h prior to the measurements. The specific surface area of samples was calculated using the Brunauer-Emmette-Teller (BET) method.

The cathodes were fabricated by mixing electroactive materials, carbon black and poly-vinylidene fluoride (PVDF) at a weight ratio of 70 : 20 : 10 in *N*-methyl-2-pyrrolidone (NMP) solvent. The resulting slurry was then pasted onto the aluminum foil and dried at 70 °C for 12 h. After that, the foil was punched into small disks with a diameter of 14 mm. The mass loading was around 1 mg. Metal lithium disks were used as anodes and the electrolyte solution was made up of 1.0 M $LiPF_6$ in ethylene carbonate (EC) and dimethyl carbonate (DMC) (1 : 1, w/w). The CR2025 coin-type cells were assembled in an argon-filled glove box, where both moisture and oxygen levels were less than 0.1 ppm.

The cells were charged and discharged over voltage ranges of 2.0–4.0 V (*vs.* Li/Li^+) at different current rates by using a Battery Testing System (Neware, China). Electrochemical impedance spectroscopy (EIS) and cyclic voltammetry (CV) were performed on a CHI 660b electrochemical workstation. CV was carried out at a scanning rate of 0.1 mV s^{-1} over the voltage range of 2.0–4.0 V. EIS measurements were performed over a frequency range of 100 kHz to 10 MHz with amplitude of 5 mV.

6.3 Results and discussion

Figure 6.1 compared the XRD patterns of both pure and Cu-doped V_2O_5 nano-belts annealed at 400 ℃ for 1 h. The Cu content was restricted to 4% to obtain single phase Cu-doped V_2O_5 nano-belts. In the XRD patterns of V_2O_5 and $Cu_{0.04}V_2O_5$, all the diffraction peaks can be indexed to the orthorhombic V_2O_5 phase (JCPDS card no. 72-0433, space group: *Pmnm (59), a = 11.51 Å, b = 4.369 Å, c= 3.563 Å*). No trace of impurity was detected, which indicates that V_2O_5 and $Cu_{0.04}V_2O_5$ were in single phase. The copper ions could be located between the V_2O_5 layers, which enhances the structural stability of the V_2O_5 lattice.[251]

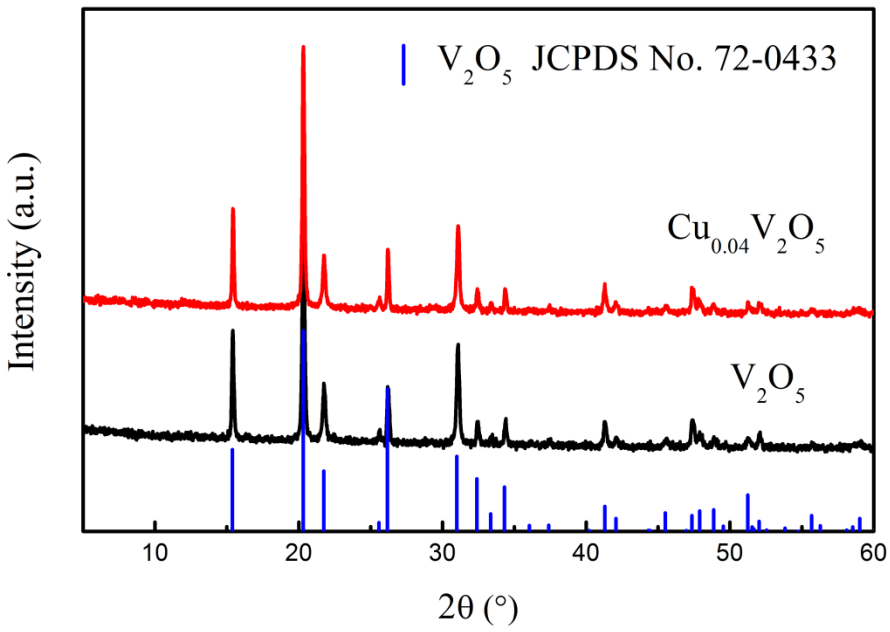

Figure 6.1 XRD patterns of V_2O_5 and $Cu_{0.04}V_2O_5$ nano-belts annealed at 400 ℃ for 1 h.

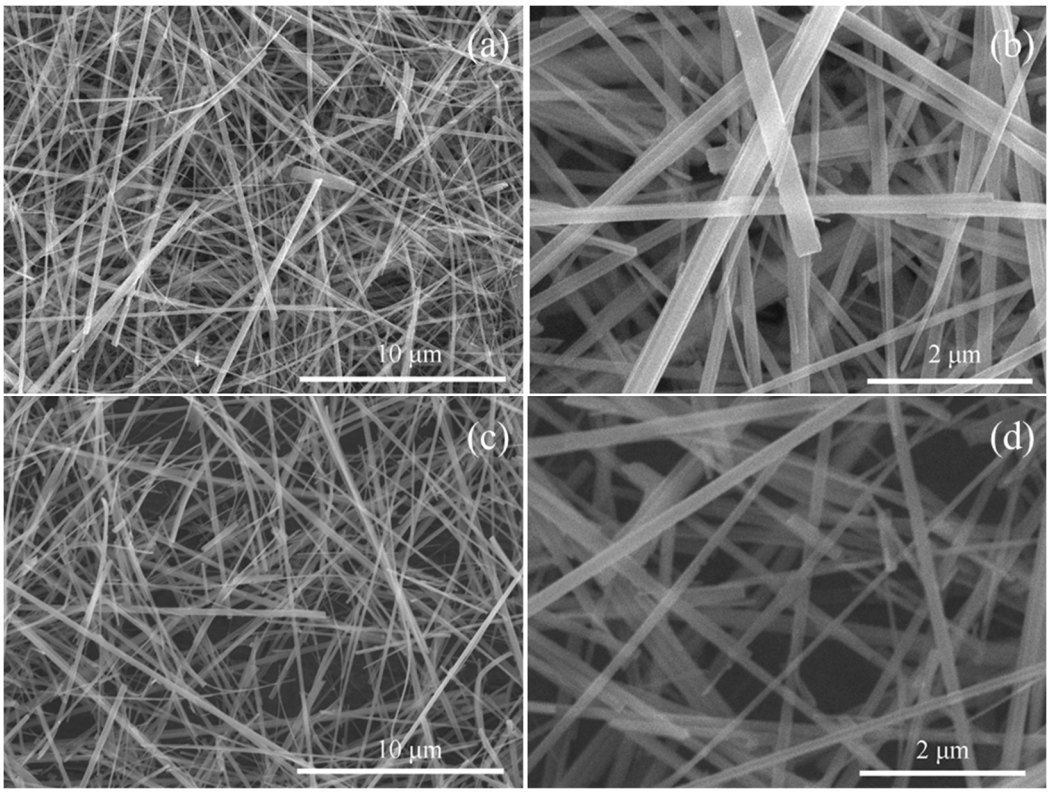

Figure 6.2 SEM images of (a-b) V_2O_5 and (c-d) the $Cu_{0.04}V_2O_5$ nanobelts.

Figure 6.2 shows the SEM images of V_2O_5 and $Cu_{0.04}V_2O_5$ nanobelts. Both samples exhibited uniform web networks composed of homogenous nanobelts. The highly

interconnected nanobelts were self-supporting so that they can effectively prevent agglomerates. In the high-magnification SEM images, the nanobelts showed high aspect ratios and clear rectangular cross-sections. The nanobelts of the two samples had similar lengths of up to tens of micro-meters. However, the V_2O_5 and $Cu_{0.04}V_2O_5$ nanobelts displayed some differences in widths. The widths of the V_2O_5 nanobelts were mainly between 100-300 nm, while the $Cu_{0.04}V_2O_5$ nanobelts showed the smaller widths of 70-250 nm. The web networks generated the voids between nanobelts, lead to porous structures. The nitrogen adsorption-desorption isotherms of the V_2O_5 and $Cu_{0.04}V_2O_5$ were demonstrated in Figure 6.3. The BET surface area of $Cu_{0.04}V_2O_5$ nanobelts is 10 m^2/g, larger than that of the pure V_2O_5 nanobelts.

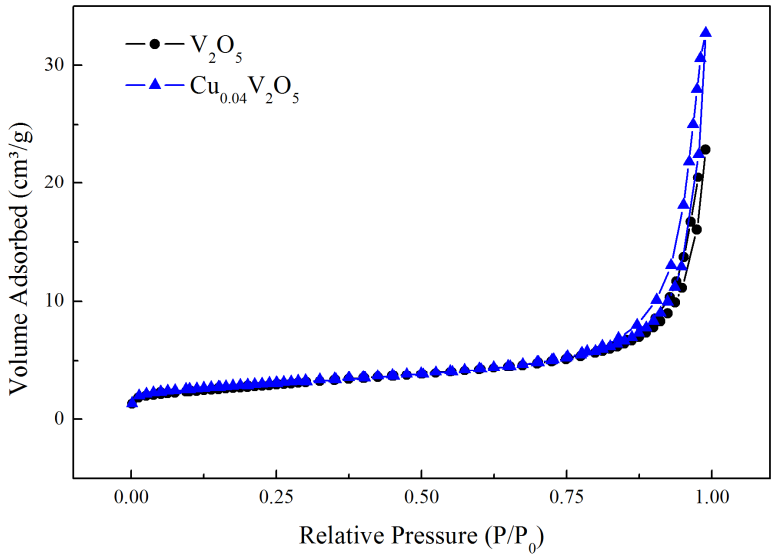

Figure 6.3 Nitrogen adsorption-desorption isotherms of the V_2O_5 and $Cu_{0.04}V_2O_5$.

The V_2O_5 and $Cu_{0.04}V_2O_5$ nanobelts were further investigated with TEM and HRTEM (Figure 6.4). The widths of the nanobelts were consistent with the observations in SEM images. The edges of carbon substrates underneath the nanobelts can be clearly seen, indicating the thicknesses of nanobelts were thin. Good crystallinity was confirmed by the lattice fringes in the HRTEM images of both V_2O_5 and $Cu_{0.04}V_2O_5$. These lattice fringes were assigned to the (200) planes of the orthorhombic V_2O_5 phase. As for the pure V_2O_5 nanobelts, the inter-planar spacing of the (200) planes was 5.791 nm. In comparison, the $Cu_{0.04}V_2O_5$ nanobelts have larger inter-planar spacing of 0.588 nm for the (200) planes, indicating the Cu doping extended the distances between the (200) planes. The EDX images of the $Cu_{0.04}V_2O_5$ nanobelts revealed that elements of vanadium, copper, and

oxygen are uniformly distributed along the nanobelt (Figure 6.5). Copper elements were evenly doped in the whole $Cu_{0.04}V_2O_5$ nanobelt.

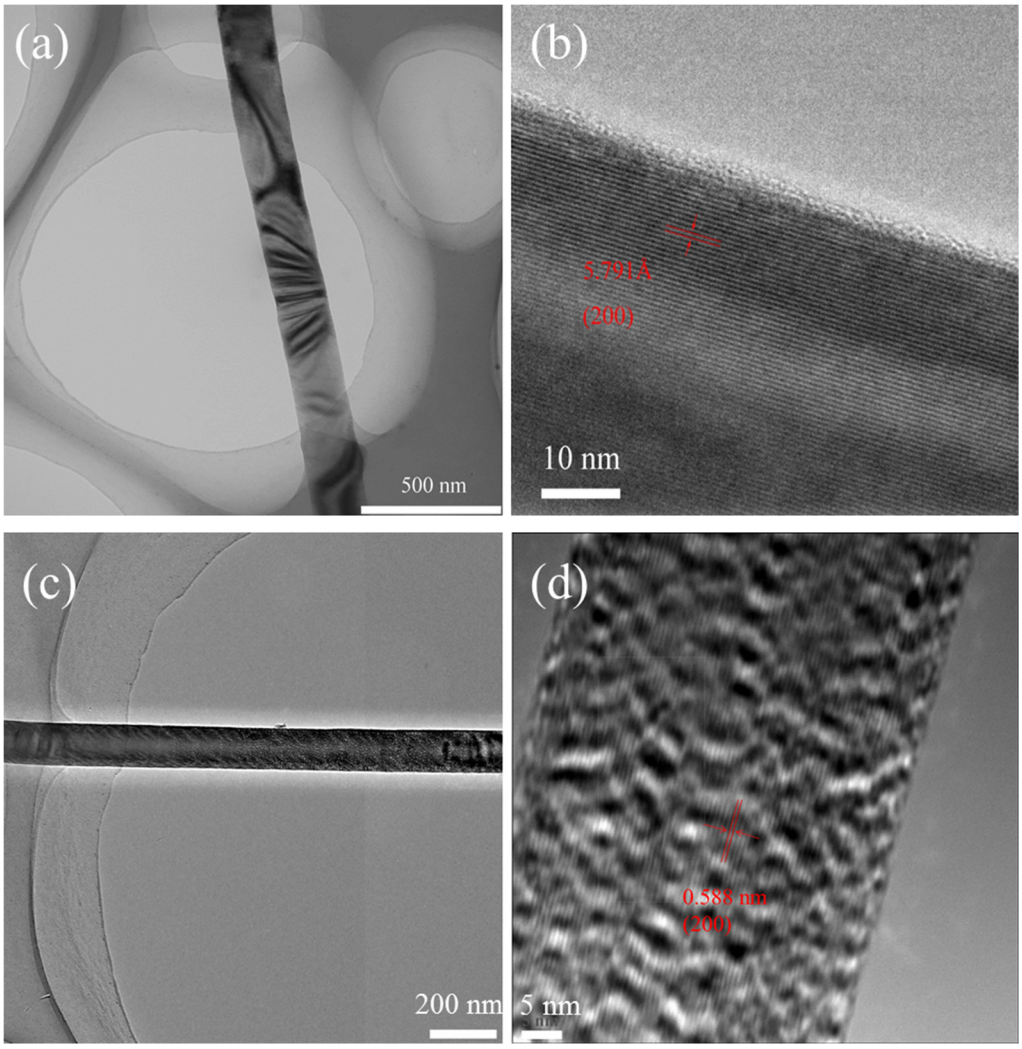

Figure 6.4 TEM (a) and HRTEM (b) images of the V_2O_5 nanobelts. TEM (c) and HRTEM (d) images of the $Cu_{0.04}V_2O_5$ nanobelts.

Figure 6.6 illustrated the high-resolution XPS spectra of Cu 2p and V 2p for the $Cu_{0.04}V_2O_5$ nanobelts. The two peaks in the V 2p spectrum were V $2p_{1/2}$ at low binding energy and V $2p_{3/2}$ at high binding energy. The Cu 2p spectrum exhibited three broad peaks from low to high binding energies, namely, Cu $2p_{1/2}$, satellite, and Cu $2p_{3/2}$. The satellite peak of Cu 2p is a typical character of Cu^{2+}. As both V 2p and Cu 2p showed far separation between $2p_{1/2}$ and $2p_{3/2}$ peaks, XPS fittings were conducted based on $2p_{3/2}$ peaks with higher intensities. As for the V $2p_{3/2}$, the peaks at 517.6 eV and 516.1 eV were assigned to V^{5+} $2p_{3/2}$ and V^{4+} $2p_{3/2}$.[252] The components of Cu $2p_{3/2}$ included Cu^{2+} $2p_{3/2}$ at 935.1 eV and Cu^{+} $2p_{3/2}$ at 932.2 eV. These values of binding energies are consistent with other

reports.[253] The results revealed that Cu^{2+} and V^{5+} elements were reduced to low valences in order to keep charge conservation. The oxide with mixed valences is favorable for higher electrical conductivity.[254] This sample was calculated to have 2.1 at. % of copper and 97.9 at.% of vanadium, consistent with the formula of $Cu_{0.04}V_2O_5$. P123 is employed as a reducing agent to partially reduce the valence of Cu^{2+} and V^{5+}, which can reduce charge imbalance and maintain pure phase.

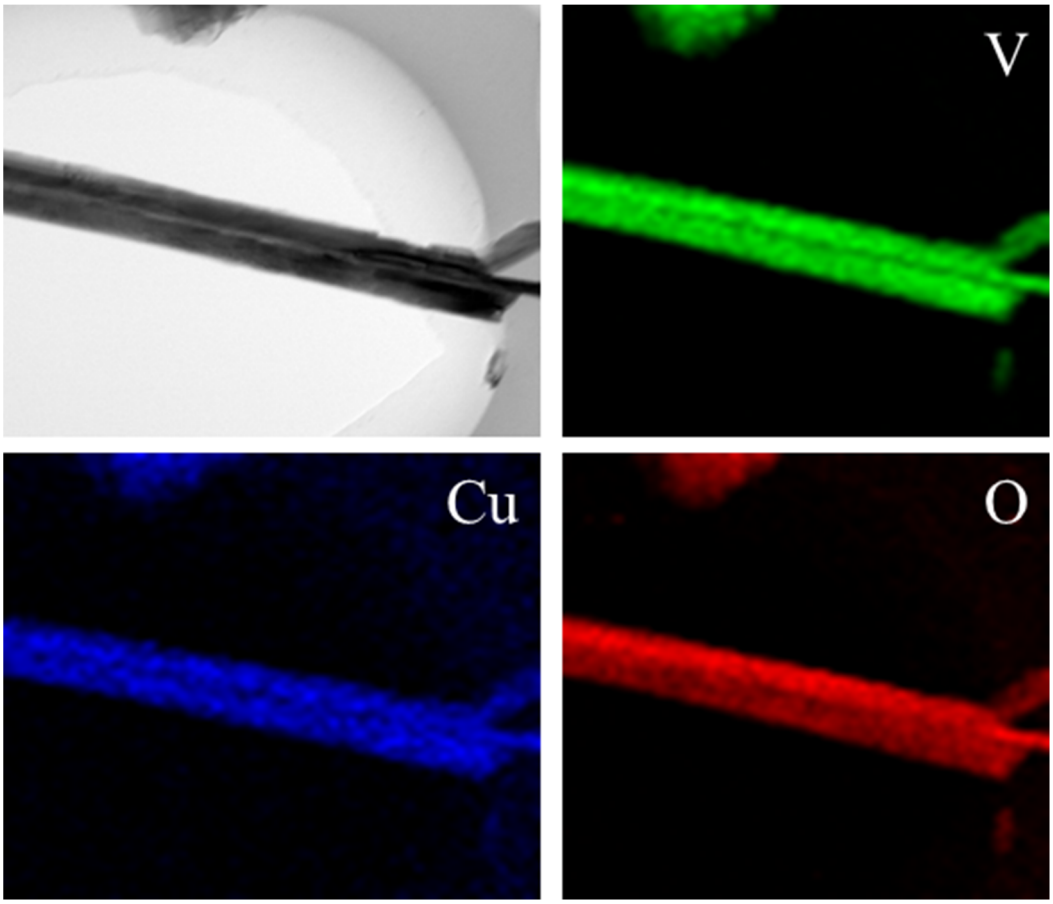

Figure 6.5 EDX mapping of the $Cu_{0.04}V_2O_5$ nanobelts.

To study the formation mechanism of single phase V_2O_5 nanobelts, time-dependent revolution of morphologies were investigated in Figure 6.7 and Figure 6.8. Small particles with diameter of 200-350 nm appeared uniformly after 10 h hydrothermal reaction. When the reaction time was extended to 15 h, the product exhibited inhomogeneous morphologies. Most of the sample was composed of the larger particles with sizes of around 0.5-1 μm. A small amount of large sheets were also formed in the 15 h sample. The large sheets showed around 10 square microns in sizes. When it reached 20 h, the morphology changed into uniform sheets with smaller sizes and thin thicknesses. These

thin sheets had about 70 nm in thicknesses and 4 microns in sizes. After 25 h, sheets trended to be split into belts, which had the widths of 0.4-1.2 μm. Notably, some belts were not completed stripped from their parent sheets, giving rise to a “tree-branch” structure. When the reaction time is further prolonged to 30 h, the final product was consisted of uniform nanobelts with high aspect ratios. The growth mechanism of nanobelts could be explained as following: V_2O_5 commercial powder was first dissolved in the solvent and grown into small particles. The sizes of the particles increase with longer reaction time. The particles are gradually assembled into large and thick sheets. However, these sheets go thinner and smaller with further reactions. The final step is splitting of sheets into belts, till the whole material is composed of uniform nanobelts with high aspect ratios. The splitting of sheets into belts are attributed to the cleavage planes of (001) and (100) in the orthorhombic V_2O_5 phase.[125]

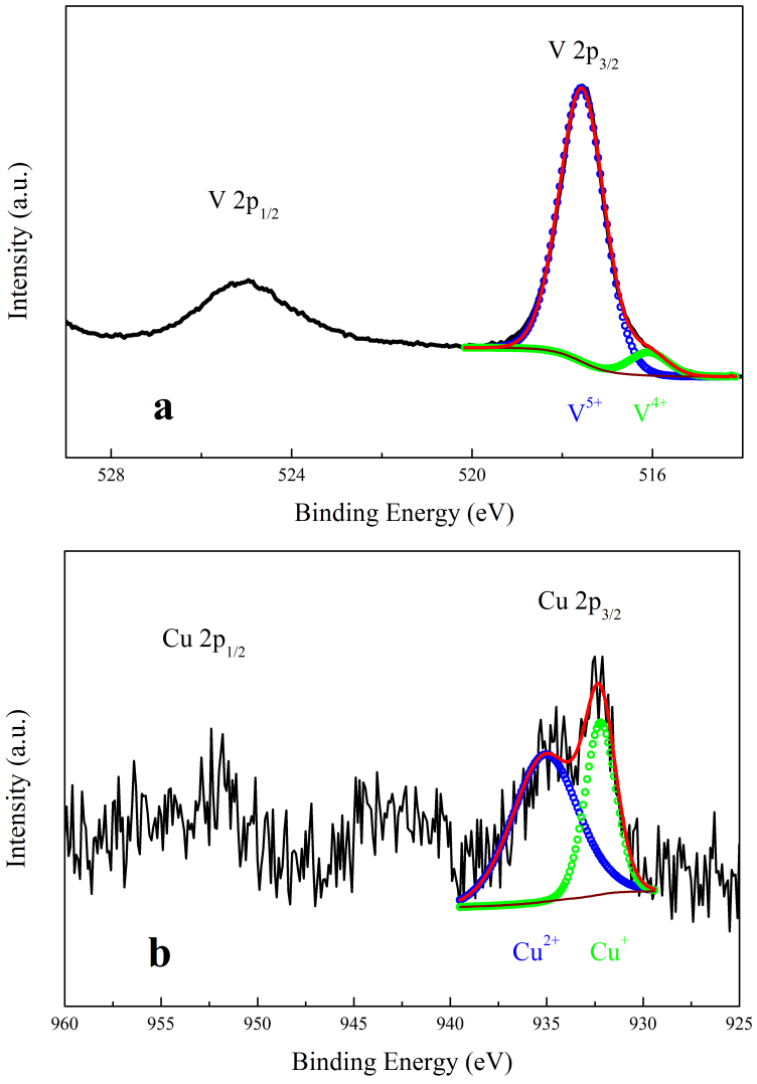

Figure 6.6 High-resolution XPS spectra of V 2p and Cu 2p for the $Cu_{0.04}V_2O_5$ nanobelts.

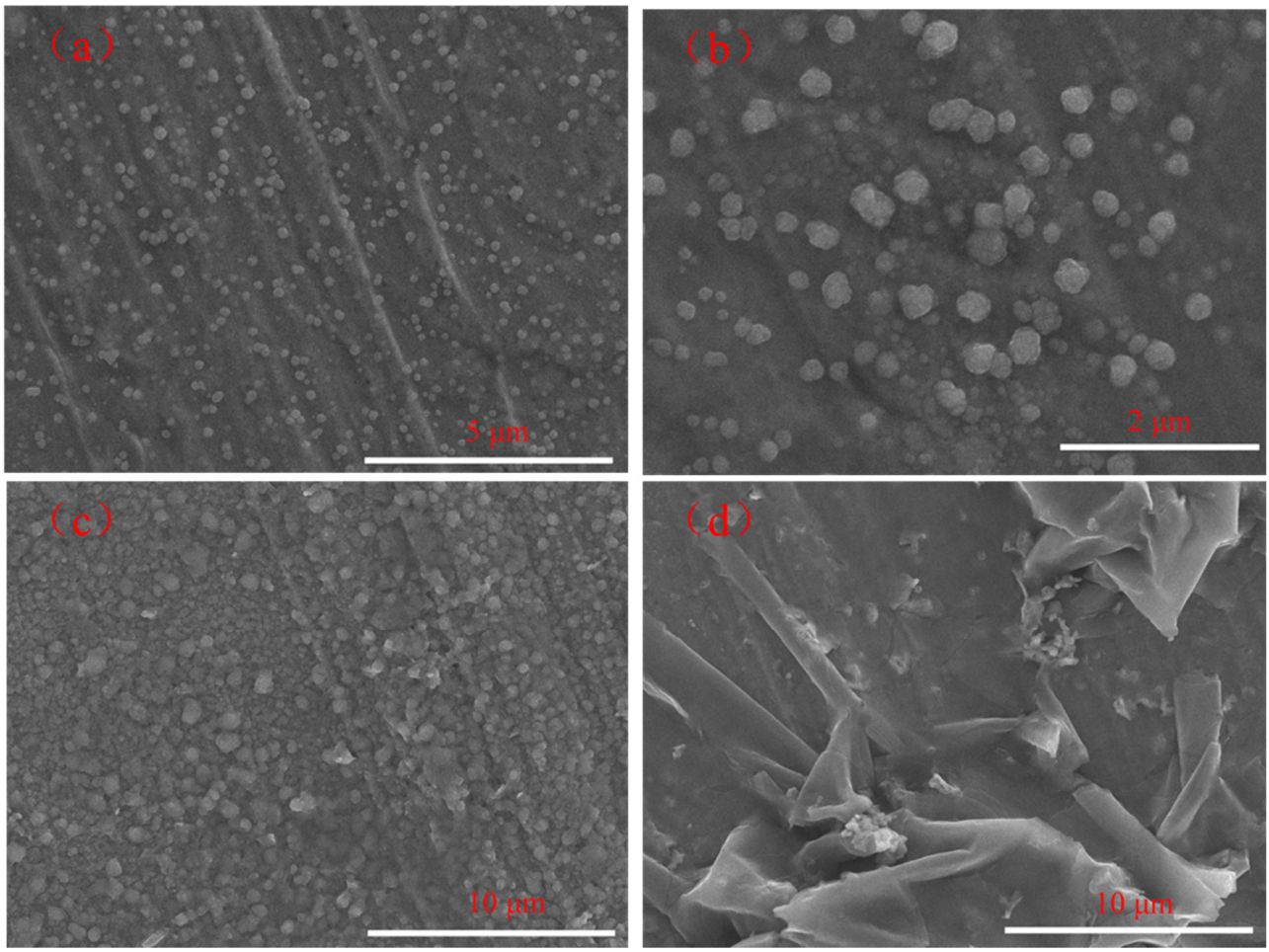

Figure 6.7 The SEM images of the products obtained with different hydrothermal reaction durations. (a-b) 10h, (c-d) 15 h.

Figure 6.9 shows cyclic voltammograms of the V_2O_5 nanobelts in the voltage range of 2.0-4.0 V. The CV curves exhibited paired redox peaks and stable profiles with discharge and charge. As for the 2nd cycle, the cathodic peaks at 3.38 V, 3.17 V, and 2.27 V are attributed to the formations of ε-$Li_{0.5}V_2O_5$, δ-LiV_2O_5, and γ-$Li_2V_2O_5$ phases by lithium intercalation, respectively. Three anodic peaks at 2.5 V, 3.32 V, and 3.5 V are associated with the Li^+ ion deintercalation processes back to δ-LiV_2O_5, ε-$Li_{0.5}V_2O_5$, and α-V_2O_5, respectively. The voltage differences between the redox peaks of the V_2O_5 nanobelts for the second cycle were much smaller than those for the first cycle, indicating the reduced polarization. Extra CV peaks appeared as shoulders after the first discharge. It might be related to the complex structural transitions that are induced by the formation of the irreversible γ-$Li_2V_2O_5$ phase in the first discharge.[151]

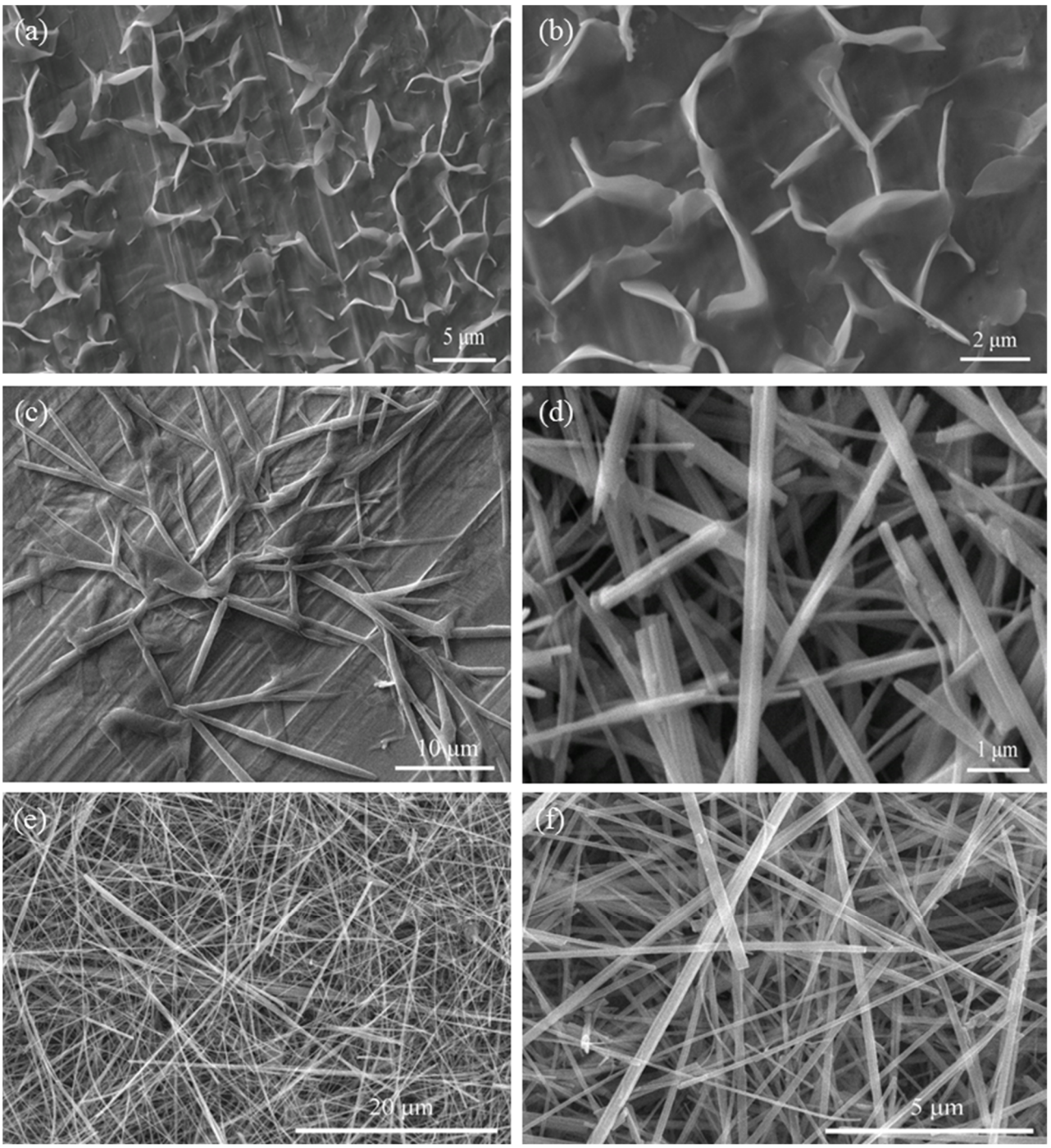

Figure 6.8 The SEM images of the products obtained at 190 ℃ for different hydrothermal reaction durations. (a-b) 20h, (c-d) 25 h, (e-f) 30 h.

Figure 6.10 presents cyclic voltammograms of the $Cu_{0.04}V_2O_5$ nanobelts in the voltage range of 2.0-4.0 V. In the 2nd cycle, the cathodic peaks at 3.36 V, 3.15 V, and 2.17 V corresponded to 0.5, 1, and 2 lithium insertions into the $Cu_{0.04}V_2O_5$ lattice. Three anodic peaks at 3.52 V, 3.33 V, and 2.55 V were related to the corresponding phase transitions in the process of lithium extraction. The peak current density of the $Cu_{0.04}V_2O_5$ nanobelts was

two times larger than that of the V_2O_5 nanobelts. It indicated the improved electric conductivity of the $Cu_{0.04}V_2O_5$ nanobelts.

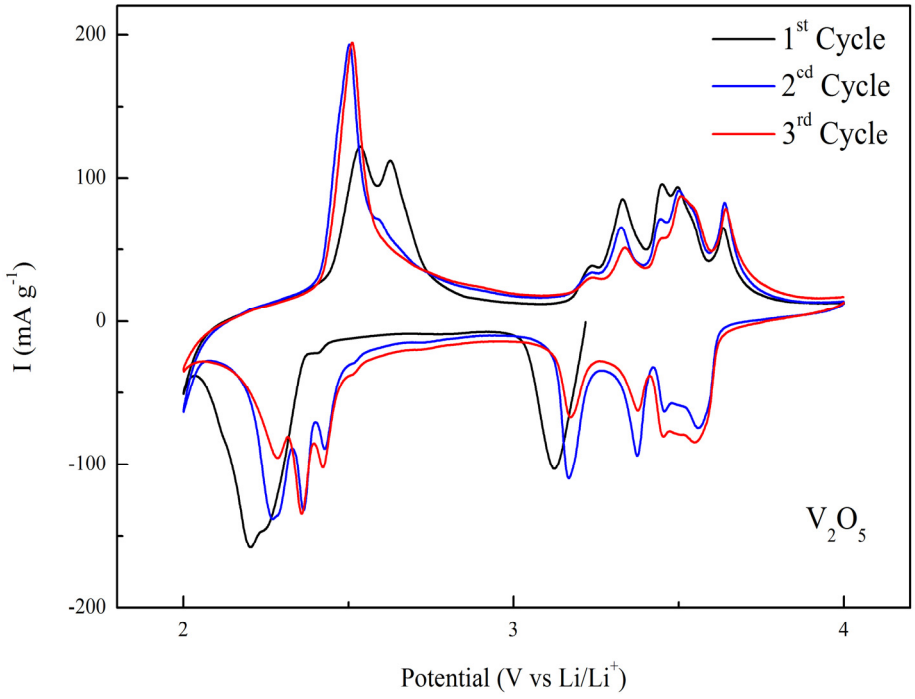

Figure 6.9 Cyclic voltammograms of the V_2O_5 nanobelts in the voltage range of 2.0-4.0 V.

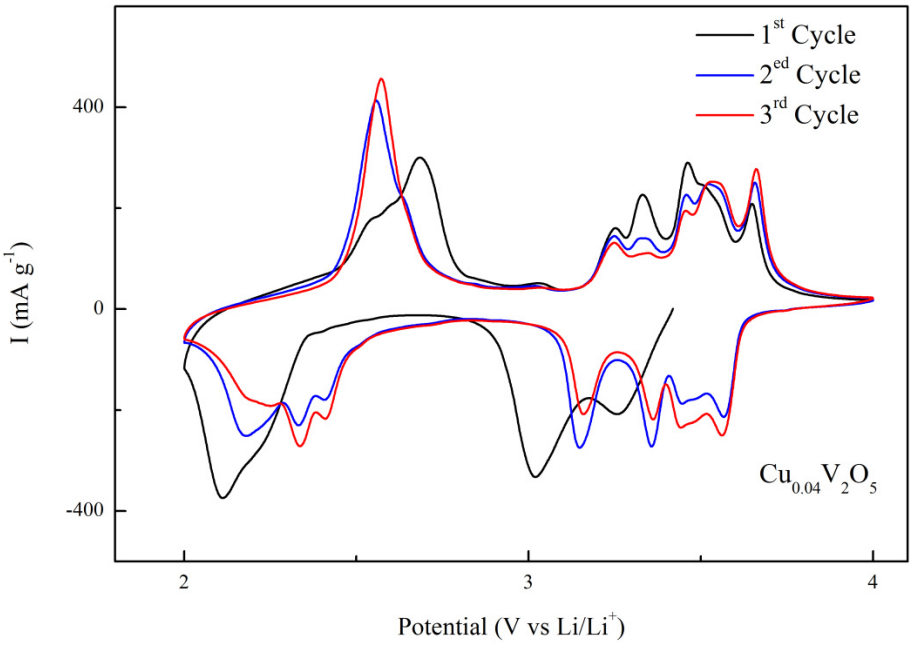

Figure 6.10 Cyclic voltammograms of the $Cu_{0.04}V_2O_5$ nanobelts in the voltage range of 2.0-4.0 V.

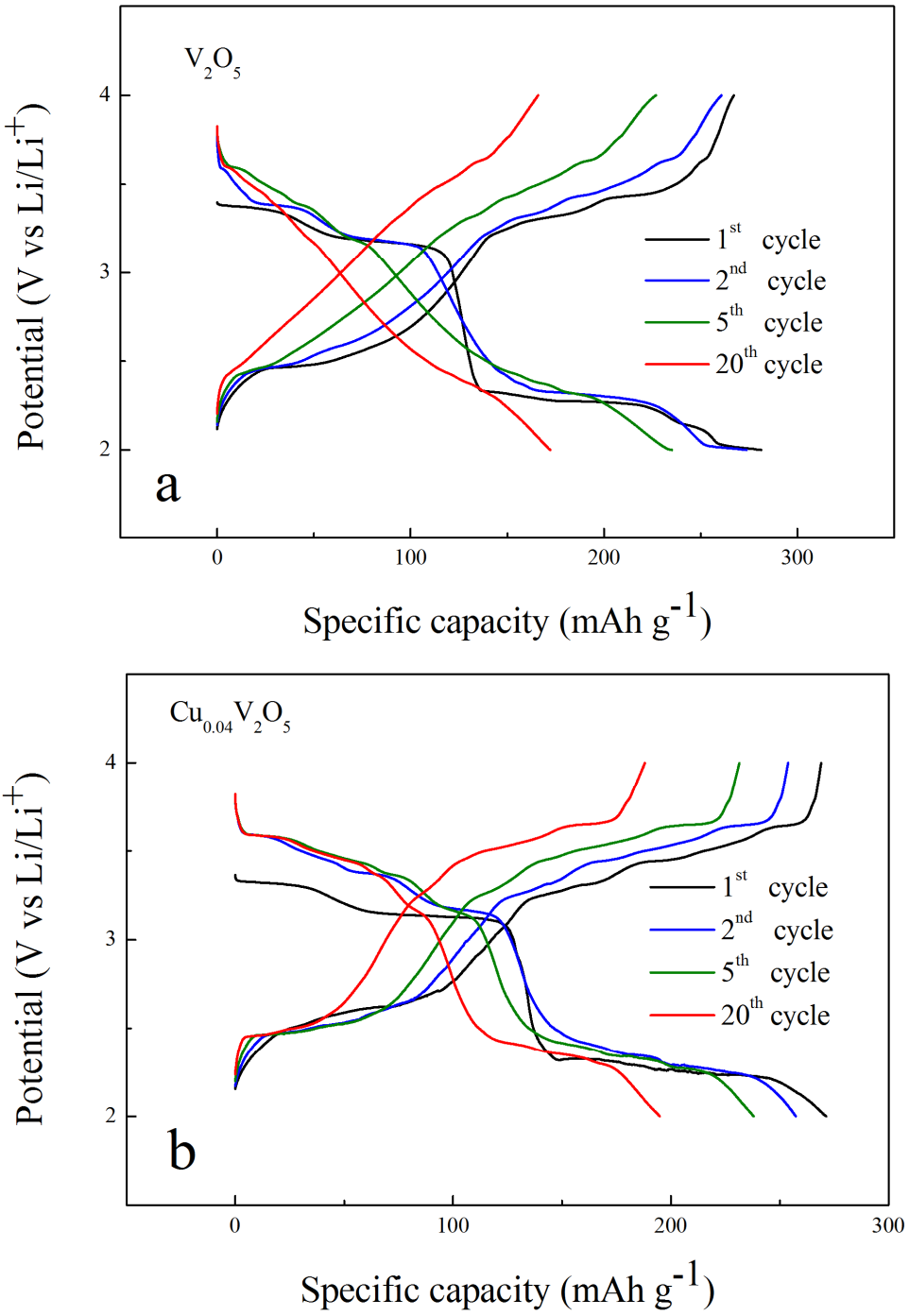

Figure 6.11 Galvanostatic charge–discharge curves of a) V_2O_5 nanobelts and b) $Cu_{0.04}V_2O_5$ nanobelts in the voltage range of 2.0-4.0 V.

The galvanostatic charge–discharge curves of V_2O_5 and $Cu_{0.04}V_2O_5$ nanobelts at 0.1 C were presented in Figure 6.11. Both samples showed distinct discharge-charge plateaus in the 1st cycle, well consistent with the redox peaks of the corresponding CV results. The charge-discharge profiles of V_2O_5 nanobelts turned into slopes after the 2nd cycle, as the

potential plateaus gradually disappeared. Noticeably, the charge-discharge plateaus of $Cu_{0.04}V_2O_5$ nanobelts remained stable in the first 20 cycles, in line with a previous report.[241] The existence of charge-discharge plateaus indicates good structural stability of an active material. Therefore, the $Cu_{0.04}V_2O_5$ nanobelts exhibited greatly improved structural stability during battery cycling. The $Cu_{0.04}V_2O_5$ nanobelts had the 1st discharge capacity of 272 mAh g^{-1} and 1st charge capacity of 270 mAh g^{-1}. The first cycle loss of the $Cu_{0.04}V_2O_5$ nanobelts is 2 mAh g^{-1}. In comparison, The V_2O_5 nanobelts had the 1st discharge capacity of 282 mAh g^{-1} and 1st charge capacity of 267 mAh g^{-1}, corresponding to the first cycle loss of 15 mAh g^{-1}. In addition, The $Cu_{0.04}V_2O_5$ nanobelts had a 20th discharge capacity of 195 mAh g^{-1}, about 71% of the initial capacity. The capacity retention of the V_2O_5 nanobelts was only 61% in the first 20 cycles. Obviously, the electrochemical reversibility of the $Cu_{0.04}V_2O_5$ nanobelts was much better.

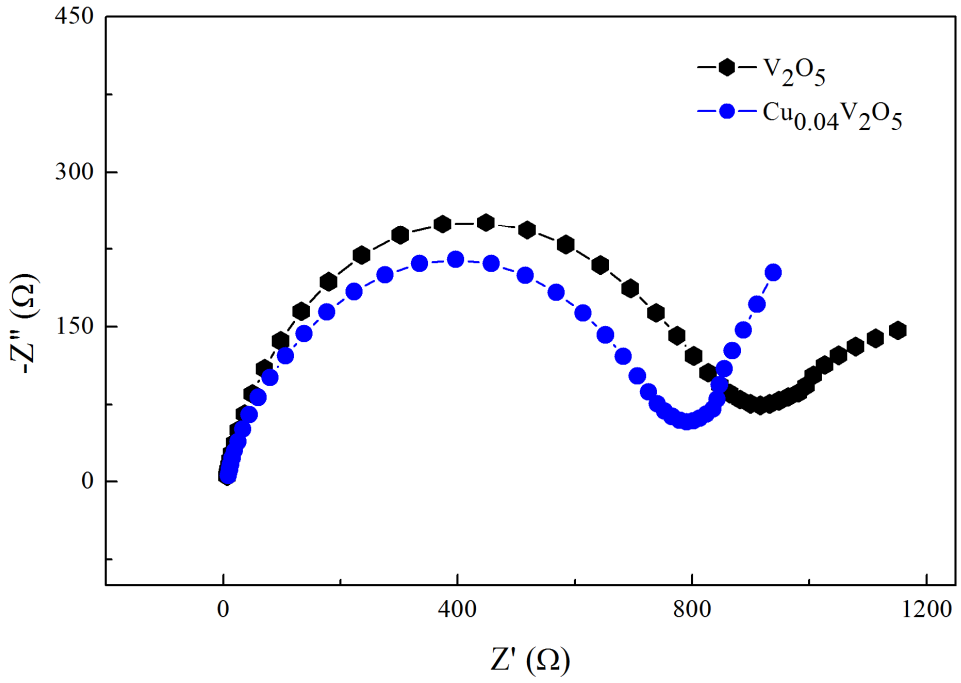

Figure 6.12 Electrochemical impedance spectra of the V_2O_5 and $Cu_{0.04}V_2O_5$ nanobelts measured from 100 kHz to 1 mHz with a voltage amplitude of 5 mV.

Figure 6.12 compared EIS of the V_2O_5 and $Cu_{0.04}V_2O_5$ nanobelts before cycling. All the spectra consist of a depressed semicircle in the high-to-medium frequency range and a linear tail with a phase angle of 45° in the low-frequency range. The intercept on the *Z'* axis stands for electrolyte resistance (R_s) at high frequencies. The semicircle is related to a charge-transfer process at the electrolyte/electrode interface, the diameter of which is

charge transfer resistances (R_{ct}). The linear region at low frequencies is associated with Warburg resistance (W) that represents the solid state diffusion of Li^+ ions through the V_2O_5 lattice. The semicircle diameter of V_2O_5 was larger than that of $Cu_{0.04}V_2O_5$. Therefore, $Cu_{0.04}V_2O_5$ has the smaller charge-transfer resistance and better electric conductivity, in agreement with the CV curves. The increased electric conductivity of the $Cu_{0.04}V_2O_5$ nanobelts is favorable to improve the cycling and rate performance.

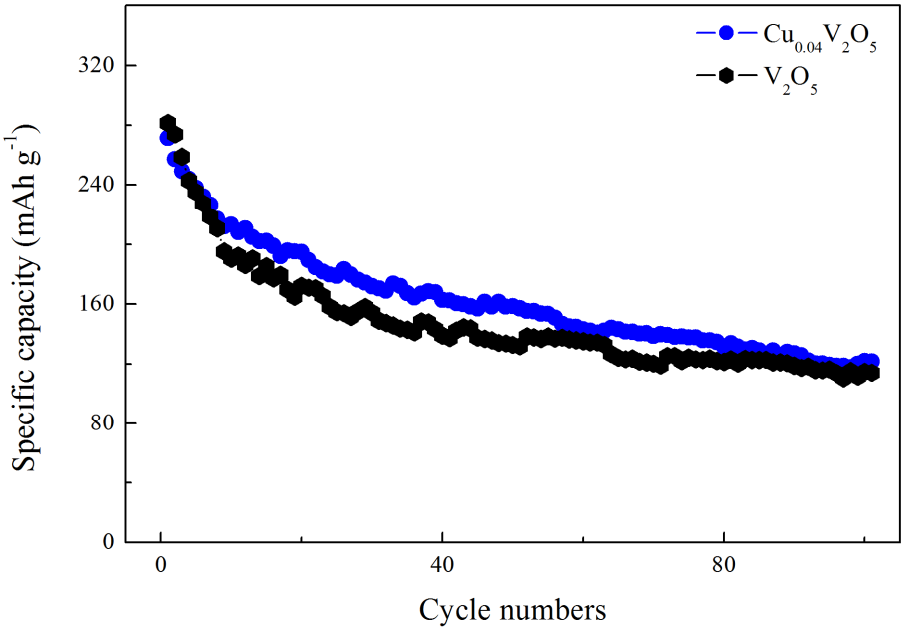

Figure 6.13 Cycling performance of the V_2O_5 and $Cu_{0.04}V_2O_5$ nanobelts at a current density of 0.1C in the voltage range of 2.0-4.0 V.

Figure 6.13 compared cycling performance of the V_2O_5 and $Cu_{0.04}V_2O_5$ nanobelts at a current density of 0.1C in the voltage range of 2.0-4.0 V. The quick capacity fading in the first 10 cycles was attributed to the SEI formation and irreversible structural transitions.[227] The $Cu_{0.04}V_2O_5$ nanobelts had the first discharge capacity of 271 mAh g^{-1} and 100th discharge capacity of 122 mAh g^{-1}. The V_2O_5 nanobelts had the first discharge capacity of 281 mAh g^{-1} and 100th discharge capacity of 99 mAh g^{-1}. The $Cu_{0.04}V_2O_5$ nanobelts showed better cycling stability with the capacity retention of 45%, higher than the value of 35% for V_2O_5 nanobelts.

The rate performance of both samples was also evaluated in the voltage range of 2.0-4.0 V (Figure 6.14). The $Cu_{0.04}V_2O_5$ nanobelts demonstrated a much better rate capability than that of the V_2O_5 nanobelts. The $Cu_{0.04}V_2O_5$ nanobelts delivered specific discharge

capacities of 258, 196, 175, 147, 104, and 68 mAh g^{-1} at 0.1C, 0.3C, 0.6C, 1C, 3C, and 6C, respectively. The specific discharge capacities of the V_2O_5 nanobelts were 244, 183, 141, 127, 67, and 19 mAh g^{-1} at 0.1C, 0.3C, 0.6C, 1C, 3C, and 6C, respectively. At the high current density of 6C, the $Cu_{0.04}V_2O_5$ nanobelts kept the 26 % of the initial capacity, while the V_2O_5 nanobelts only retained a much lower value of 8%. When the current rate jumped from 6C back to 0.1C, both of the samples recovered over 80 % of the initial capacities, indicating good electrochemical reversibility.

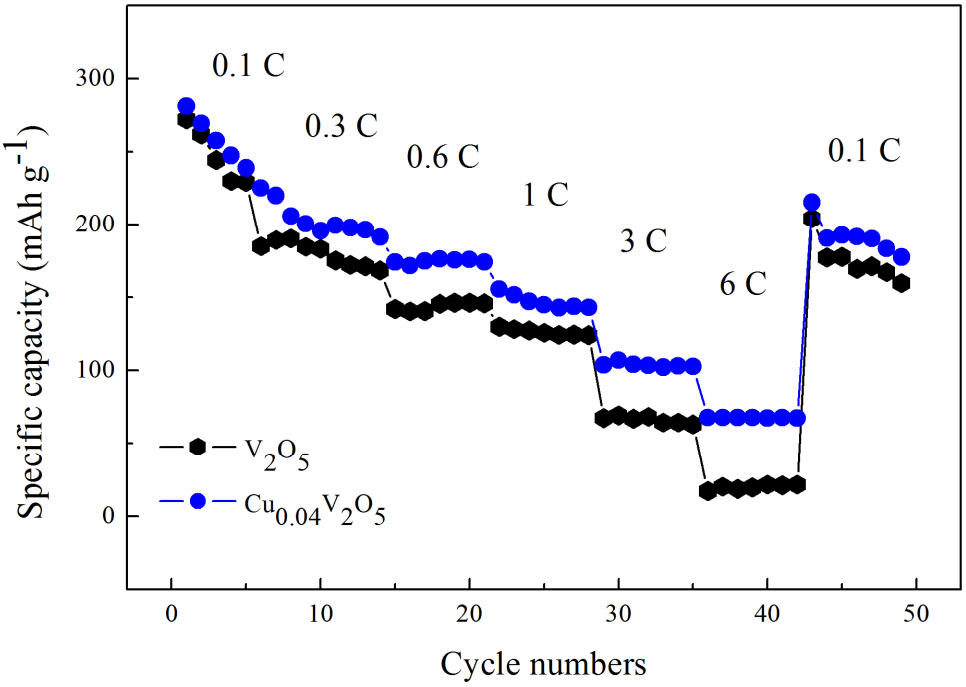

Figure 6.14 Rate performance of the V_2O_5 and $Cu_{0.04}V_2O_5$ nanobelts in the voltage range of 2.0-4.0 V.

The $Cu_{0.04}V_2O_5$ nanobelts exhibited great improvements in both cycling stability and rate performance, compared to the V_2O_5 nanobelts. The improvements of battery performance were closely associated with nanobelt structures and Cu doping. First, the smaller widths of $Cu_{0.04}V_2O_5$ nanobelts shorten the diffusion path of Li+ ions. Second, copper doping effectively enhances the electric conductivity of the $Cu_{0.04}V_2O_5$ nanobelts. Third, the good structural stability of the $Cu_{0.04}V_2O_5$ nanobelts improves the electrochemical reversibility during cycling. The nanobelt structure integrated with Cu doping is an efficient strategy to enhance the electrochemical properties of the orthorhombic V_2O_5 material.

6.4 Conclusions

In summary, single-phase V_2O_5 and $Cu_{0.04}V_2O_5$ nanobelts were prepared by hydrothermal treatment method. The nanobelts with high aspect ratios were highly interconnected to form porous web networks. The $Cu_{0.04}V_2O_5$ nanobelts possess smaller widths, resulting in shorter diffusion length for lithium ions. Copper elements were evenly distributed in the $Cu_{0.04}V_2O_5$ nanobelts, leading to a better structural stability. In the $Cu_{0.04}V_2O_5$, both vanadium and copper had mixed valences, favorable for the better electric conductivity. When applied as cathodes for lithium ion batteries, the battery performance of $Cu_{0.04}V_2O_5$ was much better than that of V_2O_5 nanobelts. Within the first 100 cycles, the $Cu_{0.04}V_2O_5$ nanobelts achieved the capacity retention of 45%, which is higher than the value of 35% for V_2O_5 nanobelts. At the high current density of 6C, the $Cu_{0.04}V_2O_5$ nanobelts kept the 26 % of the initial capacity, while the V_2O_5 nanobelts only retained a much lower value of 8%. Both the cycling stability and rate performance of the $Cu_{0.04}V_2O_5$ nanobelts were enhanced due to the excellent contributions from the nanobelt structure and Cu doping.

7 Conclusions and Recommendations

This thesis focused on designing and preparing V_2O_5 based electrode materials with excellent cycling and rate performance for lithium ion batteries. Various approaches were employed to enhance the electric conductivity, structural stability, and electrochemical reversibility of the V_2O_5. Optimizing the electrode compositions and voltage windows is effective to reduce the electric resistance and the irreversible electrochemical loss of the V_2O_5 electrode. The combination of a conductive polymer and a carbonaceous material can produce an excellent conducting network on the surface of V_2O_5, and protect the active material against the electrolyte. The cation-doped V_2O_5 nanostructures efficiently shorten the diffusion length of lithium ions and increase the inherent electric conductivity. These strategies were promising in developing high-performance V_2O_5 cathodes for LIBs.

1. The electrochemical properties of the V_2O_5 electrode are sensitive to electrode compositions and voltage windows. Two electrodes with the different compositions of 7:2:1 and 8:1:1 were charged/discharged between 1.5 and 4 V. Due to the better electric conductivity, the 7:2:1 V_2O_5 electrode exhibited improvements in electrochemical reversibility, cycling stability, and rate performance. The voltage window was adjusted to further improve the battery performance of the 7:2:1 V_2O_5 electrode. The 7:2:1 V_2O_5 electrode achieved better electrochemical reversibility and cycling performance in a narrow voltage range of 2-4 V by excluding the irreversible ω-$Li_3V_2O_5$ phase. The average capacity fading of the 7:2:1 V_2O_5 electrode in the first 100 cycles is 0.23 % per cycle between 2-4 V, which is less than half of 0.53 % per cycle in the voltage range of 1.5-4 V.

2. V_2O_5 was co-modified with poly(3,4-ethylenedioxythiophene) (PEDOT) and multi-walled carbon nanotubes (MWCNTs) by using physical mixing and chemical oxidative polymerization methods. V_2O_5 particles were intermixed with MWCNTs, while PEDOT was coated on the surface of V_2O_5 particles. MWCNTs improved the electric conductivity of the modified V_2O_5, while PEDOT not only improved the electric conductivity but also enhanced the stability of V_2O_5 against electrolyte.

Among the samples with different contents of MWCNTs and PEDOT, the V_2O_5 modified with 10 wt% of PEDOT exhibited the best electrochemical properties, by having excellent capacity retention of 94 % over 100 cycles and a high discharge capacity of 125 $mAhg^{-1}$ at 6C. The battery performance of the modified samples followed the order of PEDOT-modified V_2O_5, MWCNTs and PEDOT modified V_2O_5, and MWCNTs-modified V_2O_5.

3. Single-phase V_2O_5 and $Cu_{0.04}V_2O_5$ nanobelts were prepared by hydrothermal treatment method. The nanobelts with high aspect ratios were highly interconnected to form porous web networks. The $Cu_{0.04}V_2O_5$ nanobelts exhibited great improvements in both cycling stability and rate performance, compared to the V_2O_5 nanobelts. Within the first 100 cycles, the $Cu_{0.04}V_2O_5$ nanobelts achieved the capacity retention of 45%, which is higher than the value of 35% for V_2O_5 nanobelts. At the high current density of 6C, the $Cu_{0.04}V_2O_5$ nanobelts kept the 26 % of the initial capacity, while the V_2O_5 nanobelts only retained a much lower value of 8%. The improvements of battery performance were closely associated with nanobelt structures and Cu doping. First, the smaller widths of $Cu_{0.04}V_2O_5$ nanobelts shorten the diffusion path of Li+ ions. Second, copper doping effectively enhances the electric conductivity of the $Cu_{0.04}V_2O_5$ nanobelts. Third, the good structural stability of the $Cu_{0.04}V_2O_5$ nanobelts improves the electrochemical reversibility during cycling.

Several recommendations can be given for future research based on the above discussions.

1. The conductive agents and binders are inactive materials in the electrode, reducing the gravimetric energy density of LIBs. Conductive binders are good candidates to further improve the gravimetric energy density of LIBs, which plays dual role as the electron conducting additive and binder. The electrodes fabricated with conductive binders are not only binder-free but also conductive agent-free.

2. The MWCNT-modified V_2O_5 by the physical mixing exhibited uneven distribution of MWCNTs in the composite material. One-dimensional V_2O_5 nanowires can be highly interconnected with MWCNTs by an in-situ hydrothermal method to produce

a uniform MWCNT/V_2O_5 composite. The robust and uniform V_2O_5/MWCNTs composites can be directly used as freestanding electrodes for LIBs.

3. The Cu-doped V_2O_5 nanobelts showed improved cycling and rate performance, but the content of copper need be very low to maintain the orthorhombic V_2O_5 phase, due to large differences in the valences of Cu and V ions. Other transition metals, such as Ti, can be used to further investigate the doping effects on the electrochemical properties of V_2O_5.

4. Low-dimensional V_2O_5 nanostructures commonly exhibits self-aggregation and low tap density. This issue can be improved by synthesizing hierarchical V_2O_5 microstructures which have advantages of both nano-sized primary particles and micron-sized secondary particles.

5. Combining 3D hierarchical V_2O_5 nanostructures with cation-doping or conductive surface modifications could be a promising strategy to develop outstanding V_2O_5 cathode materials with high energy and power densities. Long cycling life is also expected for these materials due to robust structural frames. The thin films produced by vacuum filtration can be used as flexible electrodes for LIBs.

8 List of References

[1] J.M. Tarascon and M. Armand, Nature **414**, 359 (2001).

[2] C. Liang, M. Gao, H. Pan, Y. Liu, and M. Yan, J. Alloys Compd. **575**, 246 (2013).

[3] P. Verma, P. Maire, and P. Novak, Electrochim. Acta **55**, 6332 (2010).

[4] D. Deng, Energy Science & Engineering **3**, 385 (2015).

[5] Nupur Nikkan Sinha and N. Munichandraiah, Journal of the Indian Institute of Science **89** (2009).

[6] M.S. Whittingham, Science **192**, 1126 (1976).

[7] J.O. Besenhard and G. Eichinger, Journal of Electroanalytical Chemistry and Interfacial Electrochemistry **68**, 1 (1976).

[8] B.M.L. Rao, R.W. Francis, and H.A. Christopher, J. Electrochem. Soc. **124**, 1490 (1977).

[9] D.W. Murphy and P.A. Christian, Science **205**, 651 (1979).

[10] D.W. Murphy, F.J. Di Salvo, J.N. Carides, and J.V. Waszczak, Mater. Res. Bull. **13**, 1395 (1978).

[11] M. Lazzari and B. Scrosati, J. Electrochem. Soc. **127**, 773 (1980).

[12] K. Mizushima, P.C. Jones, P.J. Wiseman, and J.B. Goodenough, Mater. Res. Bull. **15**, 783 (1980).

[13] M. Mohri, N. Yanagisawa, Y. Tajima *et al.*, J. Power Sources **26**, 545 (1989).

[14] T. Nagaura and K. Tozawa, Prog. Batteries Solar Cells **9**, 209 (1990).

[15] F. Orsini, A. Du Pasquier, B. Beaudoin, J.M. Tarascon, M. Trentin, N. Langenhuizen, E. De Beer, and P. Notten, J. Power Sources **76**, 19 (1998).

[16] M.M. Thackeray, W.I.F. David, P.G. Bruce, and J.B. Goodenough, Mater. Res. Bull. **18**, 461 (1983).

[17] A.K. Padhi, K.S. Nanjundaswamy, and J.B. Goodenough, J. Electrochem. Soc. **144**, 1188 (1997).

[18] R.N. Seefurth and R.A. Sharma, J. Electrochem. Soc. **124**, 1207 (1977).

[19] J. Wang, I.D. Raistrick, and R.A. Huggins, J. Electrochem. Soc. **133**, 457 (1986).

[20] Y. Idota, T. Kubota, A. Matsufuji, Y. Maekawa, and T. Miyasaka, Science **276**, 1395 (1997).

[21] T.W. Ebbesen and P.M. Ajayan, Nature **358**, 220 (1992).

[22] K.S. Novoselov, A.K. Geim, S.V. Morozov, D. Jiang, Y. Zhang, S.V. Dubonos, I.V. Grigorieva, and A.A. Firsov, Science **306**, 666 (2004).

[23] O. Tsutomu and M. Yoshinari, Chem. Lett. **30**, 642 (2001).

[24] B. Scrosati and J.r. Garche, J. Power Sources **195**, 2419 (2010).

[25] L.X. Yuan, Z.H. Wang, W.X. Zhang, X.L. Hu, J.T. Chen, Y.H. Huang, and J.B. Goodenough, Energy Environ. Sci. **4**, 269 (2011).

[26] A. Manthiram, A. Vadivel Murugan, A. Sarkar, and T. Muraliganth, Energy Environ. Sci. **1**, 621 (2008).

[27] C.H. Xu, B.H. Xu, Y. Gu, Z.G. Xiong, J. Sun, and X.S. Zhao, Energy Environ. Sci. **6**, 1388 (2013).

[28] C. Ripp, G. Hambitzer, L. Zinck, and M. Borck, in *Encyclopedia of Electrochemical Power Sources* (Elsevier, Amsterdam, 2009), pp. 383.

[29] B. Xu, D. Qian, Z. Wang, and Y.S. Meng, Materials Science and Engineering: R: Reports **73**, 51 (2012).

[30] K. Xu, Chem. Rev. **104**, 4303 (2004).

[31] K. Edstrom, M. Herstedt, and D.P. Abraham, J. Power Sources **153**, 380 (2006).

[32] K. Zaghib, G. Nadeau, and K. Kinoshita, J. Electrochem. Soc. **147**, 2110 (2000).

[33] J.B. Goodenough and Y. Kim, Chem. Mater. **22**, 587 (2009).

[34] U. Kasavajjula, C. Wang, and A.J. Appleby, J. Power Sources **163**, 1003 (2007).

[35] H. Ma, F. Cheng, J.Y. Chen, J.Z. Zhao, C.S. Li, Z.L. Tao, and J. Liang, Adv. Mater. **19**, 4067 (2007).

[36] X.F. Zhang, K.X. Wang, X. Wei, and J.S. Chen, Chem. Mater. **23**, 5290 (2011).

[37] G.G. Amatucci, J.M. Tarascon, and L.C. Klein, Solid State Ionics **83**, 167 (1996).

[38] A.Q. Pan, J.G. Zhang, Z.M. Nie, G.Z. Cao, B.W. Arey, G.S. Li, S.Q. Liang, and J. Liu, J. Mater. Chem. **20**, 9193 (2010).

[39] Y.J. Ji, S.G. Li, G.M. Zhong, Z.R. Zhang, Y.X. Li, M.J. McDonald, and Y. Yang, J. Electrochem. Soc. **162**, A7015 (2015).

[40] D.K. Kim, P. Muralidharan, H.W. Lee, R. Ruffo, Y. Yang, C.K. Chan, H. Peng, R.A. Huggins, and Y. Cui, Nano Lett. **8**, 3948 (2008).

[41] X.L. Wu, L.Y. Jiang, F.F. Cao, Y.G. Guo, and L.J. Wan, Adv. Mater. **21**, 2710 (2009).

[42] J. Shin, H. Jung, Y. Kim, and J. Kim, J. Alloys Compd. **589**, 322 (2014).

[43] Y. Wang, K. Takahashi, K.H. Lee, and G.Z. Cao, Adv. Funct. Mater. **16**, 1133 (2006).

[44] E. Antolini, Solid State Ionics **170**, 159 (2004).

[45] Y. Gu, D. Chen, and X. Jiao, The Journal of Physical Chemistry B **109**, 17901 (2005).

[46] W. Chang, J.W. Choi, J.C. Im, and J.K. Lee, J. Power Sources **195**, 320 (2010).

[47] L. Liu, Z. Wang, H. Li, L. Chen, and X. Huang, Solid State Ionics **152**, 341 (2002).

[48] S. Gopukumar, Y. Jeong, and K.B. Kim, Solid State Ionics **159**, 223 (2003).

[49] H.J. Kweon, J. Park, J. Seo, G. Kim, B. Jung, and H.S. Lim, J. Power Sources **126**, 156 (2004).

[50] S. Oh, J.K. Lee, D. Byun, W.I. Cho, and B. Won Cho, J. Power Sources **132**, 249 (2004).

[51] T. Fang, J.G. Duh, and S.R. Sheen, Thin Solid Films **469**, 361 (2004).

[52] Y.I. Jang, B. Huang, H. Wang, D.R. Sadoway, G. Ceder, Y.M. Chiang, H. Liu, and H. Tamura, J. Electrochem. Soc. **146**, 862 (1999).

[53] H. Tukamoto and A.R. West, J. Electrochem. Soc. **144**, 3164 (1997).

[54] J.W. Fergus, J. Power Sources **195**, 939 (2010).

[55] C. Pouillerie, L. Croguennec, P. Biensan, P. Willmann, and C. Delmas, J. Electrochem. Soc. **147**, 2061 (2000).

[56] S.K. Mishra and G. Ceder, Phys. Rev. B **59**, 6120 (1999).

[57] B.L. Ellis, K.T. Lee, and L.F. Nazar, Chem. Mater. **22**, 691 (2010).

[58] Z. Liu, A. Yu, and J.Y. Lee, J. Power Sources **81**, 416 (1999).

[59] M. Yoshio, H. Noguchi, J.I. Itoh, M. Okada, and T. Mouri, J. Power Sources **90**, 176 (2000).

[60] N. Yabuuchi and T. Ohzuku, J. Power Sources **119**, 171 (2003).

[61] I. Belharouak, Y.K. Sun, J. Liu, and K. Amine, J. Power Sources **123**, 247 (2003).

[62] M.H. Lee, Y.J. Kang, S.T. Myung, and Y.K. Sun, Electrochim. Acta **50**, 939 (2004).

[63] S.H. Park, C.S. Yoon, S.G. Kang, H.S. Kim, S.I. Moon, and Y.K. Sun, Electrochim. Acta **49**, 557 (2004).

[64] J.R. He, Y.F. Chen, P.J. Li, Z.G. Wang, F. Qi, and J.B. Liu, RSC Advances **4**, 2568 (2014).

[65] Z. Yang, Z. Song, G. Chu, X. Kang, T. Ren, W. Yang, and Q. Qiao, J. Mater. Sci. **47**, 4205 (2012).

[66] J.T. Son and E.J. Cairns, J. Power Sources **166**, 343 (2007).

[67] C. Venkateswara Rao, A. Leela Mohana Reddy, Y. Ishikawa, and P.M. Ajayan, ACS Applied Materials & Interfaces **3**, 2966 (2011).

[68] S.K. Hu, G.H. Cheng, M.Y. Cheng, B.J. Hwang, and R. Santhanam, J. Power Sources **188**, 564 (2009).

[69] M.M. Thackeray, A. de Kock, and W.I.F. David, Mater. Res. Bull. **28**, 1041 (1993).

[70] M.M. Thackeray, Y. Shao Horn, A.J. Kahaian, K.D. Kepler, E. Skinner, J.T. Vaughey, and S.A. Hackney, Electrochemical and Solid-State Letters **1**, 7 (1998).

[71] M.M. Thackeray, Prog. Solid State Chem. **25**, 1 (1997).

[72] S.S. Zhang and T.R. Jow, J. Power Sources **109**, 172 (2002).

[73] H. Xia, Z. Luo, and J. Xie, Progress in Natural Science: Materials International **22**, 572 (2012).

[74] Y. Xia, Y. Zhou, and M. Yoshio, J. Electrochem. Soc. **144**, 2593 (1997).

[75] D.H. Jang, Y.J. Shin, and S.M. Oh, J. Electrochem. Soc. **143**, 2204 (1996).

[76] H. Huang, C.A. Vincent, and P.G. Bruce, J. Electrochem. Soc. **146**, 3649 (1999).

[77] T. Ohzuku, S. Takeda, and M. Iwanaga, J. Power Sources **81**, 90 (1999).

[78] J. Molenda, J. Marzec, K. Åświerczek, W. Ojczyk, M. Ziemnicki, M. Molenda, M. Drozdek, and R. Dziembaj, Solid State Ionics **171**, 215 (2004).

[79] J.H. Kim, S.T. Myung, C.S. Yoon, S.G. Kang, and Y.K. Sun, Chem. Mater. **16**, 906 (2004).

[80] M. Hu, X. Pang, and Z. Zhou, J. Power Sources **237**, 229 (2013).

[81] A.K. Padhi, K.S. Nanjundaswamy, and J.B. Goodenough, J. Electrochem. Soc. **144**, 1188 (1997).

[82] B. Wang, B. Xu, T. Liu *et al.*, Nanoscale **6**, 986 (2014).

[83] B. Wang, Q. Wang, B. Xu, T. Liu, D. Wang, and G. Zhao, RSC Advances **3**, 20024 (2013).

[84] Z. Xu, L. Gao, Y. Liu, and L. Li, J. Electrochem. Soc. **163**, A2600 (2016).

[85] A.S. Andersson, B. Kalska, L. Haggstrom, and J.O. Thomas, Solid State Ionics **130**, 41 (2000).

[86] M.S. Whittingham, Y. Song, S. Lutta, P.Y. Zavalij, and N.A. Chernova, J. Mater. Chem. **15**, 3362 (2005).

[87] R. Malik, D. Burch, M. Bazant, and G. Ceder, Nano Lett. **10**, 4123 (2010).

[88] F. Omenya, B. Wen, J. Fang, R. Zhang, Q. Wang, N.A. Chernova, J. Schneider-Haefner, F. Cosandey, and M.S. Whittingham, Adv. Energy Mater. **5**, 1401204 (2015).

[89] Y. Wu, Z. Wen, and J. Li, Adv. Mater. **23**, 1126 (2011).

[90] C. Sun, S. Rajasekhara, J.B. Goodenough, and F. Zhou, J. Am. Chem. Soc. **133**, 2132 (2011).

[91] Y. Wang, Y. Wang, E. Hosono, K. Wang, and H. Zhou, Angew. Chem. Int. Ed. **47**, 7461 (2008).

[92] Z. Li, Z. Peng, H. Zhang, T. Hu, M. Hu, K. Zhu, and X. Wang, Nano Lett. **16**, 795 (2016).

[93] B. Wang, W. Al Abdulla, D. Wang, and X.S. Zhao, Energy Environ. Sci. **8**, 869 (2015).

[94] S. Yoon, C. Liao, X.G. Sun, C.A. Bridges, R.R. Unocic, J. Nanda, S. Dai, and M.P. Paranthaman, J. Mater. Chem. **22**, 4611 (2012).

[95] X. Zhou, F. Wang, Y. Zhu, and Z. Liu, J. Mater. Chem. **21**, 3353 (2011).

[96] B. Wang, S. Wang, P. Liu, J. Deng, B.H. Xu, T.F. Liu, D.L. Wang, and X.S. Zhao, Mater. Lett. **118**, 137 (2014).

[97] G. Nihoul, C. Leroux, V. Madigou, and J. Durak, Solid State Ionics **117**, 105 (1999).

[98] H.G. Bachmann, F.R. Ahmed, and W.H. Barnes, Zeitschrift fur Kristallographie **115**, 110 (1961).

[99] C. Delmas, H. Cognac-Auradou, J.M. Cocciantelli, M. Menetrier, and J.P. Doumerc, Solid State Ionics **69**, 257 (1994).

[100] N.A. Chernova, M. Roppolo, A.C. Dillon, and M.S. Whittingham, J. Mater. Chem. **19**, 2526 (2009).

[101] Y. Wang and G. Cao, Chem. Mater. **18**, 2787 (2006).

[102] M.S. Whittingham, J. Electrochem. Soc. **123**, 315 (1976).

[103] M. Xie, X. Sun, H. Sun, T. Porcelli, S.M. George, Y. Zhou, and J. Lian, J. Mater. Chem. A **4**, 537 (2016).

[104] S.H. Ng, T.J. Patey, R. Buchel, F. Krumeich, J.Z. Wang, H.K. Liu, S.E. Pratsinis, and P. Novak, PCCP **11**, 3748 (2009).

[105] S. Afyon, F. Krumeich, C. Mensing, A. Borgschulte, and R. Nesper, Scientific Reports **4**, 7113 (2014).

[106] H.M. Liu and W.S. Yang, Energy Environ. Sci. **4**, 4000 (2011).

[107] W.Y. Ma, B. Zhou, J.F. Wang, X.D. Zhang, and Z.Y. Jiang, J. Phys. D: Appl. Phys. **46**, 105306 (2013).

[108] P. Balog, D. Orosel, Z. Cancarevic, C. Schon, and M. Jansen, J. Alloys Compd. **429**, 87 (2007).

[109] X. Peng, X. Zhang, L. Wang *et al.*, Adv. Funct. Mater. **26**, 784 (2016).

[110] J. Cheng, B. Wang, H.L. Xin, G. Yang, H. Cai, F. Nie, and H. Huang, J. Mater. Chem. A **1**, 10814 (2013).

[111] S.L. Chou, J.Z. Wang, J.Z. Sun, D. Wexler, M. Forsyth, H.K. Liu, D.R. MacFarlane, and S.X. Dou, Chem. Mater. **20**, 7044 (2008).

[112] J.M. Cocciantelli, J.P. Doumerc, M. Pouchard, M. Broussely, and J. Labat, J. Power Sources **34**, 103 (1991).

[113] C. Leger, S. Bach, P. Soudan, and J.P. Pereira-Ramos, J. Electrochem. Soc. **152**, A236 (2005).

[114] V. Petkov, P.N. Trikalitis, E.S. Bozin, S.J.L. Billinge, T. Vogt, and M.G. Kanatzidis, J. Am. Chem. Soc. **124**, 10157 (2002).

[115] K. West, B. Zachau-Christiansen, T. Jacobsen, and S. Skaarup, Electrochim. Acta **38**, 1215 (1993).

[116] Y. Wang, H. Shang, T. Chou, and G. Cao, The Journal of Physical Chemistry B **109**, 11361 (2005).

[117] K. Salloux, F. Chaput, H.P. Wong, B. Dunn, and M.W. Breiter, J. Electrochem. Soc. **142**, L191 (1995).

[118] E.C. Almeida, M. Abbate, and J.M. Rosolen, Solid State Ionics **140**, 241 (2001).

[119] P.G. Bruce, B. Scrosati, and J.M. Tarascon, Angew. Chem. Int. Ed. **47**, 2930 (2008).

[120] T. Zhai, H. Liu, H. Li *et al.*, Adv. Mater. **22**, 2547 (2010).

[121] Z.L. Wang, D. Xu, L.M. Wang, and X.B. Zhang, ChemPlusChem **77**, 124 (2012).

[122] A.M. Cao, J.S. Hu, H.P. Liang, and L.J. Wan, Angew. Chem. Int. Ed. **44**, 4391 (2005).

[123] M. Sasidharan, N. Gunawardhana, M. Yoshio, and K. Nakashima, J. Electrochem. Soc. **159**, A618 (2012).

[124] C.K. Chan, H. Peng, R.D. Twesten, K. Jarausch, X.F. Zhang, and Y. Cui, Nano Lett. **7**, 490 (2007).

[125] G. Li, S. Pang, L. Jiang, Z. Guo, and Z. Zhang, The Journal of Physical Chemistry B **110**, 9383 (2006).

[126] X. Rui, J. Zhu, W. Liu *et al.*, RSC Advances **1**, 117 (2011).

[127] X. Rui, Y. Tang, O.I. Malyi *et al.*, Nano Energy **22**, 583 (2016).

[128] K. Takahashi, S.J. Limmer, Y. Wang, and G. Cao, The Journal of Physical Chemistry B **108**, 9795 (2004).

[129] D. Yu, C. Chen, S. Xie, Y. Liu, K. Park, X. Zhou, Q. Zhang, J. Li, and G. Cao, Energy Environ. Sci. **4**, 858 (2011).

[130] V.M. Mohan, B. Hu, W. Qiu, and W. Chen, J. Appl. Electrochem. **39**, 2001 (2009).

[131] Y. Wang, K. Takahashi, H. Shang, and G. Cao, The Journal of Physical Chemistry B **109**, 3085 (2005).

[132] Y. Li, J. Yao, E. Uchaker, J. Yang, Y. Huang, M. Zhang, and G. Cao, Adv. Energy Mater. **3**, 1171 (2013).

[133] S. Liang, Y. Hu, Z. Nie, H. Huang, T. Chen, A. Pan, and G. Cao, Nano Energy **13**, 58 (2015).

[134] L. Mai, L. Xu, C. Han, X. Xu, Y. Luo, S. Zhao, and Y. Zhao, Nano Lett. **10**, 4750 (2010).

[135] N. Liu, Z.D. Lu, J. Zhao, M.T. McDowell, H.W. Lee, W.T. Zhao, and Y. Cui, Nat Nano **9**, 187 (2014).

[136] Y.K. Sun, S.M. Oh, H.K. Park, and B. Scrosati, Adv. Mater. **23**, 5050 (2011).

[137] H.F. Xiang, H. Wang, C.H. Chen, X.W. Ge, S. Guo, J.H. Sun, and W.Q. Hu, J. Power Sources **191**, 575 (2009).

[138] P. Zhang, L. Zhao, Q. An, Q. Wei, L. Zhou, X. Wei, J. Sheng, and L. Mai, Small **12**, 1082 (2016).

[139] H.B. Wu, A. Pan, H.H. Hng, and X.W. Lou, Adv. Funct. Mater. **23**, 5669 (2013).

[140] A. Pan, T. Zhu, H.B. Wu, and X.W. Lou, Chemistry – A European Journal **19**, 494 (2013).

[141] A.Q. Pan, H.B. Wu, L. Zhang, and X.W. Lou, Energy Environ. Sci. **6**, 1476 (2013).

[142] J. Zhu, L. Cao, Y. Wu *et al.*, Nano Lett. **13**, 5408 (2013).

[143] C. Zhang, Z. Chen, Z. Guo, and X.W. Lou, Energy Environ. Sci. **6**, 974 (2013).

[144] L. Mai, Q. An, Q. Wei *et al.*, Small **10**, 3032 (2014).

[145] A. Pan, H.B. Wu, L. Yu, and X.W. Lou, Angew. Chem. Int. Ed. **52**, 2226 (2013).

[146] M. Sathiya, A.S. Prakash, K. Ramesha, J.M. Tarascon, and A.K. Shukla, J. Am. Chem. Soc. **133**, 16291 (2011).

[147] X.L. Jia, Z. Chen, A. Suwarnasarn *et al.*, Energy Environ. Sci. **5**, 6845 (2012).

[148] K. Palanisamy, J.H. Um, M. Jeong, and W.S. Yoon, Scientific Reports **6**, 31275 (2016).

[149] Y.S. Hu, X. Liu, J.O. Müller, R. Schlögl, J. Maier, and D.S. Su, Angew. Chem. Int. Ed. **48**, 210 (2009).

[150] Z. Chen, V. Augustyn, J. Wen, Y.W. Zhang, M.Q. Shen, B. Dunn, and Y.F. Lu, Adv. Mater. **23**, 791 (2011).

[151] M. Koltypin, V. Pol, A. Gedanken, and D. Aurbach, J. Electrochem. Soc. **154**, A605 (2007).

[152] X. Rui, D. Sim, C. Xu, W. Liu, H. Tan, K. Wong, H.H. Hng, T.M. Lim, and Q. Yan, RSC Advances **2**, 1174 (2012).

[153] A. Odani, V.G. Pol, S.V. Pol, M. Koltypin, A. Gedanken, and D. Aurbach, Adv. Mater. **18**, 1431 (2006).

[154] K.P. De Jong and J.W. Geus, Catalysis Reviews **42**, 481 (2000).

[155] K. Balasubramanian and M. Burghard, Small **1**, 180 (2005).

[156] J.P. Salvetat, J.M. Bonard, N.H. Thomson, A.J. Kulik, L. Forro, W. Benoit, and L. Zuppiroli, Appl. Phys. A **69**, 255 (1999).

[157] P.M. Ajayan, Chem. Rev. **99**, 1787 (1999).

[158] D. Tasis, N. Tagmatarchis, A. Bianco, and M. Prato, Chem. Rev. **106**, 1105 (2006).

[159] X.Y. Chen, H.L. Zhu, Y.C. Chen, Y.Y. Shang, A.Y. Cao, L.B. Hu, and G.W. Rubloff, ACS Nano **6**, 7948 (2012).

[160] D.B. Kong, X.L. Li, Y.B. Zhang, X. Hai, B. Wang, X.Y. Qiu, Q. Song, Q.H. Yang, and L.J. Zhi, Energy Environ. Sci. **9**, 906 (2016).

[161] J.W. Lee, S.Y. Lim, H.M. Jeong, T.H. Hwang, J.K. Kang, and J.W. Choi, Energy Environ. Sci. **5**, 9889 (2012).

[162] C.N.R. Rao, A.K. Sood, K.S. Subrahmanyam, and A. Govindaraj, Angew. Chem. Int. Ed. **48**, 7752 (2009).

[163] X. Huang, X. Qi, F. Boey, and H. Zhang, Chem. Soc. Rev. **41**, 666 (2012).

[164] S. Dubin, S. Gilje, K. Wang *et al.*, ACS Nano **4**, 3845 (2010).

[165] D. Li, M.B. Muller, S. Gilje, R.B. Kaner, and G.G. Wallace, Nat Nano **3**, 101 (2008).

[166] X. Rui, J. Zhu, D. Sim, C. Xu, Y. Zeng, H.H. Hng, T.M. Lim, and Q. Yan, Nanoscale **3**, 4752 (2011).

[167] Q. Liu, Z.F. Li, Y.D. Liu *et al.*, Nat Commun **6** (2015).

[168] S.H. Choi and Y.C. Kang, Chemistry – A European Journal **20**, 6294 (2014).

[169] S. Gilje, S. Han, M. Wang, K.L. Wang, and R.B. Kaner, Nano Lett. **7**, 3394 (2007).

[170] W. Hu, X.B. Zhang, Y.L. Cheng, C.Y. Wu, F. Cao, and L.M. Wang, ChemSusChem **4**, 1091 (2011).

[171] D. Zhu, H. Liu, L. Lv, Y.D. Yao, and W.Z. Yang, Scripta Mater. **59**, 642 (2008).

[172] H.K. Park, Solid State Ionics **176**, 307 (2005).

[173] K. Zhu, H. Qiu, Y. Zhang, D. Zhang, G. Chen, and Y. Wei, ChemSusChem **8**, 1017 (2015).

[174] G.N. Kryukova, G.A. Zenkovets, N. Pfander, D.S. Su, and R. Schlogl, Materials Science and Engineering: A **343**, 8 (2003).

[175] F. Coustier, J. Hill, B.B. Owens, S. Passerini, and W.H. Smyrl, J. Electrochem. Soc. **146**, 1355 (1999).

[176] F. Coustier, S. Passerini, and W.H. Smyrl, Solid State Ionics **100**, 247 (1997).

[177] D.W. Liu, Y.Y. Liu, A.Q. Pan, K.P. Nagle, G.T. Seidler, Y.H. Jeong, and G.Z. Cao, J. Phys. Chem. C **115**, 4959 (2011).

[178] D.W. Liu, Y.Y. Liu, B.B. Garcia, Q.F. Zhang, A.Q. Pan, Y.H. Jeong, and G.Z. Cao, J. Mater. Chem. **19**, 8789 (2009).

[179] Q.H. Wu, A. Thissen, W. Jaegermann, and M. Liu, Appl. Surf. Sci. **236**, 473 (2004).

[180] H.Q. Song, C.F. Liu, C.K. Zhang, and G.Z. Cao, Nano Energy **22**, 1 (2016).

[181] R.J. Brodd, K.R. Bullock, R.A. Leising, R.L. Middaugh, J.R. Miller, and E. Takeuchi, J. Electrochem. Soc. **151**, K1 (2004).

[182] V. Bodenez, L. Dupont, M. Morcrette, C. Surcin, D.W. Murphy, and J.M. Tarascon, Chem. Mater. **18**, 4278 (2006).

[183] K. West and A.M. Crespi, J. Power Sources **54**, 334 (1995).

[184] R. Shannon, Acta Crystallographica Section A **32**, 751 (1976).

[185] Y. Li, J. Yao, E. Uchaker, M. Zhang, J. Tian, X. Liu, and G. Cao, J. Phys. Chem. C **117**, 23507 (2013).

[186] T.F. Otero and J. Rodriguez, Electrochim. Acta **39**, 245 (1994).

[187] P. Sengodu and A.D. Deshmukh, RSC Advances **5**, 42109 (2015).

[188] H. Zhao, A. Yuan, B. Liu, S. Xing, X. Wu, and J. Xu, J. Appl. Electrochem. **42**, 139 (2012).

[189] L. Noerochim, J.Z. Wang, D. Wexler, M.M. Rahman, J. Chen, and H.-K. Liu, J. Mater. Chem. **22**, 11159 (2012).

[190] Y.H. Wang, H. Liu, D. Zhu, Z.P. Guo, H.K. Liu, and S.X. Dou, Transactions of Nonferrous Metals Society of China **21**, 1303 (2011).

[191] L.L. Li, S.J. Peng, H.Y. Chen, X.P. Han, F.Y. Cheng, M. Srinivasan, S. Adams, S. Ramakrishna, and J. Chen, Nano Energy **19**, 307 (2016).

[192] F.S. Gittleson, J. Hwang, R.C. Sekol, and A.D. Taylor, J. Mater. Chem. A **1**, 7979 (2013).

[193] K.I. Park, H.M. Song, Y. Kim, S.I. Mho, W.I. Cho, and I.H. Yeo, Electrochim. Acta **55**, 8023 (2010).

[194] Y.P. Chen, G. Yang, Z.H. Zhang, X.Y. Yang, W.H. Hou, and J.J. Zhu, Nanoscale **2**, 2131 (2010).

[195] D.L. Chao, X.H. Xia, J.L. Liu, Z.X. Fan, C.F. Ng, J.Y. Lin, H. Zhang, Z.X. Shen, and H.J. Fan, Adv. Mater. **26**, 5794 (2014).

[196] H.M. Song, D.Y. Yoo, S.K. Hong, J.S. Kim, W.I. Cho, and S.I. Mho, Electroanalysis **23**, 2094 (2011).

[197] C.W. Kwon, A.V. Murugan, and G. Campet, Act. passive electron. compon. **26**, 171 (2003).

[198] A.V. Murugan, C.W. Kwon, G. Campet, B.B. Kale, T. Maddanimath, and K. Vijayamohanan, J. Power Sources **105**, 1 (2002).

[199] S.Y. Chew, C. Feng, S.H. Ng, J. Wang, Z. Guo, and H. Liu, J. Electrochem. Soc. **154**, A633 (2007).

[200] J.M. Kim, H.S. Park, J.H. Park, T.H. Kim, H.K. Song, and S.Y. Lee, ACS Applied Materials & Interfaces **6**, 12789 (2014).

[201] H. An, X. Li, C. Chalker, M. Stracke, R. Verduzco, and J.L. Lutkenhaus, ACS Applied Materials & Interfaces **8**, 28585 (2016).

[202] M. Ihsan, Q. Meng, L. Li *et al.*, Electrochim. Acta **173**, 172 (2015).

[203] R. Yu, C. Zhang, Q. Meng, Z. Chen, H. Liu, and Z. Guo, ACS Applied Materials & Interfaces **5**, 12394 (2013).

[204] B. Sun, K. Huang, X. Qi, X.L. Wei, and J.X. Zhong, Adv. Funct. Mater. **25**, 5633 (2015).

[205] Y.N. Ko, S.H. Choi, Y.C. Kang, and S.B. Park, ACS Applied Materials & Interfaces **5**, 3234 (2013).

[206] H. Zeng, D. Liu, Y. Zhang, K.A. See, Y.-S. Jun, G. Wu, J.A. Gerbec, X. Ji, and G.D. Stucky, Chem. Mater. **27**, 7331 (2015).

[207] Z. Li, C. Zhang, C. Liu *et al.*, Electrochim. Acta **222**, 1831 (2016).

[208] M. Yoshimura and K. Byrappa, J. Mater. Sci. **43**, 2085 (2008).

[209] K. Byrappa and M. Yoshimura, *Handbook of Hydrothermal Technology*. (William Andrew Publishing, Norwich, NY, 2001), pp.ix.

[210] B. Alonso and J. Livage, J. Solid State Chem. **148**, 16 (1999).

[211] C.J. Fontenot, J.W. Wiench, M. Pruski, and G.L. Schrader, The Journal of Physical Chemistry B **104**, 11622 (2000).

[212] Y. Liu, M. Clark, Q. Zhang, D. Yu, D. Liu, J. Liu, and G. Cao, Adv. Energy Mater. **1**, 194 (2011).

[213] H. Higashimura and S. Kobayashi, in *Encyclopedia of Polymer Science and Technology* (John Wiley & Sons, Inc., 2002).

[214] I.Y. Sapurina, *Oxidative Polymerization of Aniline: Molecular Synthesis of Polyaniline and the Formation of Supramolecular Structures*. (InTech, 2012).

[215] P.P. Ewald, in *Fifty Years of X-Ray Diffraction*, edited by P. P. Ewald (Springer US, Boston, MA, 1962), pp. 82.

[216] S. Brunauer, P.H. Emmett, and E. Teller, J. Am. Chem. Soc. **60**, 309 (1938).

[217] G. Huang, F. Zhang, X. Du, Y. Qin, D. Yin, and L. Wang, ACS Nano **9**, 1592 (2015).

[218] M. Yoo, C.W. Frank, and S. Mori, Chem. Mater. **15**, 850 (2003).

[219] S. Seki, S.I. Tabata, S. Matsui, and M. Watanabe, Electrochim. Acta **50**, 379 (2004).

[220] Y.G. Guo, J.S. Hu, and L.J. Wan, Adv. Mater. **20**, 2878 (2008).

[221] H. Zheng, R. Yang, G. Liu, X. Song, and V.S. Battaglia, J. Phys. Chem. C **116**, 4875 (2012).

[222] G. Liu, H. Zheng, A.S. Simens, A.M. Minor, X. Song, and V.S. Battaglia, J. Electrochem. Soc. **154**, A1129 (2007).

[223] T. Marks, S. Trussler, A.J. Smith, D. Xiong, and J.R. Dahn, J. Electrochem. Soc. **158**, A51 (2011).

[224] S. Wang, S. Li, Y. Sun, X. Feng, and C. Chen, Energy Environ. Sci. **4**, 2854 (2011).

[225] R.S. Liu, *Controlled Nanofabrication: Advances and Applications*. (Pan Stanford, 2012).

[226] X. Li, W. Li, H. Ma, and J. Chen, J. Electrochem. Soc. **154**, A39 (2007).

[227] D. Chen, R. Yi, S. Chen, T. Xu, M.L. Gordin, D. Lv, and D. Wang, Materials Science and Engineering: B **185**, 7 (2014).

[228] Z.P. Wang, G.W. Xie, and L.J. Gao, J Nanomater. **2012**, 7 (2012).

[229] G.D. Du, K.H. Seng, Z.P. Guo, J. Liu, W.X. Li, D.Z. Jia, C. Cook, Z.W. Liu, and H.K. Liu, RSC Advances **1**, 690 (2011).

[230] K.H. Seng, J. Liu, Z.P. Guo, Z.X. Chen, D. Jia, and H.K. Liu, Electrochem. Commun. **13**, 383 (2011).

[231] L.Q. Mai, F. Dong, X. Xu, Y.Z. Luo, Q.Y. An, Y.L. Zhao, J. Pan, and J.N. Yang, Nano Lett. **13**, 740 (2013).

[232] R. Corradi and S.P. Armes, Synth. Met. **84**, 453 (1997).

[233] J.H. Xu, H.J. Zhen, Y.D. Jiang, and Y.J. Yang, J. Wuhan Univ. Technol. Mat. Sci. Edit. **24**, 287 (2009).

[234] N. Paradee and A. Sirivat, Polym. Int. **63**, 106 (2014).

[235] K. Bindumadhavan, S.K. Srivastava, and S. Mahanty, Chem. Commun. **49**, 1823 (2013).

[236] L.L. Li, S.J. Peng, H.B. Wu, L. Yu, S. Madhavi, and X.W. Lou, Adv. Energy Mater. **5**, 1500753 (2015).

[237] C.X. Guo, G. Yilmaz, S.C. Chen, S.F. Chen, and X.M. Lu, Nano Energy **12**, 76 (2015).

[238] S.A. Spanninga, D.C. Martin, and Z. Chen, J. Phys. Chem. C **114**, 14992 (2010).

[239] Y. Xiao, J.Y. Lin, S.Y. Tai, S.W. Chou, G. Yue, and J. Wu, J. Mater. Chem. **22**, 19919 (2012).

[240] A. Sakunthala, M.V. Reddy, S. Selvasekarapandian, B.V.R. Chowdari, and P.C. Selvin, Energy Environ. Sci. **4**, 1712 (2011).

[241] Y. Wei, C.W. Ryu, and K.B. Kim, J. Power Sources **165**, 386 (2007).

[242] M.L. Qin, J. Liu, S.Q. Liang, Q. Zhang, X.L. Li, Y. Liu, and M.Y. Lin, J. Solid State Electrochem. **18**, 2841 (2014).

[243] Q. Guo, Z.H. Sun, M. Gao, Z. Tan, B.S. Zhang, and D.S. Su, J. Energy Chem. **22**, 347 (2013).

[244] V. Raju, J. Rains, C. Gates, W. Luo, X. Wang, W.F. Stickle, G.D. Stucky, and X. Ji, Nano Lett. **14**, 4119 (2014).

[245] G.T. Chandrappa, N. Steunou, S. Cassaignon, C. Bauvais, and J. Livage, Catal. Today **78**, 85 (2003).

[246] J. Zhu, L. Cao, Y. Wu *et al.*, Nano Lett. (2013).

[247] H. Yu, X. Rui, H. Tan *et al.*, Nanoscale **5**, 4937 (2013).

[248] H.K. Kim, Y.W. Ok, T.Y. Seong, E.J. Jeon, W. Cho, and Y.S. Yoon, Journal of Vacuum Science & Technology a-Vacuum Surfaces and Films **19**, 2549 (2001).

[249] S. Zhan, Y. Wei, X. Bie, C. Wang, F. Du, G. Chen, and F. Hu, J. Alloys Compd. **502**, 92 (2010).

[250] H. Wang, Z.Y. Tang, and J.X. Li, J. Solid State Electrochem. **14**, 1525 (2010).

[251] G. Gregoire, N. Baffier, A. Kahn Harari, and J.C. Badot, J. Mater. Chem. **8**, 2103 (1998).

[252] H. Ma, S. Zhang, W. Ji, Z. Tao, and J. Chen, J. Am. Chem. Soc. **130**, 5361 (2008).

[253] W. Hu, X.B. Zhang, Y.L. Cheng, Y.M. Wu, and L.M. Wang, Chem. Commun. **47**, 5250 (2011).

[254] P. Gomez-Romero, Adv. Mater. **13**, 163 (2001).